Engineering Properties of Transition Metal Halides via Cationic Alloying

by

Pranvera Kolari

A Thesis Presented in Partial Fulfillment
of the Requirements for the Degree
Master of Science

Approved July 2020 by the
Graduate Supervisory Committee:

Sefaattin Tongay, Chair
Christopher Muhich
Yang Jiao

ARIZONA STATE UNIVERSITY

August 2020

ABSTRACT

Transition metal di- and tri-halides (TMH) have recently gathered research attention owing to their intrinsic magnetism all the way down to their two-dimensional limit. 2D magnets, despite being a crucial component for realizing van der Waals heterostructures and devices with various functionalities, were not experimentally proven until very recently in 2017. The findings opened up enormous possibilities for studying new quantum states of matter that can enable potential to design spintronic, magnetic memory, data storage, sensing, and topological devices. However, practical applications in modern technologies demand materials with various physical and chemical properties such as electronic, optical, structural, catalytic, magnetic etc., which cannot be found within single material systems. Considering that compositional modifications in 2D systems lead to significant changes in properties due to the high anisotropy inherent to their crystallographic structure, this work focuses on alloying of TMH compounds to explore the potentials for tuning their properties. In this thesis, the ternary cation alloys of $Co_{(1-x)}Ni_xCl_2$ and $Mo_{(1-x)}Cr_xCl_3$ were synthesized via chemical vapor transport at a various stoichiometry. Their compositional, structural, and magnetic properties were studied using Energy Dispersive Spectroscopy, Raman Spectroscopy, X-Ray Diffraction, and Vibrating Sample Magnetometry. It was found that completely miscible ternary alloys of $Co_{(1-x)}Ni_xCl_2$ show an increasing Néel temperature with nickel concentration. The $Mo_{(1-x)}Cr_xCl_3$ alloy shows potential magnetic phase changes induced by the incorporation of molybdenum species within the host $CrCl_3$ lattice. Magnetic measurements give insight into potential antiferromagnetic to ferromagnetic transition with molybdenum incorporation, accompanied by a shift in the magnetic easy-axis from

parallel to perpendicular. Phase separation was found in the $Fe_{(1-x)}Cr_xCl_3$ ternary alloy indicating that crystallographic structure compatibility plays an essential role in determining the miscibility of two parent compounds. Alloying across two similar (TMH) compounds appears to yield predictable results in properties as in the case of $Co_{(1-x)}Ni_xCl_2$, while more exotic transitions, as in the case of $Mo_{(1-x)}Cr_xCl_3$, can emerge by alloying dissimilar compounds. When dissimilarity reaches a certain limit, as with $Fe_{(1-x)}Cr_xCl_3$, phase separation becomes more favorable. Future studies focusing on magnetic and structural phase transitions will reveal more insight into the effect of alloying in these TMH systems.

Dedicated to my parents, who instilled in me the value of education

to myself, for having taken on the challenge

to all of human being that I have crossed paths with somewhere along the way,
and who have guided me to where I have reached today

and certainly, to science and advancement.

ACKNOWLEDGMENTS

This work could not have been possible without the guidance and mentorship from many people starting from the staff at Scottsdale Community College where my adventure began. I would like to express great appreciation to Dr. Vicich, who helped me find my way into an exciting science discipline by giving me an opportunity to mentor other peers. Also, I am thankful to have met Dr. Anwar at Arizona State University who offered me opportunities for involvement and teaching during my undergraduate degree. I am very fortunate and thankful to have taken the course taught by my advisor, Dr. Tongay, who later provided me with the opportunity to join his lab group. It was a privilege to have had a chance to work under the guidance of such a great materials scientist. I would like to extend my appreciation to my committee members (Dr. Jiao and Dr. Muhich) for their expert input in reviewing this work. Working in the 2D materials laboratory among such smart individuals helped me grow as a researcher. I am deeply thankful to Mark for all the advice, the long weeks without any days off, and the long days of sealing ampoules. I am thankful to Yuxia, and Cameron, for their amazing mentorship. Similarly, the Janus team, Yasir and Q, have been there for guidance, friendship and even as a stress relieving punch bag for times of need. My work would have not been the same without all my other lab co-workers, as well as Justin, and David for their expert opinion on various equipment. I am grateful for my friends Srishti, Emily, Naushita and their support throughout this journey, and Marcos for all the patience and cooking during busy writing days. I am lucky to have had many passionate professors, advisors, and mentors along the way who make a super long list of amazing individuals.

TABLE OF CONTENTS

Page

LIST OF TABLES

Table Page

Table Page

LIST OF FIGURES

Figure Page

Figure Page

Figure Page

Figure Page

Figure Page

Figure Page

Figure Page

Figure Page

1. INTRODUCTION TO 2D QUANTUM MATERIALS

Classical physics has done wonders in painting the picture for our understanding of the world that we live in, but it can only make accurate predictions up to a certain limit; once the scale is reduced to the nanometer range we enter the quantum world where the laws of classical physics fail to model behavior of matter. Quantum physics beautifully describes matter interactions at very low limits and in doing so, we are now able to make predictions, understand, and develop new classes of materials with exotic properties that have and will continue to revolutionize technology as we know it. Materials that consist of at least one dimension smaller than 100 nm are considered to be nanomaterials (Gupta, Sakthivel, & Seal, 2015). Nanomaterials can take on many types of geometries such as nanosheets, nanotubes, nanospheres, quantum dots etc., all of which possess drastically different properties (Gupta et al., 2015). Among the broad library of nanomaterials are 2D layered structures which will be discussed in this work.

2D materials are, indeed, a relatively new class of materials that have rightfully gained immense attraction in the scientific community, specifically materials science. These materials differ from other rather traditional 3D materials in that they are, namely, confined to two dimensions; the third dimension is only a few nanometers in size. The structure of 2D materials is layered and it is comprised of covalently bonded atoms in-plane (or within each sheet) and weak van der Waals (vdW) forces between sheets (see illustration in Fig.1) (Mas-Ballesté, Gómez-Navarro, Gómez-Herrero, & Zamora, 2011). Due to the ease with which vdW forces can be broken, these structures are able to be cleaved and isolated as individual atomic layers. As such, 2D materials exhibit large

variations in physicochemical, opto-electronic, magnetic and other properties compared to their 3D counterparts (Gibertini, Koperski, Morpurgo, & Novoselov, 2019). The differences come about owing to the increase in surface-to-volume ratio, confinement of electrons leading to a quasi-continuous step-like nature in their density of states, magneto-crystalline anisotropy and so forth (Gupta et al., 2015; Mas-Ballesté et al., 2011).

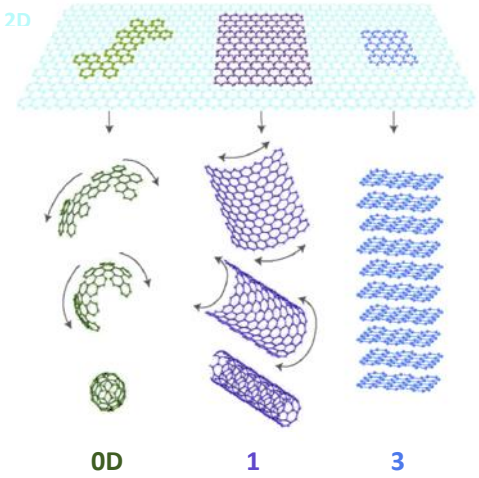

Fig. 1 | Classification of materials based on their dimensionality (Gupta et al., 2015; Mas-Ballesté et al., 2011).

Significant research efforts in 2D materials were inspired after the isolation of monolayer graphene from graphite in 2004 (Gupta et al., 2015; Mas-Ballesté et al., 2011; Novoselov, Mishchenko, Carvalho, & Castro Neto, 2016; Stanford, Rack, & Jariwala, 2018). Among the broad range of 2D structures discovered from there on, the main distinguished classes include the following: transition metal dichalcogenides (TMDCs), layered oxides and hydroxides, hexagonal boron nitride (h-BN), MXenes, phosphorene, and metal-organic frameworks (MOFs). Transition metal halides (TMHs), another class

of 2D materials, are recently gaining a lot of interest in the area of magnetic monolayers (Burch, Mandrus, & Park, 2018). These compounds have yet to be studied in-depth and their potential remains to be realized. Significant amount of attention has been given to TMH structures from a computational aspect, however, much of those predictions are still in need of experimental validation. This work is, hence, intended to shed light upon some aspects of TMH structures such as their flexibility to be alloyed and be modified structurally in order to engineer their magnetic properties.

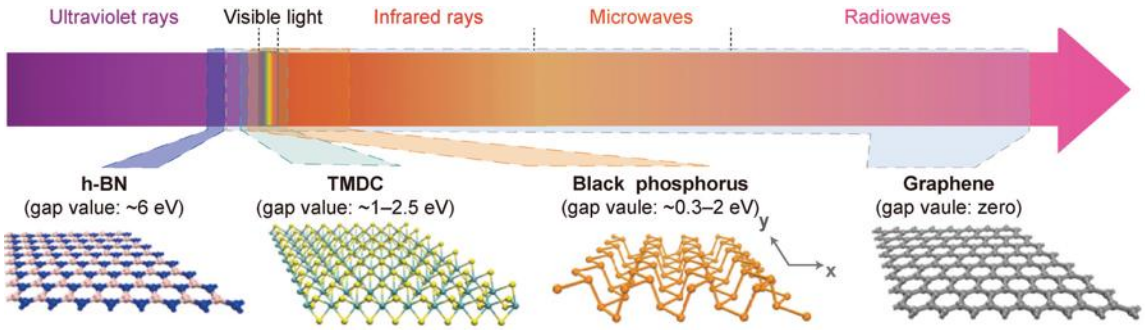

Fig. 2 | Some of the main classes of 2D materials and their respective bandgap energy ranging from insulating (hBN) to metallic (graphene) (Hao Wang et al., 2020).

The implications of the above-mentioned modifications in material properties at the 2D limit are quite significant. From a physical point of view, due to the large surface-to-volume ratio, these structures can be easily modified to achieve surface functionalization for various applications including catalysis (Gupta et al., 2015; Mas-Ballesté et al., 2011). Owing to the high specific surface area, some 2D materials like graphene, graphitic-carbon nitride (g-C3N4), transition metal dichalcogenides (TMDCs), MXenes, and many 2D heterostructures have been identified as great candidates for application in water splitting reactions (oxygen reduction reaction, hydrogen evolution reaction), supercapacitors and energy storage (Deng et al., 2016; Yuan, Pang, & Hao,

2020). Many of them, have been found to have superb mechanical properties which, in addition to low-dimensionality and flexibility of band-structure engineering, implies possibility for further miniaturization of devices and the development of flexible electronics (Gupta et al., 2015; Stanford et al., 2018).

Furthermore, the band structure of single-layer materials can be significantly different from the bulk (3D) compound, and sometimes even compared to a bi-layer structure. These structures are highly sensitive to defects, doping, adsorbed species, strain and other modifications providing further opportunity for engineering their band structure to tailor it to the relevant application (Gupta et al., 2015). In terms of electronic properties, 2D materials can have metallic, semi-metallic, semiconducting, insulating or superconducting character enabling their implementation in electronic and opto-electronic devices (Gupta et al., 2015; Mas-Ballesté et al., 2011; Novoselov et al., 2016; Stanford et al., 2018). Having such small thickness, layered materials are transparent and thus can be implemented into photovoltaic devices (Novoselov et al., 2016).

Owing to their compatibility in terms of stacking 2D layers on top of one another, a wide range of heterostructures can be engineered to yield different properties (Xu et al., 2020). This implies a much broader capability to engineer properties such as in the case of the light emitting diode (LED) build by sandwiching a TMDC layer between layers of hexagonal boron nitride (Xiaomu Wang & Xia, 2015). More advanced applications that would be enabled by the characteristic properties of 2D materials and heterostructures include information storage / spintronic devices (Liu et al., 2020), valleytronics applications (Novoselov et al., 2016), sensing and biomedical device applications

(George & Kandasubramanian, 2020; Zheng, Sun, Han, Xu, & Bu, 2020), magneto-optical nanostructures (Abramchuk et al., 2018) and so on.

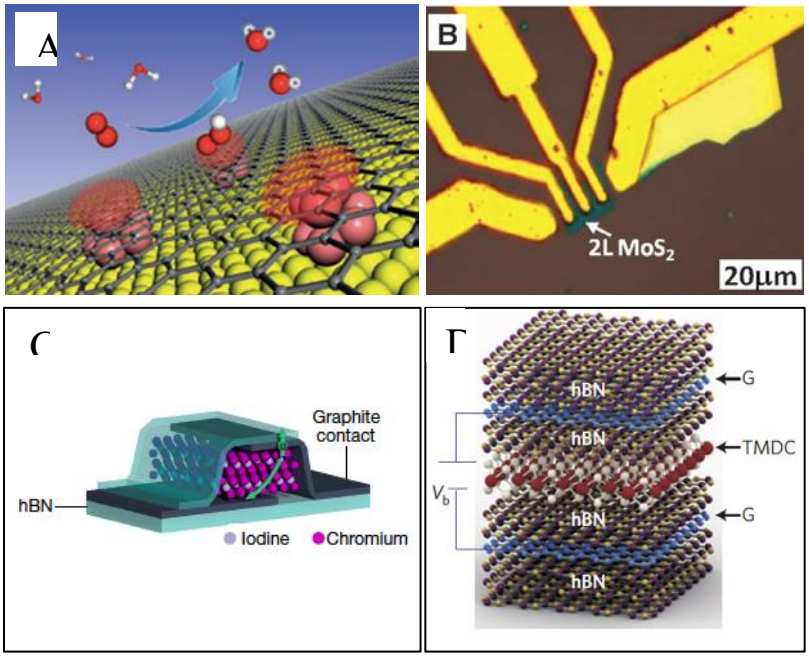

Fig. 3 | Some applications of 2D materials: (A) Photocatalysis reaction on graphene monolayer surface with metal clusters encapsulated beneath (Deng et al., 2016), (B) Field effect transistor device with a bi-layer MoS2 sheet (X. Huang, Zeng, & Zhang, 2013), (C) Magnetic heterostructure device with CrI3 (Burch et al., 2018), (D) vdW heterostructure LED using hBN, graphite, and TMDC layers (X. Huang et al., 2013).

Despite their potential to revolutionize many technologies, 2D materials have their shortcomings; Many of these structures that are predicted have not been realized in practice, while others that have are not always stable in standard atmospheric conditions (Novoselov et al., 2016). Regarding optoelectronic applications, owing to the nanometer scale thickness and transparency, 2D materials suffer from low absorption of light (Hao Wang et al., 2020). Furthermore, uniform large area synthesis is critical for production of opto-electronic devices and implementation in complex circuitry (Stanford et al., 2018). Fabrication of 2D materials at such a scale remains challenging and many 2D structures are still being produced only at the laboratory scale. However, overwhelming amount of

research seems promising that these phenomenal structures can indeed be realized at the industrial scale. For instance, large scale synthesis of graphene and transition metal dichalcogenides with controllable thickness and quality have already been realized (X. Huang et al., 2013). Although a lot of work still remains to be done before this class of materials achieves its full potential in various application fronts, the future of 2D materials is evidently quite optimistic.

1.1 Graphene – The revolutionary atomically thin material

In 2004, the decades long effort to isolate a single layer sheet of graphite was accomplished and it was named graphene. The technique used to perform the isolation is rather simple: using highly oriented pyrolytic graphite (HOPG) to exfoliate or delaminate layers of graphite and transfer them onto a substrate such as SiO_2 which provides phase contrast allowing visualization of single layers under an optical microscope (Mas-Ballesté et al., 2011). This event shook up the materials science field and an enormous amount of research effort was dedicated to synthesizing and studying the properties of the thinnest material known to man.

Graphene has outstanding properties: the monolayers exhibit carrier mobility upwards of 2.5*105 cm2·V-1·s-1 exceeding that of copper, thermal conductivity reaching 5000 W·m-1·K-1, Young's modulus of approximately 1 TPa, and is known to be the strongest material known with strength of 40 N/m (Geim, 2009). Graphene also exhibits superb mechanical properties with elastic strain values about 20% higher compared to traditional conducting materials (Geim, 2009). The observed properties are, naturally, derived from the atomic structure of graphene; the honeycomb crystal lattice allows

electrons to propagate through very rapidly with mean-free path between collisions in the micron-range, and zero effective mass. As such, electrical properties in graphene are described by a Dirac-like equation (versus Schrödinger equation) making it a special material for studying different quantum effects (Bonaccorso, Sun, Hasan, & Ferrari, 2010; Castro Neto, Guinea, Peres, Novoselov, & Geim, 2009; Geim, 2009).

Having such astonishing electrical and mechanical properties, graphene was identified as the material of the future for a large number of technological fronts including electronic, photonic, composites, energy, and bio-applications (Novoselov et al., 2012). Additionally, it can be utilized as an economically viable transparent conductive layer for flexible electronics. In the area of photonics, graphene may find space in fabrication of photodetectors, modulators, solid-state mode-locker lasers, light emitting diodes, THz wave detectors and generators (Bonaccorso et al., 2010; Novoselov et al., 2012). From a mechanical point of view, graphene is anticipated to enhance traditional material strengths by means of reinforcing them (similar to carbon nanotube reinforcement) to make high performance composite structures (Novoselov et al., 2012).

There are roadblocks that must be overcome before these technologies can take full advantage of the graphene potential with the main one being scale-up. Chemical vapor deposition (CVD) has successfully been shown to produce relatively good sheets of graphene (see Fig. 4) at a reasonable cost with control over thickness. However, the reported values for graphene electrical, mechanical, and other properties are associated with high-quality layers produced at a laboratory setting. It is crucial to establish viable and economical methods of synthesizing graphene sheets at an industrial scale having

comparable quality to the ones synthesized in the laboratory. The true potential of graphene, thus, remains to be unleashed in the upcoming decades.

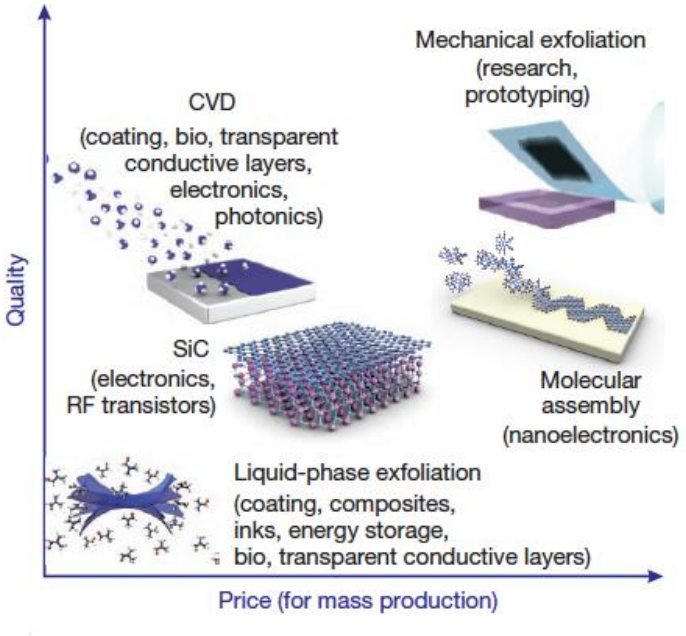

Fig. 4 | Illustration of various synthesis techniques for obtaining thin sheets of 2D vdW materials and their associated quality and cost. (Novoselov et al., 2012)

1.2 Transition metal dichalcogenides (TMDCs)

Composed of transition metals and chalcogen atoms (MX_2, M = transition metal, X = S, Se, Te), TMDC structures are some of the most robust vdW materials that have found potential applications in a variety of fields. Their structure is composed of sheets that are held together by vdW forces where each individual sheet is three-atom thick with metal atoms sandwiched between two layers of chalcogen atoms on top and bottom. These compounds exist in crystal structures with either hexagonal symmetry (trigonal prismatic coordination), or tetragonal symmetry (octahedral coordination) (see Fig. 5).

The structure has a direct correlation to the electronic properties of these materials. For example, compounds that exhibit triangular prismatic structure coordination are known to be semiconducting (e.g. MoS_2, $MoSe_2$, WS_2, WSe_2), while the ones exhibiting octahedral coordination are metallic (e.g. TiS_2, $TiSe_2$, NbS_2, $NbTe_2$) (Choi et al., 2017). A rather intriguing quality of TMDCs is observed in their monolayer form; the bandgap of semiconducting TMDCs (such as MoS_2) undergoes a shift from indirect to direct as the material thickness is reduced from bulk to monolayer. PtS_2 on the other hand undergoes a shift from semi-metallic to semiconducting behavior upon reduction of its thickness from bulk to monolayer (Kang et al., 2020). Such unique electronic and optical properties in TMDCs arise due to the quantum confinement of electrons in two-dimensions. By taking advantage of these phenomena, the band structure of TMDCs can be tailored to the desired applications.

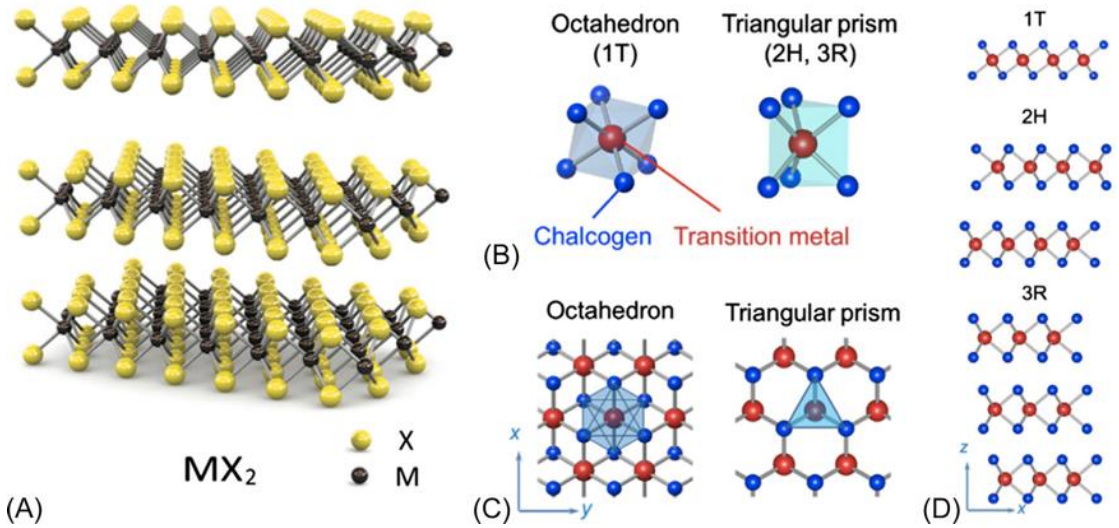

Fig. 5 | Illustration of TMDC structures: (a) MX_2 structure with a layer of metal atoms sandwiched between two layers of chalcogen atoms, (b) the main polytypes of the TMDC structures, namely 1T, 2H, and 3R, (c) main crystal structures showing prismatic and hexagonal symmetry, (d) cross-sectional view of the different polytypes. (Parvez, 2019)

Known to exhibit large room-temperature exciton binding energies (200 meV for MoS_2, 700 meV for WS_2) with resonance in the near IR and the visible light region, TMDCs find applications in optoelectronic devices such as photodetectors, logic gates, LEDs (Ginsberg & Tisdale, 2020). Beyond strongly bound excitons, these compounds have strong light-matter interaction which is express as a coupling between photons and excitons (coupling known as polaritons; half-light, half-matter quasiparticles). Exciton-polariton quasiparticles (see Fig. 6) enable other applications for TMDCs in photonics and quantum communication technologies (Ardizzone et al., 2019).

Recently, a rather interesting phenomenon of spin-valley coupling has attracted a lot of attention to TMDC materials; analogous to exploiting the charge degree of freedom in electronics as well as the spin degree of freedom in spintronics, a new degree of freedom has been determined, namely the valley index which can take +K and -K values (Chhowalla et al., 2013; Ginsberg & Tisdale, 2020). The valley refers to local maxima/minima in the electronic band structure of a semiconductor, and it can be accessed using circularly polarized light. This phenomenon gave rise to a new field, namely valleytronics (analogous to spintronics) which has potential to become yet another method for developing switching devices based on valley quantum numbers.

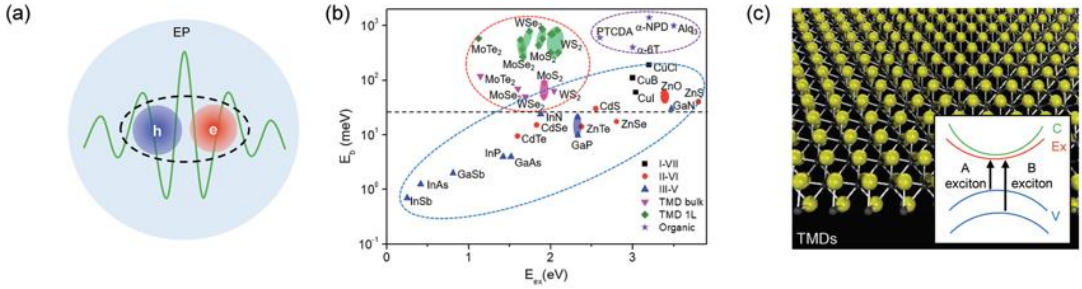

Fig 6. | Electronic band structure characteristics of TMDCs: (a) Exciton-polariton quasiparticle illustration, (b) exciton binding energy (E_b) vs. exciton energy (E_{ex}) of TMDC materials (circled red) compared to other semiconductors, (c) atomic and electronic structure of TMDCs (Hu & Fei, 2020).

Further implications of strong light-matter interaction in TMDC monolayers include their optical response that can be exploited for emission of single photons. This effect was first studied on compounds such as WS_2 and WSe_2 at cryogenic temperatures and the emission was found near areas of lattice strain. Later, another 2D material (hexagonal boron nitride) was found to exhibit room temperature single photon emission from point defects which makes device fabrication more practical and enables the development of quantum computing and sensing technologies (Chakraborty, Vamivakas, & Englund, 2019).

1.3 2D magnetic materials

The 2D materials spectrum spans a broad range of material properties: from metals, semimetals, semiconductors, to insulators and topological insulators. 2D magnets, despite being a crucial component for realizing vdW heterostructures and devices with various functionalities, were not proven experimentally until very recently (in 2017).

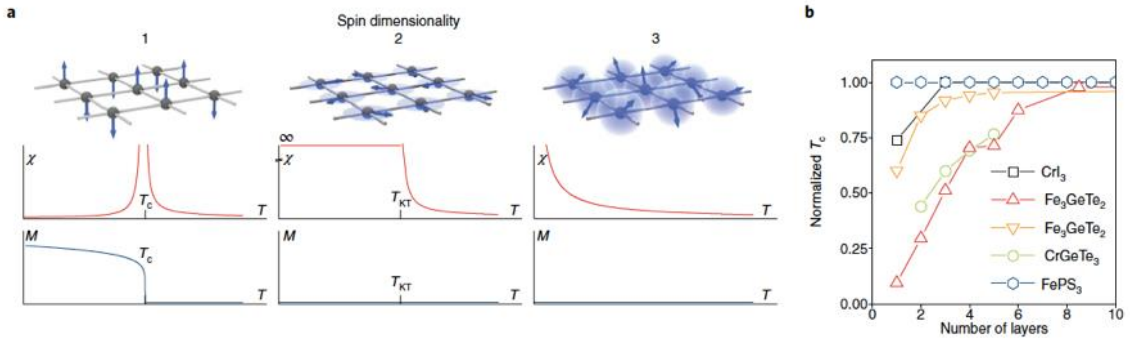

Fig. 7 | (a) Illustration of spin dimensionality of 1, 2, and 3 showcasing the Ising, XY, and isotropic Heisenberg model, respectively. (b) Variation of T_C with material thickness for systems that have been experimentally proven to sustain magnetism in the 2D limit. (Gibertini et al., 2019)

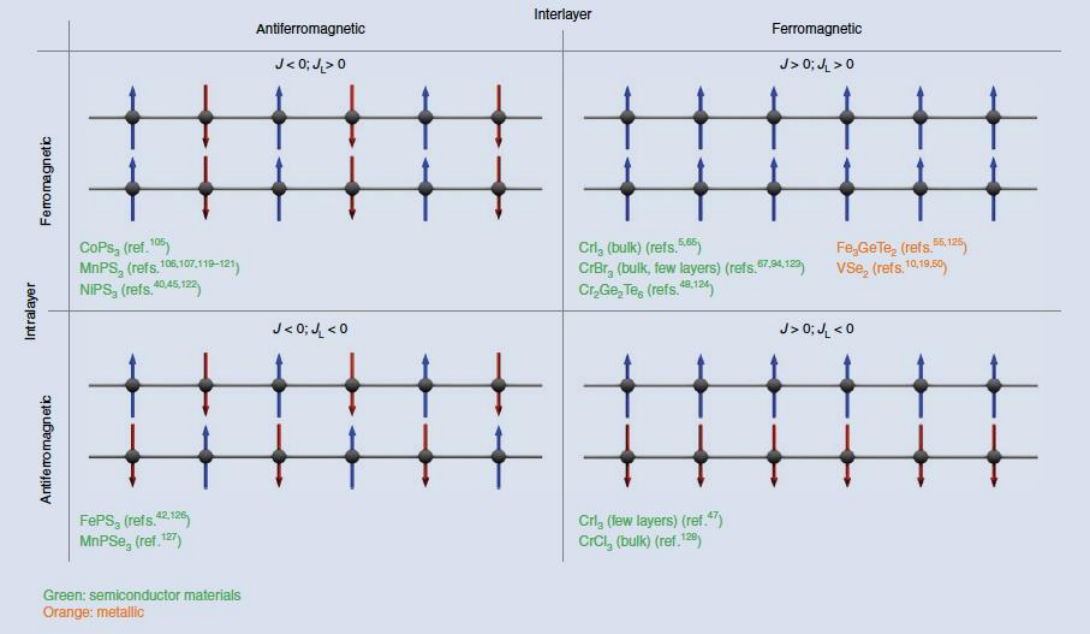

Fig. 8 | Magnetic configurations in some 2D layered materials. This illustration does not show whether the magnetic spins are in-plane or out-of-plane (e.g. in CrI_3, spins are oriented out-of-plane, while in $CrCl_3$, spins are oriented in-plane). (Gibertini et al., 2019).

The Mermin-Wagner theorem restricts the possibility of isolating 2D isotropic materials with long-range magnetic order at finite temperatures as a result of thermal fluctuations (Mermin & Wagner, 1966). Theoretically, assuming a Heisenberg isotropic model with spin dimensionality of 3 in the 2D limit, spin fluctuations were predicted to overpower the spin-ordering phenomenon necessary to establish magnetic domains (see Fig. 7 (a)). Despite this theoretical predictions, 2D magnetism has been experimentally demonstrated in a few vdW systems marking a new milestone in the study of these structures. Long-range, intrinsic magnetic order in vdW materials is made possible via magnetic anisotropy (alignment of spins in the so called easy-axis crystal orientation) which is given rise to by means of spin-orbit coupling or lattice distortions (Botana & Norman, 2019; Klein et al., 2018; Tomar et al., 2019). The 2D limit allows two

orientations of easy-axis, namely, in-plane (XY model) and out-of-plane (Ising model) with the former giving rise to antiferromagnetic behavior (spin alternating between each layer) and the latter yielding a ferromagnetic behavior (spin orientation in the z-axis).

Among many atomically thin materials predicted to exhibit ferromagnetic or antiferromagnetic behavior, some of them have been already demonstrated. The first studies describing the breakthrough findings of magnetism in monolayer vdW materials were published in 2016. Anti-ferromagnetism based on the Ising model was experimentally demonstrated to survive all the way down to the single layer limit in the transition metal phosphorus trichalcogenide structure of $FePS_3$. This study employs indirect methods such as Raman spectroscopy at cryogenic temperatures to show that there is no variation in the Néel transition temperature (T_N) with material thickness down to a single layer of $FePS_3$ (Lee et al., 2016; Xingzhi Wang et al., 2016). Similar studies were published around the same time on other systems such as $NiPS_3$ and $CrSiTe_3$ (Kuo et al., 2016; Lin et al., 2016).

In 2017, chromium triiodide (CrI_3), a transition metal halide compound, was isolated in the single layer form and studied under a polar-magneto-optical Kerr effect microscope. The study yielded the first experimental demonstration of stable ferromagnetic ordered spins in the out-of-plane (Ising) orientation with Curie temperature (T_c) of 61 K (similar to 45 K in the bulk CrI_3) (B. Huang et al., 2017). Further, chromium germanium telluride ($CrGeTe_3$) was also shown to exhibit ferromagnetism in the bi-layer form (Gong et al., 2017). In the $CrGeTe_3$ system magnetism was only sustained in structures of 2 or more layers due to the absence of intrinsic magneto-crystalline anisotropy, which is not the case for the CrI_3 system. More recently, in an astonishing

study, researcher discovered room temperature ferromagnetism in vanadium di-selenide (VSe_2) monolayers, a condition that must be met for practical applications of layered nanomagnets (Bonilla et al., 2018).

These findings open up enormous possibilities to understand new quantum states of matter and bring us closer to designing spintronic, magnetic memory, data storage, sensing, topological and other devices (Botana & Norman, 2019; Klein et al., 2018; Tomar et al., 2019). They also enable scientists to study physics phenomena described by the Heisenberg, Ising, and XY models at the 2D limit, as well as changes that can be induced via gating, lattice strain, or proximity effects and Moiré patterns (Burch et al., 2018).

Clearly, the study of 2D magnets is still at its infancy with a plethora of opportunities for exploration. First and foremost, probing magnetism at such a small scale remains challenging; the development of new probing techniques with high resolution at the nanoscale will greatly accelerate this area of research. The expansion of the 2D magnets library is yet another important development which will enable discoveries of room temperature ferro and anti-ferromagnets. The flexibility allowed by vdW structures to layer various materials in heterostructure format will be crucial for the realization of functional magneto-optical devices, magnetic sensors, spintronic devices and topological quantum computing technology. From a more fundamental viewpoint, this new class of materials will enable studies of exotic quantum phases including quantum spin liquids, Chern insulators, and skyrmions which, in turn, is essential making progress in the area of high-density and low-power data storage systems (Burch et al., 2018; Gibertini et al., 2019).

2. ALLOYING IN 2D LAYERED STRUCTURES

The materials science pyramid correlates the structure and processing of material systems to their properties and performance. Driven by the need to advance technology in many different fronts, new materials systems are developed, and older materials systems are constantly being improved by means of targeting their crystal structure and fabrication methods to enhance and obtain the desired properties for different applications. Modern technologies demand materials with various physical and chemical properties such as electronic, optical, structural, catalytic etc., which cannot be fulfilled solely by the parent compounds without any modifications; thus, continuous tunability of material properties is necessary to enable engineering of these systems for the appropriate applications. Both physical and chemical techniques have been used to successfully alter structure and material properties among which well-documented methods include introduction of defects, strain and electric field, as well as alloying, ion intercalation and temperature (Qian, Jiao, & Xie, 2020).

2.1 Potential of alloying to engineer properties in 2D systems

Many traditional 3D material classes have been well established and documented, and there is a multitude of techniques known to enable controllable tuning of their properties. Alloying has been used for a long time in materials science as a reliable method for obtaining the desired material performance for many applications. A well-known example is stainless steel alloys where addition of metals such as Chromium, Aluminum, Nickel, Copper, Molybdenum, Niobium, and other elements such as Carbon and Nitrogen to elemental iron drastically changes the properties of the alloy.

2D systems are relatively new and have not yet acquired the same level of documentation both in breadth and depth. As a result, a lot of potential in these systems remains to be uncovered. Owing to their unique crystal structures with atomically thin thickness and no dangling bonds, 2D materials enable new avenues for tuning their properties with control at a sub-nanometer level (Cain, Hanson, & Dravid, 2018). Control over the number of layers as well as the stacking order of different layers in 2D vdW materials to build heterostructures are only two of such methods for controlling their properties. Alloying in 2D materials has also been documented in some of the most studied classes such as transition metal mono, di, and tri – chalcogenides (TMMC, TMDC, TMTC, respectively) with a focus on tuning the electronic band structure and phase of the compounds.

Compositional modifications in 2D systems generally lead to significant changes in properties due to the high anisotropy that is inherent to their crystallographic structure. As a result, we observe huge transitions in electronic bandgap (from metallic to insulating behavior) in TMMC alloy of chromium-germanium-telluride ($Cr_{1-x}Ge_xTe_3$) with the amount of tellurium in the crystal structure (Mogi et al., 2018). This alloy system undergoes a structural change as it is converted from Cr_2Te_3 to $Cr_2Ge_2Te_3$. Interestingly, upon reaching the latter compound stoichiometry in this alloys, magnetization with perpendicular anisotropy is induced (Mogi et al., 2018) illustrating the power of alloying to not only tune the material properties, but induce new properties that are sometimes unexpected.

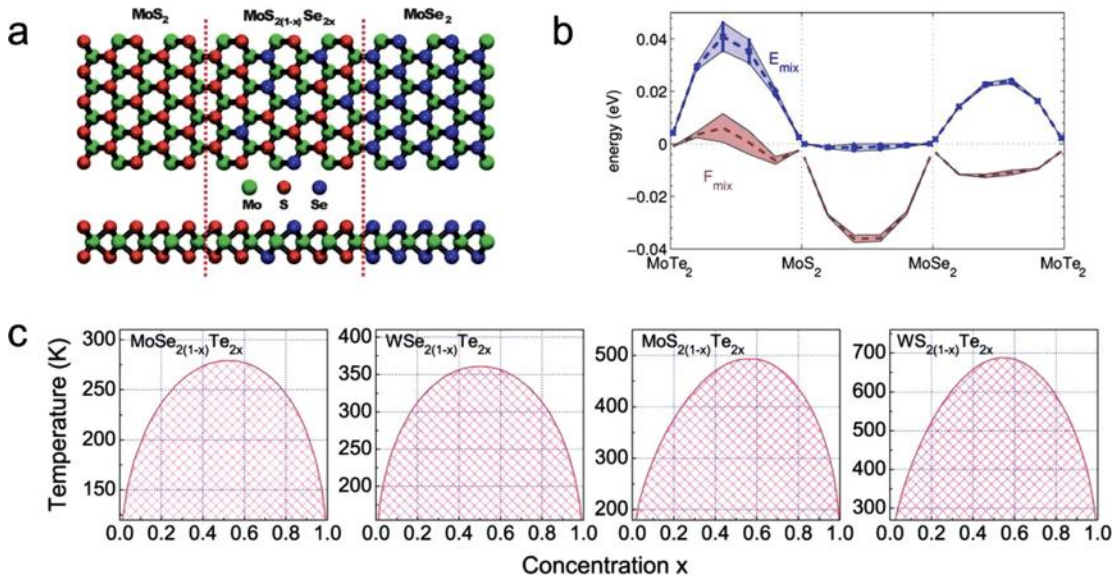

Fig. 9 | Alloying in 2D TMDCs. (a) Crystal structure of parent compounds (MoS_2, $MoSe_2$) and their ternary alloy ($MoS_{2(1-x)}Se_{2x}$), (b) Gibbs-energy of mixing as a function of alloy composition for three ternary compounds, (c) Phase diagrams for four ternary TMDC alloys showing the phase separated region in shaded red color. (Zeng et al., 2015)

New crystallographic phases can be induced via incorporation of foreign elements during alloying. A study found that the $Mo_{1-x}W_xTe_2$ alloy undergoes a phase transition from the semiconducting 2H (trigonal-prismatic) to the metallic Td (orthorhombic) phase at a concentration of > 8% of tungsten. They found a new phase to be stable in this alloy system, namely the orthorhombic Td' (Qian et al., 2020). Similarly, TMDC alloys of $WSe_{1-x}Te_x$ undergo a phase transition from 2H to 1Td with increasing tellurium concentration with a simultaneous band structure change from p-type semiconductor to a metallic electronic character (Qian et al., 2020)

TMDC alloys have been among the most studied compounds due to their enormous stability and exotic electronic band structure. These materials have a relatively low free energy of mixing (see Fig. 9) enabling their full-spectrum (ternary) alloy formation (Zeng et al., 2015). MoX_2, and WX_2 (X = S, Se, Te) parent compounds have

been cross-alloyed both by mixing the chalcogen atoms as well as by mixing the metals. Complete alloying with no region of phase separation has been reported for bulk and monolayer $Mo_{1-x}W_xS_2$, and $Mo_{1-x}W_xSe_2$ alloys (Cain et al., 2018), $MoS_{2(1-x)}Se_{2x}$, and $WS_{2(1-x)}Se_{2x}$ alloys (Duan et al., 2016; Li et al., 2014), and quaternary $Mo_{1-x}W_xSe_{2(1-x)}S_{2x}$ alloy (Susarla et al., 2017). One of the main benefits of having complete alloying capability across the entire composition range in TMDCs is bandgap engineering. The quaternary compound allows tuning the bandgap from as low as 1.61 to 1.85 eV showcasing that the larger number of components (higher alloy order) adds more degrees of freedom for engineering properties (see Fig. 10).

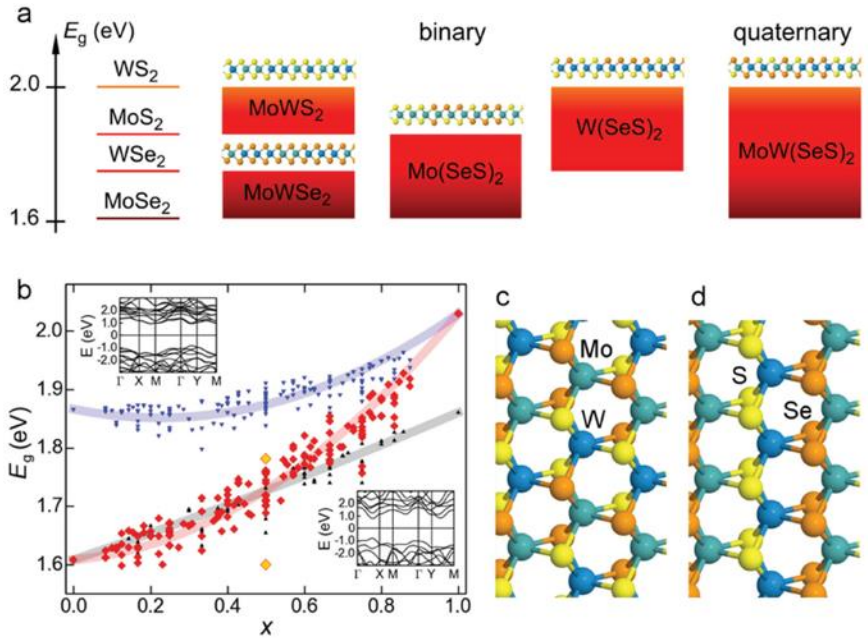

Fig. 10 | Illustration of binary and ternary TMDC alloys. (a) Electronic bandgap comparison of pure binary compounds and their ternary and quaternary alloys (b) Calculated bandgap variation of $Mo_{1-x}W_xSe_{2(1-x)}S_{2x}$ alloy (red), $Mo_{1-x}W_xS_2$ (blue), $MoSe_{2(1-x)}S_{2x}$ (black) with composition ($Mo_{1-x}W_xSe_{2(1-x)}S_{2x}$ band structure with largest bandgap at top inset, and smallest bandgap at bottom inset, (c, d) crystal structure of quaternary alloy. (Susarla et al., 2017)

The presence of complete alloys in the above-mentioned TMDCs does not guarantee that this behavior can be extrapolated to all 2D materials. The formation of a mixed state (alloy) of a compound requires lowering of the free energy of the system, and depending on the system, this may sometimes not be the case. For instance, in the TMTC alloy of $TiS_{3(1-x)}Se_{3x}$, the alloy becomes unstable at composition above 8% of selenium. The phase-separated state of the parent compounds is more thermodynamically stable leading to rejection of selenium from the alloy beyond that limit (Agarwal et al., 2018). The study published by the same group on the $Nb_{1-x}Ti_xS_3$ alloy reflect no such rejection across the entire compositional spectrum (Wu et al., 2020).

Motivated by the reported success and challenges remaining to be overcome in the world of 2D materials, this work is focused on exploring a rather younger class of materials that holds a lot of promise for obtaining 2D magnets and, yet again, revolutionizing future technology – transition metal halides. The extent and flexibility of engineering the properties in these materials remains to be found. Therefore, the upcoming chapters are devoted to the niche topic of cationic alloying in TMH vdW structures with the goal to answer the following questions:

1) Considering that anionic alloys in some TMH compounds have been reported, is it possible to alloy the metal cations and to what extend?
2) What factors determine miscibility of compounds in ternary TMH alloys?
3) In what ways are fundamental properties, including magnetic, of such alloy systems tuned with varying concentration of foreign species within a host lattice?

3. SYNTHESIS AND CHARACTERIZATION TECHNIQUES

The materials discussed in this work are synthesized in the bulk form via two methods: sublimation growth, and chemical vapor transport (CVT). Both methods rely on transport of gaseous species from one location to another, a process driven by the presence of a temperature gradient. The crystals grown by either of the two methods are characterized with techniques that reveal information about their identity or elemental composition, crystal structure, optical and magnetic properties. A brief discussion of the fundamentals of each synthesis method and characterization technique is presented below.

3.1 Synthesis Methods

Crystal growth is a method that has been used historically for synthesizing crystalline materials of various classes for many practical applications. Generally, crystal growth can be achieved from a liquid phase, vapor phase, or solid phase (Feigelson, 2015). Vapor phase growth can be done via physical or chemical deposition techniques. The former is the simplest, most straightforward way of synthesizing high quality crystals and it involved sublimation of compounds in the source (region where precursors are placed), and transport in the gas phase only to deposit and grow into crystalline solid phase in the sink (region where crystal growth occurs). The latter, however, can have many variations depending on the complexity of compounds to be synthesized and the precursors available. This technique is employed when the precursors have relatively low vapor pressures at the given temperature; in such a case, a transport agent is used to convert the species into the vapor phase (by means of chemical bonding), transport them

to the sink region. The formation of the vapor phase compounds is a reversible process, so the transport agent is recycled – travels back and forth to transport more of the precursors species (Feigelson, 2015).

3.1.1 Sublimation Growth

Sublimation growth is a physical vapor deposition technique for growing high quality crystals with large domain size in a simple system configuration (see Fig. 11). The principle of sublimation involves, namely, sublimation (phase transition from solid to vapor) of powder precursors at an appropriate temperature (hot zone) where the vapor pressure is significantly high to enable growth within a reasonable time. Following the sublimation of the solid precursors, gas particles are transported towards a colder zone where deposition of gaseous species takes place resulting in crystal formation (see Fig. 11). This process is done in an open system and is facilitated by directional transport of gaseous species via an inert gas (e.g. Argon). The growth is generally described by equation (1). Compounds grown with this method are typically highly volatile.

$$AB_{x\,(s)} \overset{\Delta T}{\leftrightarrow} AB_{x\,(g)} \qquad (1)$$

Both thermodynamic and kinetic considerations are important; the former determines the stability of the compounds in the given conditions (temperature and pressure), while the latter determines the crystal growth rate which is affected by the temperature gradient and the (inert) gas flow rate. Considering the thermodynamics of the reversible process involved, these reactions are endothermic meaning that transport occurs from the hot zone (sublimation) to the cold zone (deposition).

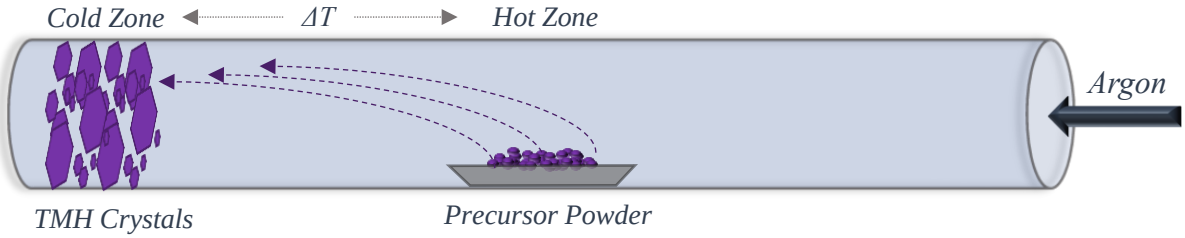

Fig. 11 | Illustration of crystal growth by sublimation method. The growth is performed inside of a quartz tube with a constant flow of an inert gas that transports the sublimed species from the hot zone towards the cold zone where crystallization occurs.

Under appropriate conditions, sublimation of precursors can lead to decomposition into other gaseous species which are then re-crystallized in the colder region. The growth for these reactions is performed at higher temperatures at which the precursor compound becomes unstable; these reactions are governed by the general equations (2) and (3).

$$AB_{x\,(s)} \overset{\Delta T}{\leftrightarrow} A_{(g)} + xB_{\,(g)} \qquad (2)$$

$$AB_{x\,(s)} \overset{\Delta T}{\leftrightarrow} AB_{y\,(g)} + (x-y)B_{\,(g)} \qquad (3)$$

Both sublimation and decomposition sublimation techniques are endothermic processes and fall within the scope of auto-transport reactions. That is, the precursors volatilize and transport themselves (either as a compound in the vapor form, or as decomposed vapor species that re-crystallize in the cold zone) without the need for an external agent.

3.1.2 Chemical Vapor Transport

Transport of vapor species in the presence of a temperature gradient is also the fundamental principle in CVT. The distinguishing characteristic of this growth technique is the necessity to convert non-volatile species into more volatile ones by means of a transport agent (Binnewies, Glaum, Schmidt, & Schmidt, 2012). This means that the transport agent chemically bonds to the precursor species converting it into a gas phase compound that can be transported and crystallized in a different region. Another difference compared to sublimation growth is that CVT is performed in a high-pressure (closed system) environment – that is, a quartz ampoule where precursors are sealed in vacuum and volatilize upon heating to the growth temperature (see Fig. 12).

This technique can be performed in various pathways depending on the desired final product and available precursors. For instance, crystal growth can be performed via a transport agent that stays out of the final product (e.g. Iodine), but some crystal growth can be performed by using a transport agent that will (partially) enter the crystal structure of the product (e.g. Tellurium chloride). Generally, the transport agent is recycled, meaning that it re-enters the reaction after transporting the chemical species to the growth zone (Binnewies et al., 2012). The general chemical equation describing CVT reactions is shown in equations (4) and (5).

$$AB_{x\,(s)} + nC_{(g)} \overset{\Delta T}{\leftrightarrow} AC_{n\,(g)} + \frac{x}{y}B_{y\,(g)} \qquad (4)$$

$$AB_{x\,(s)} + nCD_{(g)} \overset{\Delta T}{\leftrightarrow} AC_{n\,(g)} + \frac{x}{y}B_{y}D_{(g)} \qquad (5)$$

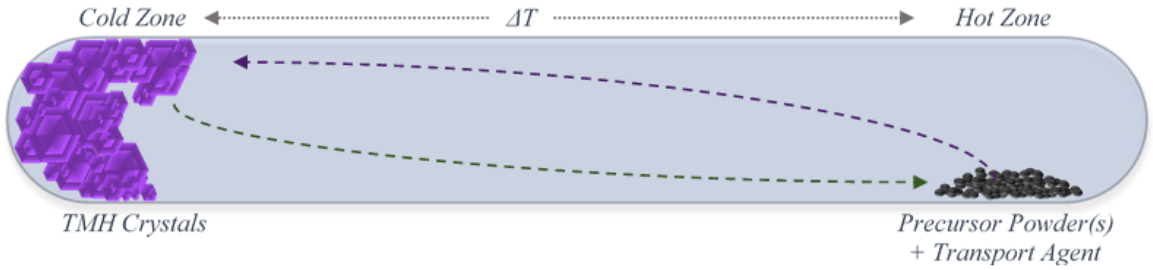

Fig. 12 | Illustration of crystal growth by CVT method. Note the direction of growth from hot to cold is appropriate only for endothermic reactions; in case of exothermic reactions, transport of species occurs from the cold to the hot zone. Purple arrow indicates transport of species from source to sink, while green arrow indicates return of the transport agent to re-enter the transport reaction.

The main considerations that are relevant in CVT crystal growth are thermodynamic based. Kinetics does not play a significant role in this type of growth due to the nature of the growth environment (Binnewies et al., 2012). As far as reaction kinetics is concerned, the main parameter that can be used to control transport rates is temperature gradient. Naturally, lower transport kinetics yield higher quality crystals due to the allotted time for atomic and/or molecular species to orient and form in particular crystal structures. However, from a thermodynamics standpoint, many conditions must be met to enable high quality crystal formation. First, the temperature in the source region must be appropriate for precursors to either volatilize, decompose, or convert to gaseous species by means of reacting with the transport agent. The growth temperature must be appropriate as well; in case of an exothermic reaction, the sink zone should be at a higher temperature than the source, and for an endothermic reaction – at a lower temperature. The crystal formation will only occur if the temperature in the sink area is high enough for crystallization to occur (due to the presence of an activation energy for crystallization), but low enough for the crystals to be stable (solid phase).

The transport agent must be selected carefully since it is to transport all precursors and it must therefore be able to react with all of them. The transport agent also must be highly volatile or decompose in the given source temperature. Time is another important parameter; depending on the transport kinetics, time must be allotted for all precursors to react and transport in order to ensure precise stoichiometry of the final product. That is, precursors with various transport rates can put the stoichiometry off if they are not allowed to react completely. The parameter that also affects the transport rate of precursors is surface area. Precursors with larger surface area (e.g. fine powders) will naturally react with the gaseous species faster than precursors that have lower exposed surface (e.g. elemental chunks). Finally, the crystal quality will largely depend on the quality of precursors used; purer precursors will yield crystals with lower defect density.

In this work, parent compounds have been grown in two ways: by sublimation growth, and by using CVT. The latter was, in some cases, performed by starting with compound-type precursors (TMH powders) and in other cases by starting with elemental powders (including a transport agent). Alloy compounds were all synthesized using CVT.

3.2 Characterization Methods

Characterization is the most essential tool in materials science that enables scientists to identify the materials that they are working with, determine their properties, as well as confirm new discoveries. The following techniques that are discussed in short below are essential to learning about the properties of the new alloy compounds synthesized in this work.

3.2.1 Raman Spectroscopy

Raman spectroscopy is a fundamental characterization technique used for identifying crystalline compounds. It is an optical technique that utilizes laser (from IR, visible and up to the UV range) to excite the atoms / molecules in the sample which generate scattered electromagnetic radiation (Wolverson, 2008). The Raman scattering process is different than the most common type of scattering from materials (Rayleigh scattering) and it occurs more rarely. Rayleigh scattering is an elastic process and it involves scattering of light with the same frequency as the incoming light. On the other hand, under specific conditions, the laser radiation can excite vibrational modes in the crystal lattice of a solid-state material (optical phonons) which can alter the energy of the scattered radiation changing its frequency (see Fig 13). The condition that must be met for Raman modes to be active is polarizability of the material; in polarizable systems, a dipole moment is induced by the incoming photon energy and the electron clouds get deformed by the external electric field (Principles, 2009).

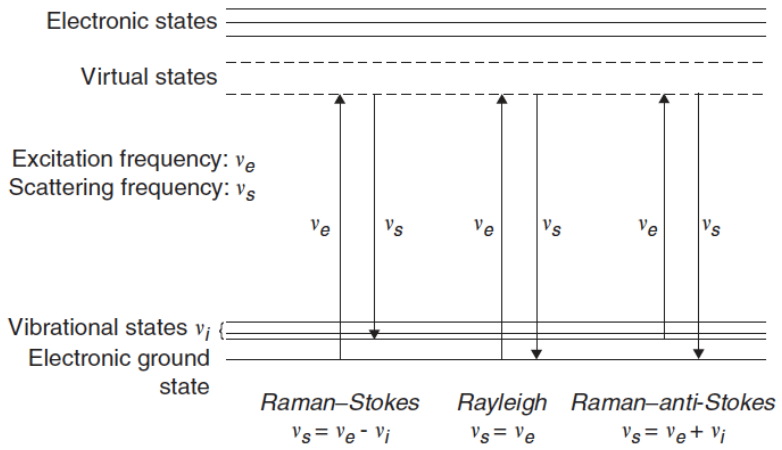

Fig. 13 | Raman-Stokes scattered light (E > E0), Rayleigh scattered light (E = E0), Raman-anti-Stokes scattered light (E < E0). (Lewandowska & Liu, 2016)

Based on the type of photon-phonon interaction, the scattered photon can have higher energy (Stokes scattering) or lower energy than the incident photon (anti-Stokes scattering). Due to the unique nature of crystalline structures, there will be specific Raman peaks associated with each material depending on the polarizability of the atoms which can then be used to identify the compound. Further information that can be derived from a Raman spectrum include sample crystallinity or quality, defects in the crystal structure, anisotropy, phase transitions, effects of temperature and strain etc. (Lewandowska & Liu, 2016).

In this work, Renishaw Raman system was used with operating laser of 488 nm wavelength. Prior to the measurement, bulk samples are exfoliated a few times using scotch tape until a thin enough sample is achieved which is the transferred onto a clean Si/SiO_2 substrate (oxide layer 285 nm). The substrate provides enough contrast to enable visualization of very thin flakes using an optical microscope. The power level, exposure time, and number of accumulations are varied depending on the stability of samples as well as the signal intensity.

3.2.2 Scanning electron microscopy

Scanning electron microscopy (SEM) is an imaging technique that utilizes an electron beam (as opposed to light) to raster scan a specimen and reveal microscopic topographical and compositional features that are impossible to resolve via a traditional optical microscope. Compared to optical microscopy, SEM has higher resolution (~ 10 nm) and depth of field enabling the production of a 3D image of the specimen analyzed. The instrument operates under vacuum to allow the electron beam to travel from the

source to the specimen and then to the detector without scattering. Imaging is usually performed in two main modes: secondary electron (SE), and backscattered electron mode (BSE). SE imaging is used to generate topographic contrast via detection of the inelastically scattered valence electrons from the specimen. BSE imaging is used to generate compositional contrast via detection of the elastically (back-) scattered electrons that interact with the atomic core of the elements in the specimen (Leng, 2013a).

The SEM instrument used in this work is an Amray 1910 FE-SEM operated under SE mode with accelerating voltage of 15 – 20 keV (depending on the sample). All samples were mounted in the bulk form on top of sample holders coated with carbon tape. Then, samples were coated with a layer of gold (thickness ~ 10 nm) on the surface in order to reduce charging effects that are present in semiconducting and insulating samples.

3.2.3 Energy dispersive spectroscopy

The scanning electron microscope is commonly equipped with an X-ray energy-dispersive spectrometer (EDS) that is used to analyze the chemical composition of the specimen. As such, an additional EDS detector is placed in the SEM instrument to capture the characteristic X-rays emitted by the bombardment of the specimen with the electron beam. The process of X-ray emission begins with the ejection of inner core electrons from the specimen atoms. The empty electron state gets filled by an upper shell electron via a transition that lowers the energy of the system. The energy associated with this transition is emitted in the form of an X-ray photon with specific wavelength. The energy difference between electron shells are unique for each atom, allowing the

identification of the elements in the sample by detecting the X-rays with specific energy (Leng, 2013b). The EDS instrument used in this work is an EDAX Ametek X1 Analyzer and it is coupled with the SEM instrument described above. Samples were simultaneously imaged and analyzed for elemental composition using a working distance of ~ 12 mm, and a tilt angle of ~ 30°.

3.2.4 X-Ray diffraction

X-ray diffraction (XRD) is a crystal structure characterization technique that utilizes a monochromatic X-ray beam (characteristic X-ray) to scan through a crystalline sample and obtain information about the planar spacing. X-rays are electromagnetic waves with a much shorter wavelength than visible light; using these waves of length on the order of ~ 0.1 nm allows for features within the crystal structure to be resolved at the nanoscale (Leng, 2013c). The working principle in XRD involves Bragg's Law which states that there is a relationship between the crystallographic interplanar spacing and the scanning angle (of the X-Ray beam). Equation (6) describes this law, where n = integer, λ = wavelength of light, d = interplanar spacing, θ = incident angle.

$$n\lambda = 2dsin\theta \qquad (6)$$

The X-ray beam is reflected off of different (parallel) planes in a crystal; the reflected X-rays can be in-phase (where they constructively interfere), or out-of-phase (where they destructively interfere leading to partial or complete cancellation). According to Bragg's law, the X-rays are in-phase when equation 6 is satisfied in which case the diffracted beam is composed of constructively interfering X-rays which is then detected by the instrument (see Fig. 14). The XRD spectrum will then display the incident angles

and the associated intensity of the reflections from those angles. Information about the interplanar spacing (d_{hkl}) of the relevant planes {h k l} can be extracted from that data by using equation 6 with a value of 1 for n.

The instrument used in this work to perform XRD measurements is the Malvern PANalytical Aeris X-ray powder diffractometer, Research Edition with a CuKα excitation source with wavelength λ = 0.1542 nm. Samples of single crystal TMH flakes were laid flat on the sample holder and in some cases some ethanol was applied to the top in order to help stick the sample to the holder.

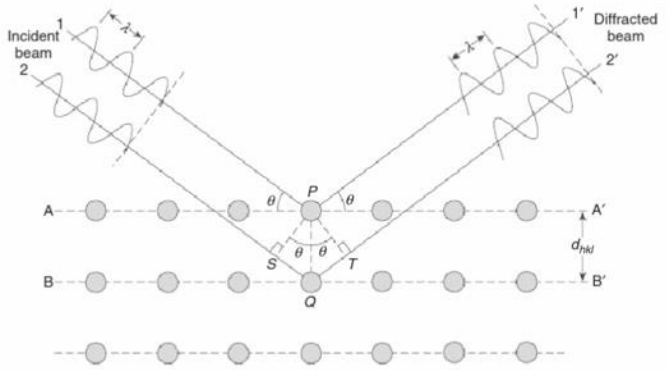

Fig. 14 | Illustration of Bragg's law. SQ + QT = 2PQ sinθ. (Leng, 2013c)

3.2.5 Vibrating sample magnetometry

Static magnetic properties of the 2D TMH bulk crystals are characterized via vibrating sample magnetometry (VSM). In this technique, the sample is mounted on a sample holder in either a parallel or perpendicular orientation (in reference to the magnetic field direction). The sample is then placed between two electromagnet poles that have pick-up coils attached to them. During the measurements, the sample is vibrated at a specific and constant frequency (see Fig. 15); the magnetic moment changes and as a

result, an AC voltage gets induced in the coils leading to a magnetic moment signal to be detected by the attached lock-in amplifier (Camley, R. E., Celinski, Z., & Stamps, R. M., 2015). The physical property measurement system (PPMS) has capability to reduce the specimen temperature down to 2K allowing for magnetic measurements to be performed at cryogenic temperatures. There are different types of measurements and information that can be retrieved from VSM data; the most informative measurement is a graph of the magnetic moment as a function of the applied field. Furthermore, magnetic moment can be measured as a function of temperature, revealing information about the Curie or Néel temperature of the specimen.

The VSM measurements are conducted on a Quantum Design PPMS System Model 6000. Samples are loaded in the bulk form in both parallel and perpendicular configurations (in reference to the crystallographic ab-plane) using special sample holders made of brass and/or quartz. Magnetic moment versus temperature and magnetic moment versus field measurements are collected in a zero-field cooled environment.

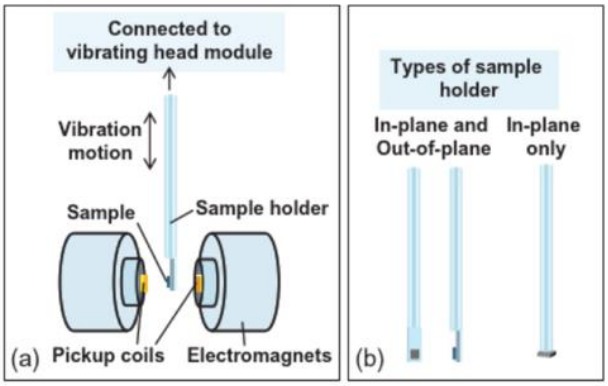

Fig. 15 | Simple illustration of the VSM system setup showcasing: (a) the sample and pickup coils that detect the material magnetic moment signal, (b) different orientations of the sample in reference to the magnetic field. (Camley, R. E., Celinski, Z., & Stamps, R. M., 2015)

4. ALLOYING IN TRANSITION METAL HALIDES

4.1 Literature review and motivation

Developing functional devices in the above-mentioned fields including spintronics, opto-electronics, magneto-optics etc., requires more than just the appropriate materials; tuning the material properties controllably such as optical bandgap, Curie or Néel temperature, magnetic anisotropy and so forth, is of utmost importance to achieve the desired device performance. One way in which properties of TMH magnetic materials were controlled in a recent study is via alloying and varying the anion ratio in ternary compounds.

The first research work was done on the alloys of chromium trihalide compounds, namely $CrCl_{3-x}Br_x$, and $CrBr_{3-x}I_x$. The study reveals that by varying the amount of Bromine in the former alloy structure, spin-orbit coupling can be tuned giving control over magnetic anisotropy; the study demonstrates how halide concentration can be utilized to transform the easy-axis from in-plane to out-of-plane and vice versa (Abramchuk et al., 2018). Interesting results of this study demonstrate a linear relationship between energy bandgap, crystal interplanar spacing, and Curie temperature to the content of bromine in the $CrCl_3$ parent compound (see Fig. 16).

Similarly, another study was performed on the same materials system, this time with a focus on chromium iodide-bromide alloy ($CrI_{3-x}Br_x$) (Siena et al., n.d.). The findings were not very conclusive and did not provide an in-depth understanding of the conclusions regarding the anionic ternary alloy. These two articles consist of the entire literature that has been, to date, published on the topic of alloying transition metal halide magnetic materials. Clearly, there is a need for more fundamental studies on the synthesis

of TMH alloy compounds, an area holding a lot of potential for establishing the playing grounds and tuning capabilities in these material systems. Exploring this uncharted territory will provide space to better understand magnetism in the bulk of vdW materials which will then give insight into magnetism in the 2D limit.

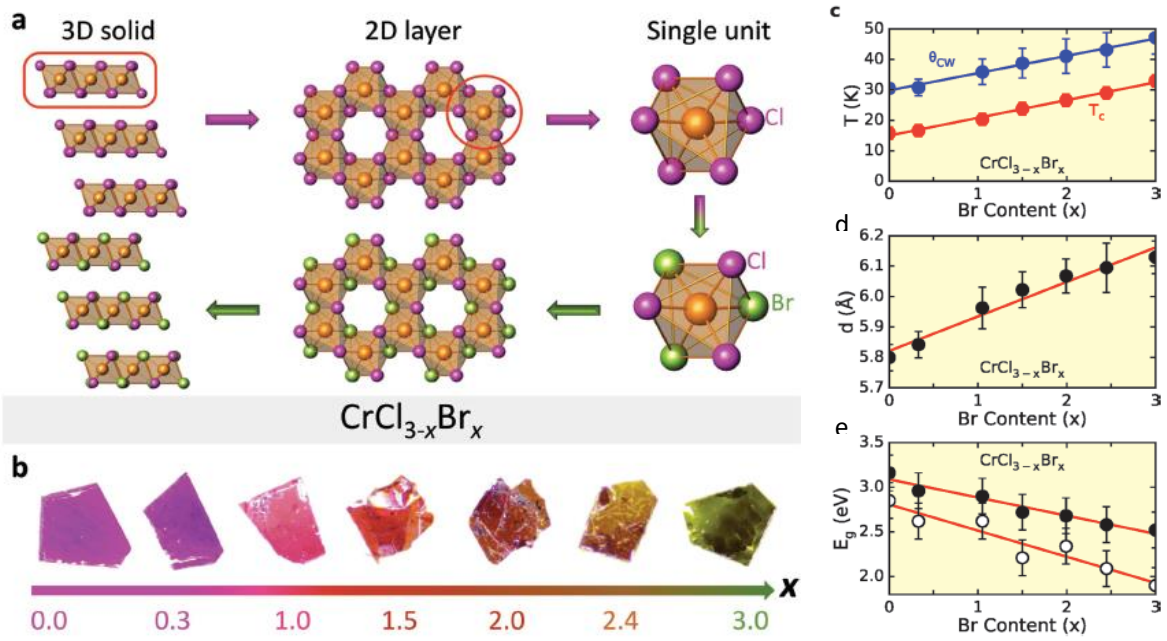

Fig. 16 | Illustration of $CrCl_{3-x}Br_x$ alloy: a) crystal structure of parent compound ($CrCl_3$) and alloy compound ($CrCl_{1.5}Br_{1.5}$), b) optical images showcasing color evolution of alloy between the two parent compounds, c) increasing T_c with Br content, d) increasing d-spacing with Br content, e) decreasing optical bandgap with Br content (Abramchuk et al., 2018).

Alloying the anion element is one method to engineer material properties in MX_2 and MX_3 structures. This method is advantageous due to the typical similarity between the associated parent compounds with a different halide element. That is, from an electronic standpoint, the number of valence electrons is the same across the different halides. Variability is introduced as a result of the halide atomic size, leading to changes in metal-halide bond length / bond strength. The halide atoms available for alloying are

limited to chlorine, bromine, and iodine. Fluorine TMH structures are not two-dimensional, rather, due to the large electronegativity of fluorine atoms, transition metal (di- and tri-) fluorides tend to adopt three-dimensional crystal structures (McGuire, 2017). The limited engineering space via anionic alloying motivates this work, where the engineering of TMH properties is done via cationic alloying.

Transition metals span a large space in the periodic table. Characteristic of these elements is their partially filled d-bands (with the exception of group 10 elements) which grants them vastly different electronic properties (Haotian Wang, Yuan, Sae Hong, Li, & Cui, 2015). Thus, it is naturally expected to observe vastly different magnetic properties between TMH compounds of different metal cations. Alloying by cationic mixing opens up a larger library of potential ternary compounds that can lead to new findings in terms of crystal phases and their associated magnetic properties. This thesis presents the synthesis and characterization of two novel TMH cationic alloys, and discussion on a phase-separated ternary compound, regarding which no other publication has been found to date. Future directions and potential of this work is discussed in the concluding chapter.

4.2 Synthesis and characterization of parent compounds

Before delving into alloying, the parent compounds of several transition metal halides were synthesized using two crystal growth methods: sublimation growth, and chemical vapor transport. The former method was used for synthesis of $CrCl_3$, and $NiCl_2$. CVT was used to grow crystals of $MoCl_3$, and $CoCl_2$, $FeCl_3$. Some relevant properties of

these compounds are showcased in Table 1 below, whereas Table 2 summarizes the growth method and associated parameters for each parent compound. Figure 20 illustrates the crystal structure of (most) TMH compounds; The MCl_2 (M = Ni, Co) compounds discuss here adopt the $CdCl_2$ structure, while the MCl_3 (M = Cl, Mo, Fe) compounds adopt the $AlCl_3$ structure at room temperature except $FeCl_3$ which can adopt the BiI_3 rhombohedral ($R\bar{3}$), trigonal Ti_3O (P321), or ($P\bar{3}$) crystal structure. Note that these compounds commonly undergo a phase transition at low (or high) temperature leading to changes in their magnetic properties as will be discussed below.

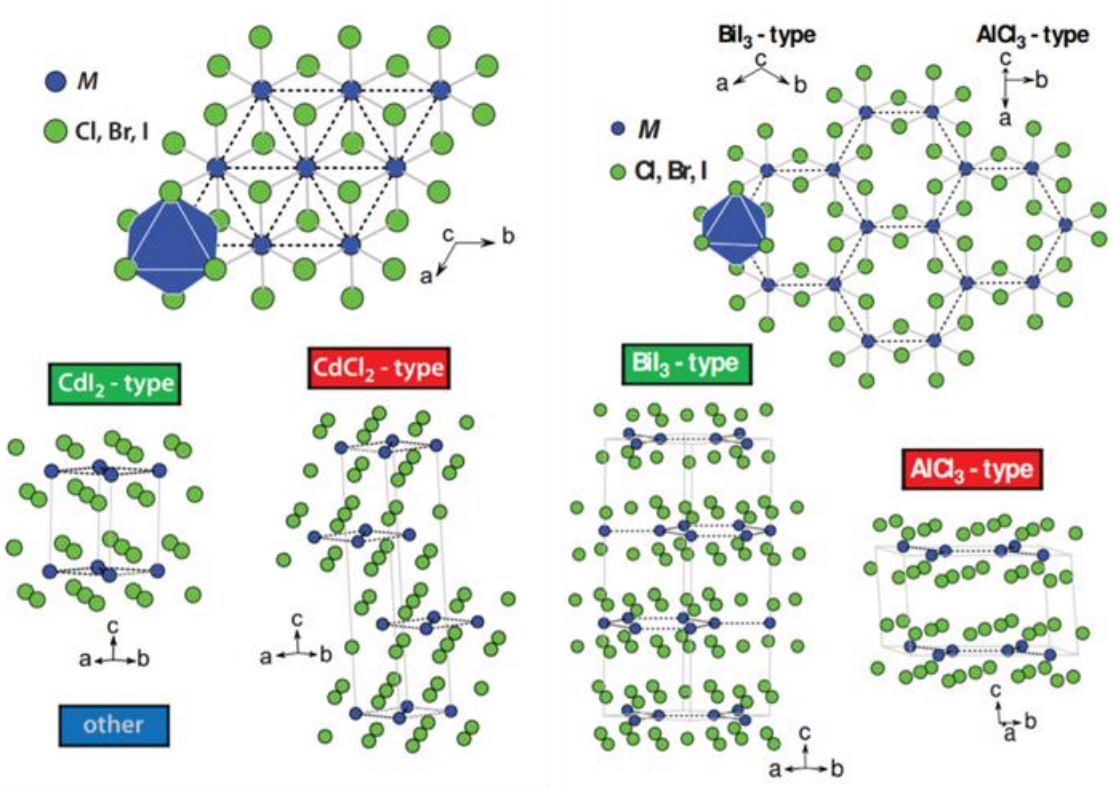

Fig. 17 | Crystal structure illustration for most TMH compounds. (McGuire, 2017)

Table 1. Properties of parent TMH compounds. Note that HM stands for helimagnetic behavior which occurs when there are competing magnetic interactions between AFM and FM magnetic order (McGuire, 2017; Tomar et al., 2019).

Compound	Structure	Global magnetic order	In-plane magnetic order	T_c or T_N (K)	θ (K)	d_{hkl} (nm)
$CrCl_3$	C2/m	AFM	FM II	15	27	0.344
α-$MoCl_3$	C2/m	Diamagnetic	Diamagnetic	-	-	0.599
$NiCl_2$	R$\bar{3}$m	AFM	FM II	52	68	0.580
$CoCl_2$	R$\bar{3}$m	AFM	FM II	25	38	0.581
$FeCl_3$	R$\bar{3}$, P321*, or (P$\bar{3}$)	HM*	HM*	10*	-11*	0.580

Table 2. Summary of crystal growth conditions of parent TMH compounds.

Compound	Synthesis method	Hot zone T (ºC)	Cold zone T (ºC)	Precursors	Growth time (hrs)	Argon flow rate (sccm)
$CrCl_3$	Sublimation	700	600	$CrCl_3$ powder	6	20
$CrCl_3$	CVT	700	550	$CrCl_3$ powder	48	-
α-$MoCl_3$	CVT	470	360	Mo, $TeCl_4$ powders	72	-
$NiCl_2$	Sublimation	700	550-690	$NiCl_2$ powder	6	20
$CoCl_2$	CVT	720	590	Co, $TeCl_4$ powders	72	-
$FeCl_3$	CVT	230	180	$FeCl_3$ powder	42	-

4.2.1 $CrCl_3$

Owing to its great stability in ambient conditions and ease of synthesis, chromium tri-chloride is one of the most studied TMHs. This compound is known to adopt the $AlCl_3$ monoclinic (space group C2/m) crystal structure with hexagonal symmetry at room temperature, and undergo a phase transition to the BiI_3 rhombohedral ($R\bar{3}$) structure below 240 K as shown in Fig.17 (McGuire, 2017). Paramagnetic at room temperature, $CrCl_3$ becomes antiferromagnetic below ~ 15 K. The moment within a single layer is ferromagnetic with the easy axis in the XY plane, while alternating layers adopt antiferromagnetic order against each other.

Fig. 18 | Images of $CrCl_3$ crystals grown by sublimation or CVT technique. Note the large domains of single crystals in the millimeter range.

Synthesis of this compound was performed via sublimation of $CrCl_3$ powder under two environments: in a single-zone furnace (open-system), and a quartz ampoule (closed system). Both methods produced similar quality crystals with a few millimeters' domain size (see Fig. 18). First, $CrCl_3$ growth was conducted in a single-zone furnace using $CrCl_3$ powder precursor (200 mg of anhydrous $CrCl_3$ flakes from Alfa Aesar with 99.9% metals basis purity) placed in an alumina crucible. Argon gas flow was kept for 5 min before ramping up the temperature at a rate of 22.5 ºC/min. After 7 hours of growth,

the furnace was turned off and the hood was lifted allowing for a natural cool-down rate. The gas flow was kept constant throughout the growth including the cool-down period. Precursors were not completely consumed during this growth; however, oxidation of chromium was noticed in the remaining precursors due to the change in color from purple to green (see Fig. 19). The oxidation can be attributed to the open-system setup as well as precursors purity (considering that all TMH compounds are, to different extents, hygroscopic). Crystals nucleated and grew on the inside walls of the quartz tube. All other synthesis via sublimation in an open system is performed in a similar fashion.

The second growth method within a closed quartz ampoule was performed similarly starting from the same $CrCl_3$ powder precursors (380 mg) in a temperature gradient as described in Fig. 19. The precursors were loaded inside of a cleaned quartz ampoule and sealed under a vacuum environment (10^{-5} Torr). Growth proceeded in a two-zone furnace for 48 hours with most of the precursors having transferred to the growth zone. Small amounts of precursors are noticed in the source region, and the (green) color indicates oxidation of chromium. To avoid bursting the quartz ampoule, the furnace temperature was increased at a rate of 2.8 ºC/min, while cooling was done naturally inside the furnace (rate ~ 3-4 ºC/min). To avoid formation of oxides, future growth should be conducted using precursors that have been previously heated to remove any adsorbed water species. All other synthesis via sublimation in a closed system is performed in a similar fashion. CVT growth from elemental precursors is described in more detail below.

The layered structure of $CrCl_3$ can be clearly visualized in SEM images as shown below in Fig. 22. The underlying hexagonal crystal structure yields hexagonal symmetry

even in the macro and micro-scale as can be seen from the optical and SEM images. Elemental analysis using EDS (Fig. 22) confirms the presence of chromium and chlorine in the sample. The stoichiometry of the sample according to EDS is slightly off, as is expected considering the small atomic size of chlorine and the limited resolution of the instrument. However, other characterization techniques are used to confirm the 1:3 stoichiometry of the crystals grown.

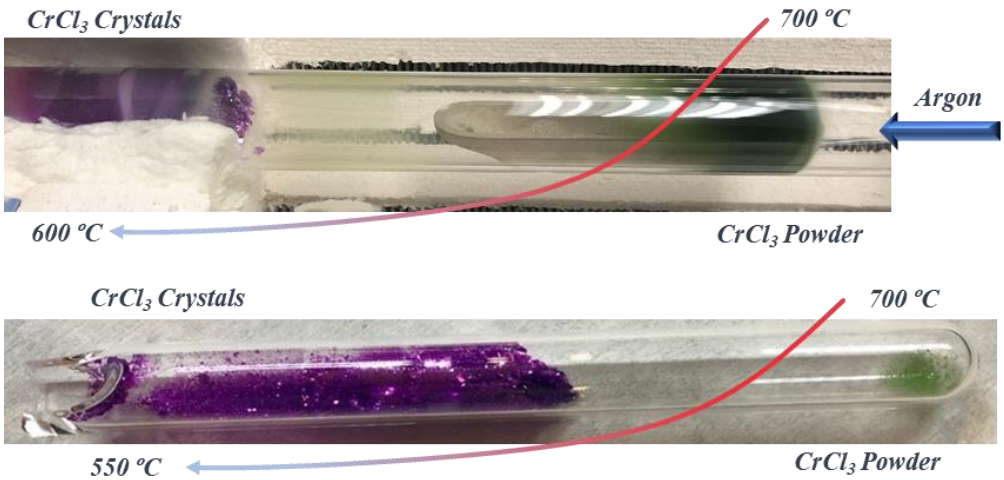

Fig. 19 | Experimental setup for open-system growth (top) and closed-system growth (bottom). Note the green color due to the oxidation of chromium in the source regions.

Raman analysis (Fig. 21) performed on exfoliated flakes identifies the characteristic $CrCl_3$ peaks at 163, 206, 245, 299, and 343 cm^{-1} which is known from previous literature (McGuire, Clark, et al., 2017). Finally, the crystal structure (C2/m) was confirmed via XRD analysis shown in Fig. 21 where peaks are identified at the angles labeled in the inset of the graph. These peaks are associated with the reflection planes of the family {0 0 1} due to the measurement technique. That is, single crystals were mounted flat on the sample holder with the (0 0 1) plane parallel to the holder. Knowing the X-ray wavelength, the reflection planes, and the associated incident angles,

interplanar spacing of the planes causing the detected reflections in the XRD data are calculated using Bragg's law as described in section 3.2.4 (Chapter 3). The interplanar spacing (d_{hkl}) for the relevant is also included on the inset in the XRD data below (see Fig. 21).

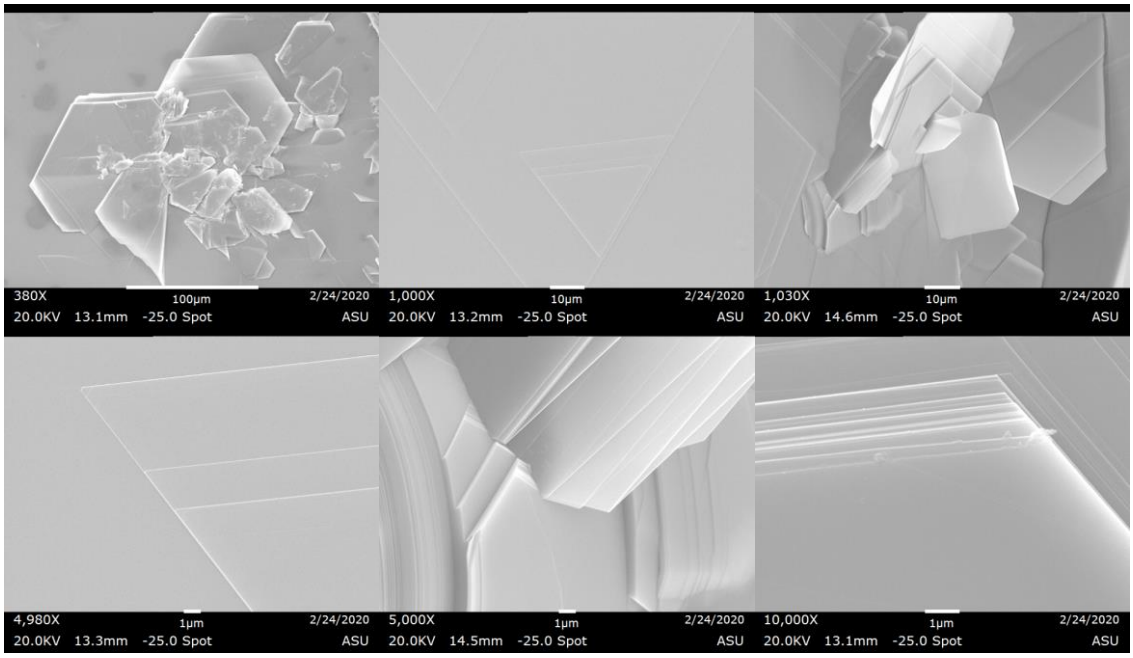

Fig. 20 | Scanning electron microscopy of $CrCl_3$ crystals. Note the hexagonal symmetry and layered structure which is characteristic of all 2D vdW materials.

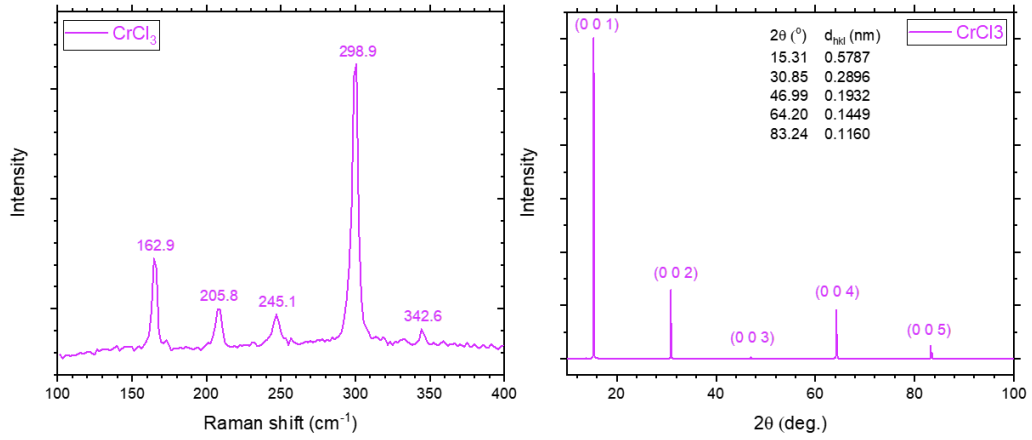

Fig. 21 | Raman spectrum (left) of exfoliated $CrCl_3$ onto a Si substrate with SiO_2 top-layer of 285 nm thickness. XRD spectrum (right) of bulk crystal flakes detailing the interplanar spacing of the reflecting planes.

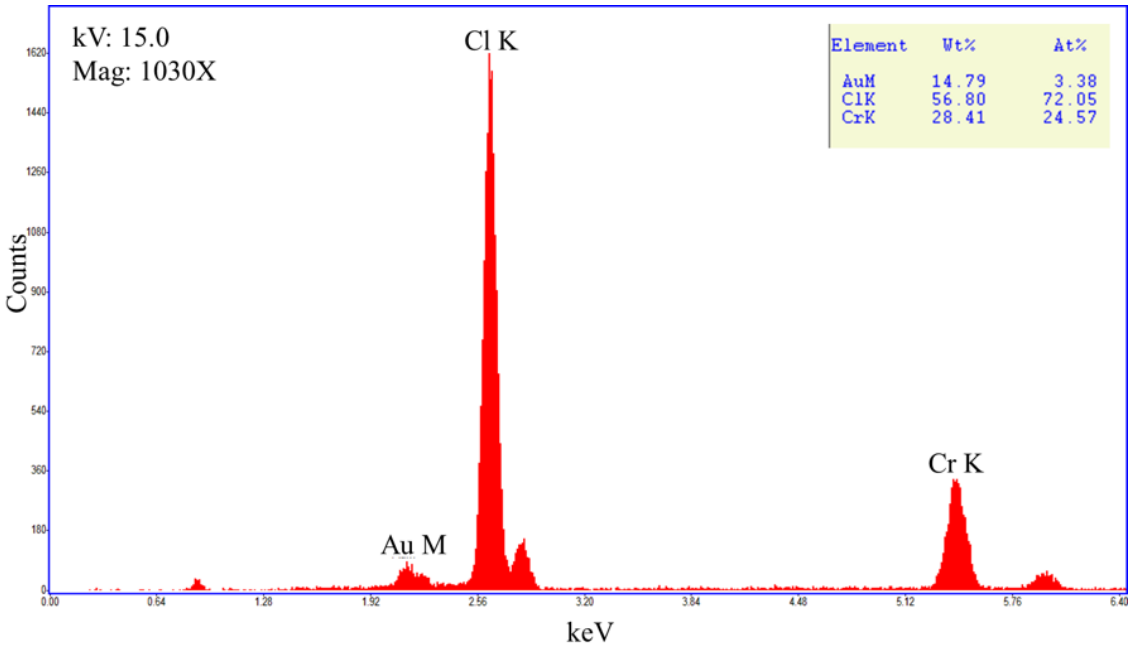

Fig. 22 | Energy dispersive spectrum of $CrCl_3$ showcasing elemental analysis of the crystals. Note: the labels (K, M) are associated with specific transitions within electron shells leading to the observed characteristic X-rays. Inset shows quantitative analysis of the elements detected.

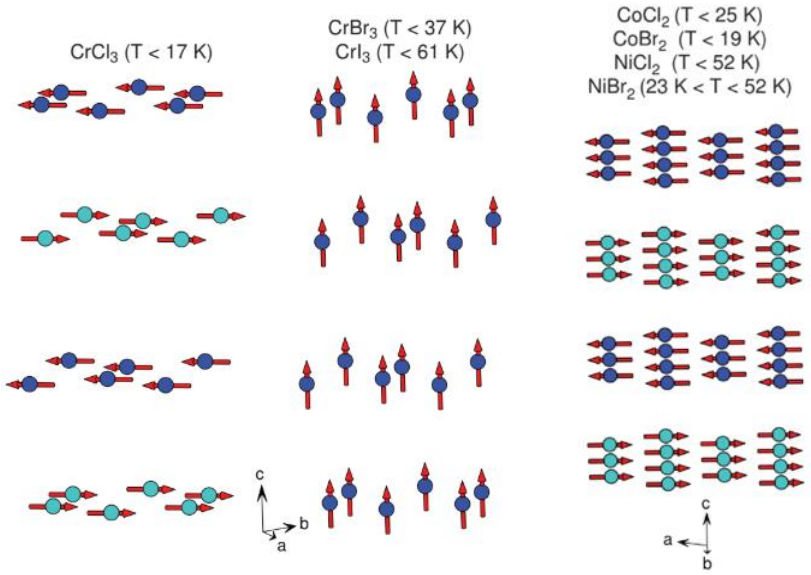

Fig. 23 | Magnetic moment orientations in parent TMH compounds showing AFM behavior for $CrCl_3$, $NiCl_2$, and $CoCl_2$ between layers (and FM within layers) below their respective Curie temperatures. Easy-axis in all three compounds is in the ab-plane, while some other compounds ($CrBr_3$, and CrI_3) are easily oriented out-of-plane (McGuire, 2017).

Chromium halide compounds are known to have global antiferromagnetic ($CrCl_3$) or ferromagnetic ($CrBr_3$, and CrI_3) behavior. Fig. 24 shows the susceptibility (unitless) of $CrCl_3$ bulk crystal as a function of temperature. Notice how the high temperature region appears to have an inverse relation to temperature which is characteristic of paramagnetic materials according to Curie-Weiss law which states the following (χ = susceptibility, C = material Curie constant, T = temperature, T_C = Curie temperature).

$$\chi = \frac{C}{T - T_C} \qquad (7)$$

The inset shows a plot of inverse susceptibility versus temperature, which is linear at high temperatures with a Weiss constant θ ~ 29 K, as expected from literature (McGuire, 2017). In the lower temperature region, susceptibility reaches a maximum around 14-15 K, followed by a reduction with further decreasing temperature. This behavior is typical of antiferromagnetic materials (Ashcroft & Mermin, 1968) and the peak indicates the region where paramagnetic to antiferromagnetic transition takes place. Reported Curie temperature for $CrCl_3$ (T_C ~ 14-17 K) agrees with these measurements. This material is, however, also known to exhibit ferromagnetic order at higher magnetic field values as is described in (McGuire, Yan, et al., 2017).

Normalized magnetization as a function of magnetic field shows that the two orientations are magnetized to saturation at different rates. In the c-axis orientation ($\perp$) the magnetization reaches saturation at fields higher than 0.6 T, while in the II orientation, maximum magnetization is reached above 0.2 T. This observation confirms the previously reported data that $CrCl_3$ has preferential orientation of magnetic moments (easy-axis) in the ab-plane versus out-of-plane, that is, $CrCl_3$ has an xy- easy axis (see Fig. 23). The discontinuity in the susceptibility versus temperature plot in the same figure

showcases the well reported phase transition that occurs around 255 K in which $CrCl_3$ converts from the $AlCl_3$ monoclinic (space group C2/m) structure to the BiI_3 rhombohedral ($R\bar{3}$) structure.

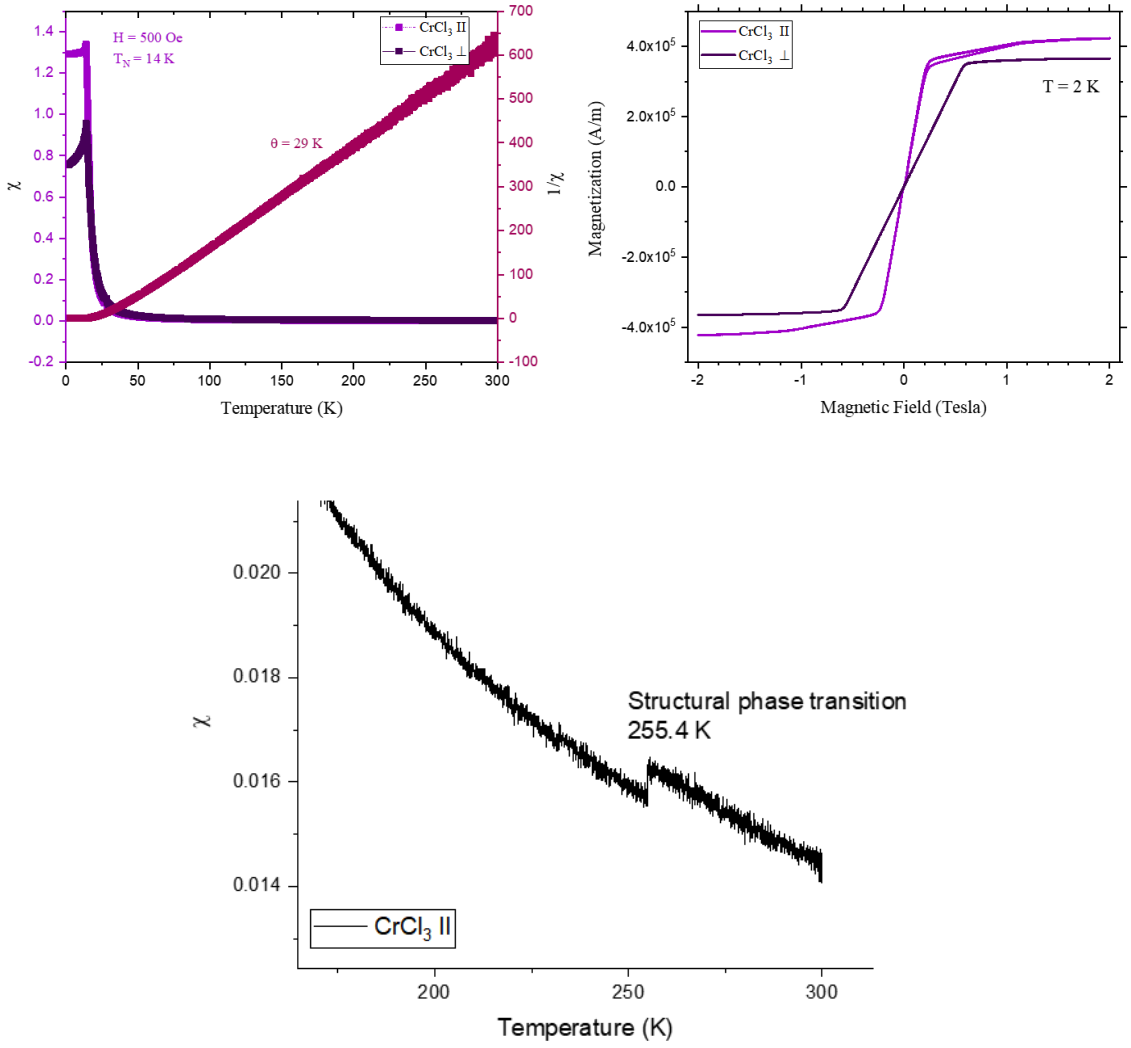

Fig. 24 | VSM measurements showcasing the susceptibility versus temperature (top left), and normalized magnetization versus magnetic field (top right). Bottom plot shows a distortion in the susceptibility around the temperature where phase transition occurs.

4.2.2 α-$MoCl_3$

This TMH compound is rather special considering that molybdenum belongs to the 4d transition metals period in which case the spin-orbit coupling can be more significant. The tri-chloride compound exists in two phases, namely, α-$MoCl_3$ and β-$MoCl_3$. The former is known to have a monoclinic crystal structure similar to that of $CrCl_3$ at room temperature (space group C2/m). The latter phase is described in either a C2/c space group, or a highly distorted C2/m space group with different stacking order than the α-phase.

Synthesis of this compound is more complex than the chromium based TMH. The reason for this is the fact that this compound not only adopts two phases in the trichloride form (as mentioned above), but it also exists in other valence configurations ($MoCl_2$, $MoCl_4$, and $MoCl_5$) all of which are relatively low temperature compounds. Synthesis is made difficult because within a small temperature gradient, more than one phase can be stable and grow, reducing the yield or suppressing the growth of the desired phase.

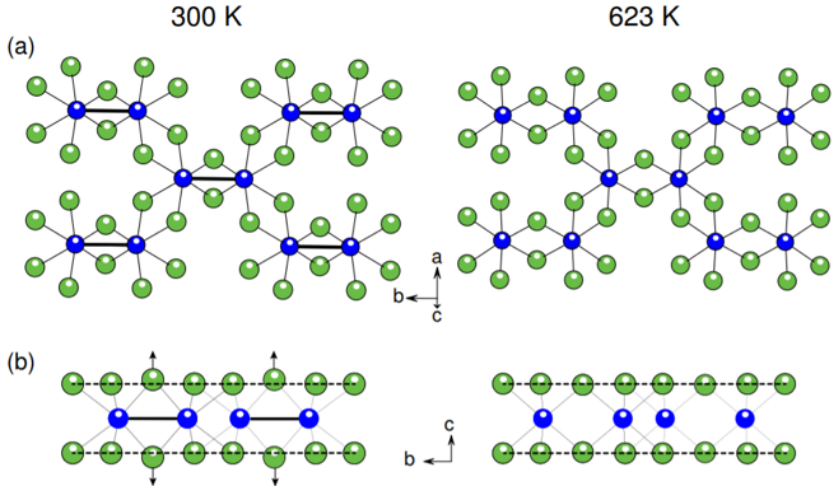

Fig. 25 | Dimerization in $MoCl_3$ illustrated by the solid dark lines between the molybdenum atoms (blue). Note the movement of chlorine atoms (green) due to the M-M interaction - marked with an arrow pointing outwards. (McGuire, Yan, et al., 2017)

Growth of this compound was achieved using elemental molybdenum (1-5 μm powder from Sigma Aldrich, 99.9% trace metals basis) and tellurium tetrachloride (crystalline $TeCl_4$ from Alfa Aesar 99.9% metals basis purity) as a transport agent and chlorine source. To preserve the purity of the moisture sensitive $TeCl_4$, precursors were loaded inside of a glovebox avoiding exposure to air. A total mass of 0.5 grams was loaded in a similar fashion as described before inside of a quartz ampoule and sealed under vacuum environments. The temperature was increased at a rate of ~ 2 °C/min up to 470 °C (hot zone) and 360 °C (cold zone), growth time kept at 72 hours, and cooling rate similar to the previous (naturally cooled) conditions described in 4.2.1. These growth conditions yielded small α-$MoCl_3$ crystal size (micron range) in the sink area and a second phase near the center of the quartz ampoule (which was not characterized). The source area in the ampoule had a small amount of precursor powders remaining that did not completely transport in the given growth period.

Based on the Raman analysis, the crystal phase that grew near the cold zone does match literature confirming its identity as α-$MoCl_3$. Due to the small crystal size, XRD data was rather noisy and as such was not included in this document. In order to obtain credible XRD pattern from this material, the crystal growth needs to be optimized to first eliminate the conditions that allow for the growth of a second (undesirable) phase and to yield larger crystals. The elemental analysis via EDS (see Supplementary Information) shows the presence of molybdenum and chlorine at a ratio close to 1:3 but slightly lower due to the underestimation of chlorine atoms as was found to be the case in all other compound characterization.

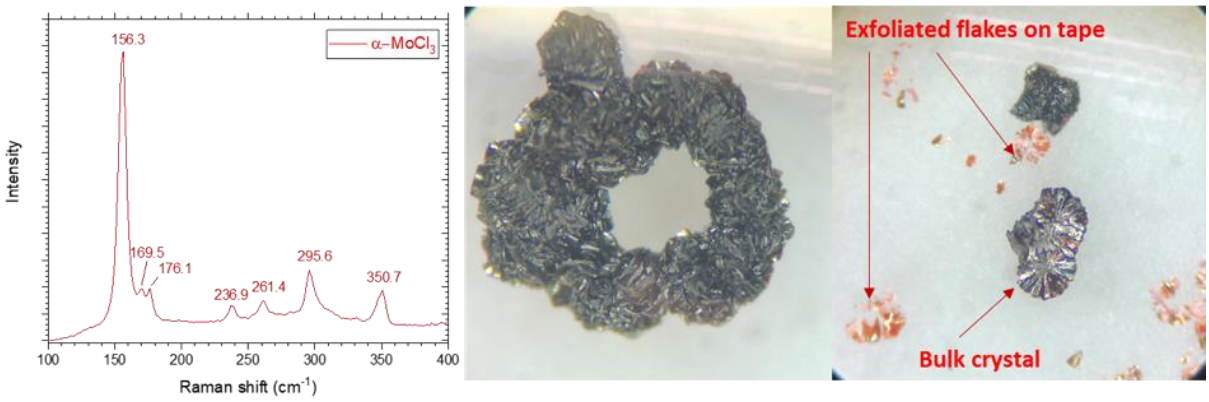

Fig. 26 | Raman data (left) and optical images (middle, right) of α-$MoCl_3$ crystals. Note the layered structure evident from the vertically stacked planes (middle) in the bulk crystal, further illustrated by the ease of exfoliating the crystal (right) into the imaged deep red colored thin flakes.

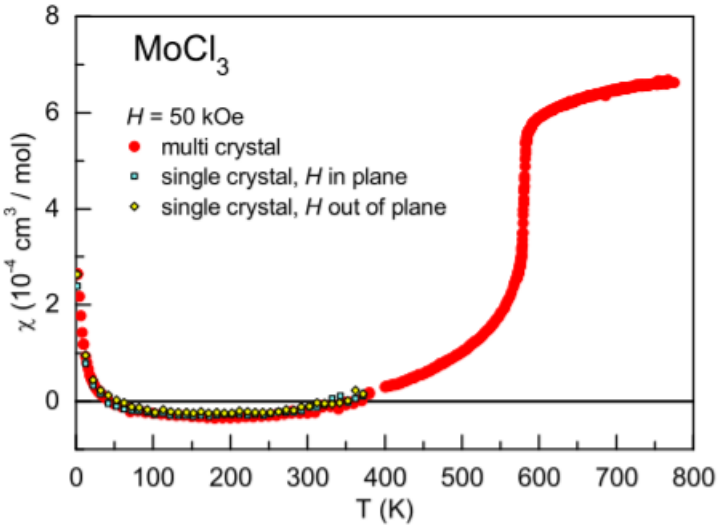

Fig. 27 | Susceptibility measurement of $MoCl_3$ showing transition from diamagnetic to paramagnetic and possible AFM order at high T. (McGuire, Yan, et al., 2017)

The magnetic properties reported for this compound identify it as weakly paramagnetic or diamagnetic at room temperature and below. The slight magnetic moments are attributed to the dimerization between molybdenum atoms (as shown in Fig. 25). However, high temperatures (623 K) were found to remove the dimerization between

metal atoms leading to stronger paramagnetic response. AFM behavior is predicted at higher temperatures than reported experimentally. This finding bring attention to this compound considering that magnetic materials can be implemented in practice only when their stability at standard conditions is achieved, while most other magnetic materials show FM or AFM order at cryogenic temperatures. Ideally, room temperature FM and AFM compounds will open up a lot of opportunity to enable device fabrication. The interest in alloying this compound is evidently to explore the effect of other metals (dopants) in altering the dimerization phenomenon and the magnetic response of the alloy at lower temperatures.

4.2.3 $NiCl_2$

Despite being studied to a lesser extent, $NiCl_2$ is also identified as an AFM vdW material with Néel temperature at 52 K. Sharing a chlorine atom between three atoms of (divalent) nickel, this compound adopts the rhombohedral $CdCl_2$ structure with space group $R\bar{3}m$ as illustrated in Fig. 17. A temperature dependent structural phase transition has not been reported for this compound.

As was mentioned in the beginning of this chapter, $NiCl_2$ was also synthesized via sublimation in an open-system configuration. Fig. 30 shows the system setup. Nickel dichloride (200 mg of anhydrous powder 99% metals basis purity from Alfa Aesar) was loaded inside of an alumina crucible which was placed in the center of a single-zone furnace under a constant flow of Argon. The precursor was loaded inside of the glovebox to limit the time of exposure to air. Growth proceeded in the same way described in the $CrCl_3$ growth with the conditions listed in Table 1.

This compound has extremely low Raman signal and is quite robust to the high-power laser used for characterization. Despite this, peaks at 171, and 266 cm^{-1} are detected which is in line with reported values from literature (Lockwood et al., 1979). Elemental composition showing the presence of nickel and chlorine in the compound was characterized via EDS and the data is included in the Supplementary Information (SI) at the end of this document. As mentioned before, the detection of chlorine atoms is lower than the expected concentration due to the limitations of the instrument when detecting smaller atoms. Crystal structure is confirmed via XRD analysis included in Fig. 29 showing peaks at 15.36, 30.95, 47.16, 64.46, and 83.61 degrees which is in agreement with expected signal from the {0 0 3} family of planes that is generated by the rhombohedral $NiCl_2$ phase ($R\bar{3}m$).

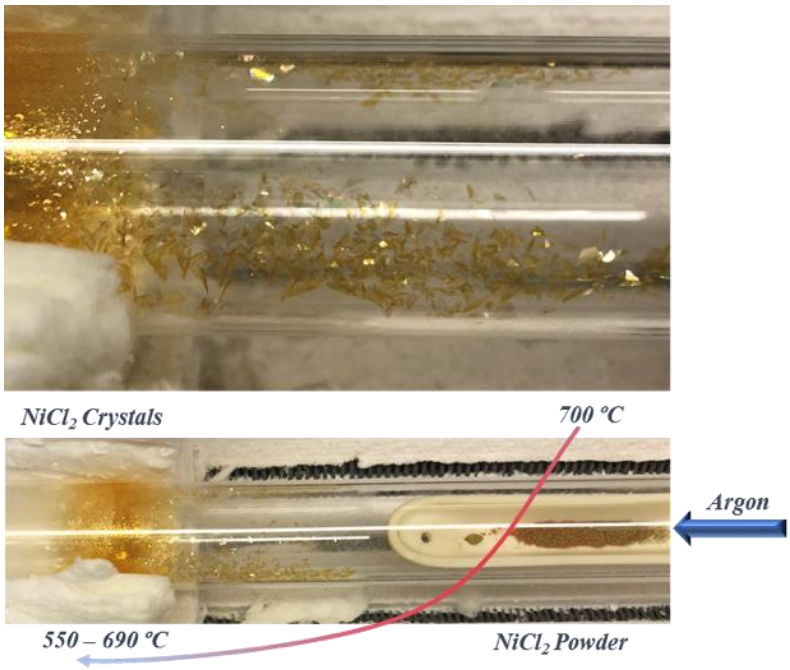

Fig. 28 | Images of $NiCl_2$ crystals within quartz tube showing the characteristic yellow color (top), and setup of the synthesis system (bottom).

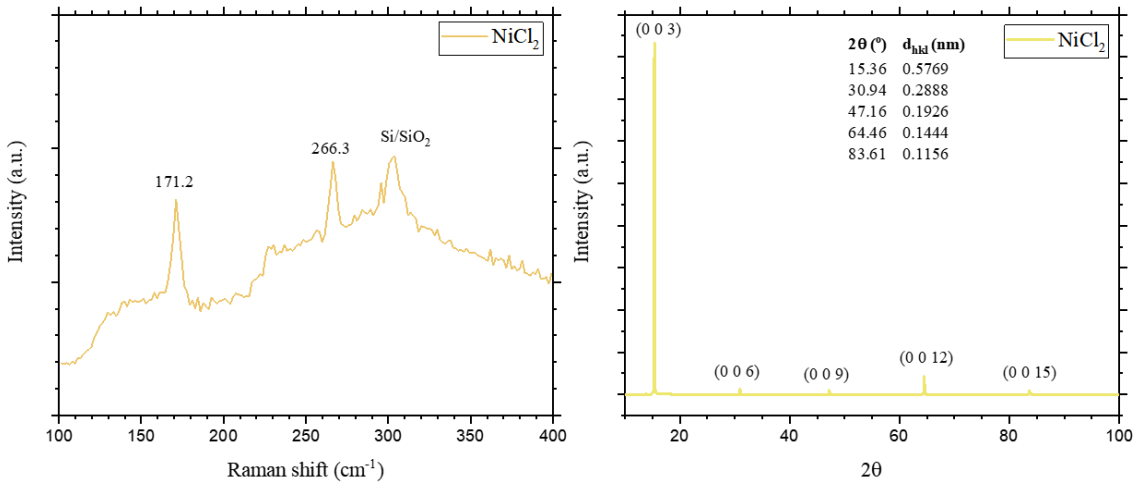

Fig. 29 | Raman spectrum (left), and XRD pattern (right) for $NiCl_2$ crystal. Note the inset includes interplanar spacing for relevant peaks that ae observed in the XRD spectrum.

Based on the magnetization versus magnetic field data in Fig. 30, $NiCl_2$ displays linear relationship up to a field H = 2 T, characteristic of paramagnetic materials. This is not to say, however, that this material is paramagnetic at 2 K, but it does indicate that higher fields would be required to saturate the magnetization yielding a hysteresis-type curve. The AFM nature of this compound is clear in the susceptibility versus temperature plot with a Neel transition temperature at 52 K. The parallel orientation reaches higher susceptibility at a field of 500 Oe compared to the perpendicular orientation indicating that the easy-axis for this compound is also in the ab plane. Note the inverse susceptibility plot displaying large noise with increasing temperature. This is due to the low field at which the measurement is taken (500 Oe) at which the magnetic moment detected from the small crystalline sample is small compared to the diamagnetic response detected from the sample holder. To improve this analysis and reduce the noise, future measurements should be taken at higher magnetic fields.

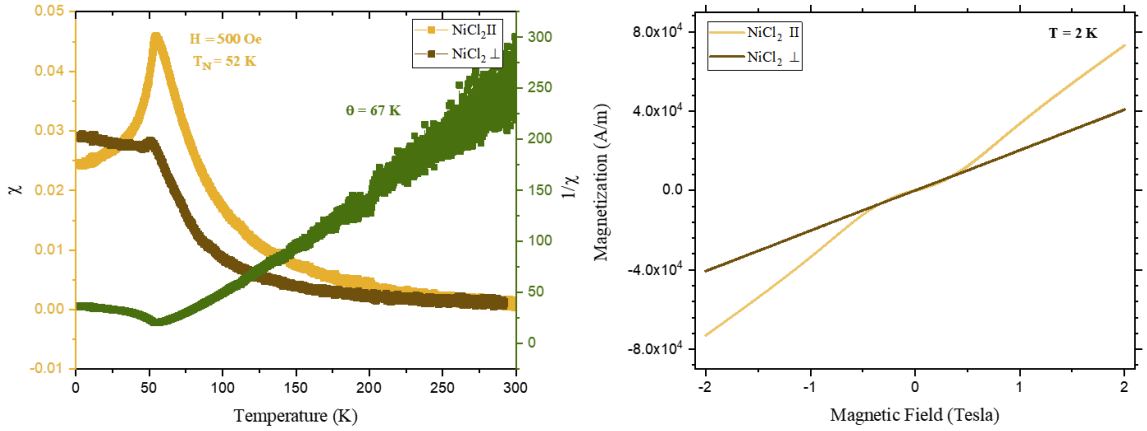

Fig. 30 | Magnetic susceptibility and inverse susceptibility of $NiCl_2$ in parallel and perpendicular orientation to the ab plane of the crystal (left). Note the noise in the $1/\chi$ plot at high temperatures comes from the lower crystal to background signal. Magnetization curve with magnetic field showing linear relationship up to 2 T.

4.2.4 $CoCl_2$

Cobalt di-chloride is quite similar to nickel di-chloride in terms of structure and properties. This compound also exhibits AFM stacking at temperatures below 25 K, while within a single layer, it adopts ferromagnetic order (see Fig. 23). Structurally, it exists in the rhombohedral $CdCl_2$ structure with space group $R\bar{3}m$ as illustrated in Fig. 17. A temperature dependent structural phase transition has not been reported for this compound.

The synthesis for this compound was performed in a sealed quartz ampoule environment similar to the method described before (see Fig. 31 and Table 1 for details). A total mass of 0.5 grams of precursors was loaded inside of an ampoule consisting of cobalt powder (of 2 μm particle size, 99.8% trace metals basis purity from Sigma Aldrich) together with powder of tellurium tetrachloride (crystalline $TeCl_4$ from Alfa Aesar 99.9% metals basis purity) as a transport agent and chlorine source. To preserve the purity of the moisture sensitive $TeCl_4$, precursors were loaded inside of a glovebox

avoiding exposure to air. The growth conditions yielded small $CoCl_2$ crystal size (mm range) in the sink area. The source area in the ampoule had a small amount of precursor powders remaining that did not completely transport in the given growth period. Note that the purple color in the source region indicates formation of the hydrate form of $CoCl_2$ meaning that some water was able to remain inside the ampoule. The presence of water can interfere with the crystal growth so to avoid this, in future synthesis of this compound, both the metal powder and transfer agent should be desorbed of any moisture by heating them to temperatures that will enable their respective removal of water.

This compound also has extremely low Raman signal and is quite robust to the high-power laser used for characterization. Despite this, peaks at 151, and 248 cm^{-1} are detected which is in line with reported values from literature (Lockwood, Johnstone, Carrara, & Mischler, 1978). Note that the additional peak observed at and 302 cm^{-1} is associated with the Si/SiO_2 substrate. Elemental composition showing the presence of cobalt and chlorine in the compound was characterized via EDS and the data is included in the Supplementary Information chapter at the end of this document. As mentioned before, the detection of chlorine atoms is lower than the expected concentration due to the limitations of the instrument when detecting smaller atoms. Structural characterization via XRD is not attained for this crystal due to the inability to isolate single crystals that are large enough for the characterization to yield good results, thus, it is excluded from this document. Magnetic properties are also excluded from this work due to limitations of crystal size, however, there is reported properties in literature that suggest that this compound also is AFM at temperatures lower than 25 K (McGuire, 2017).

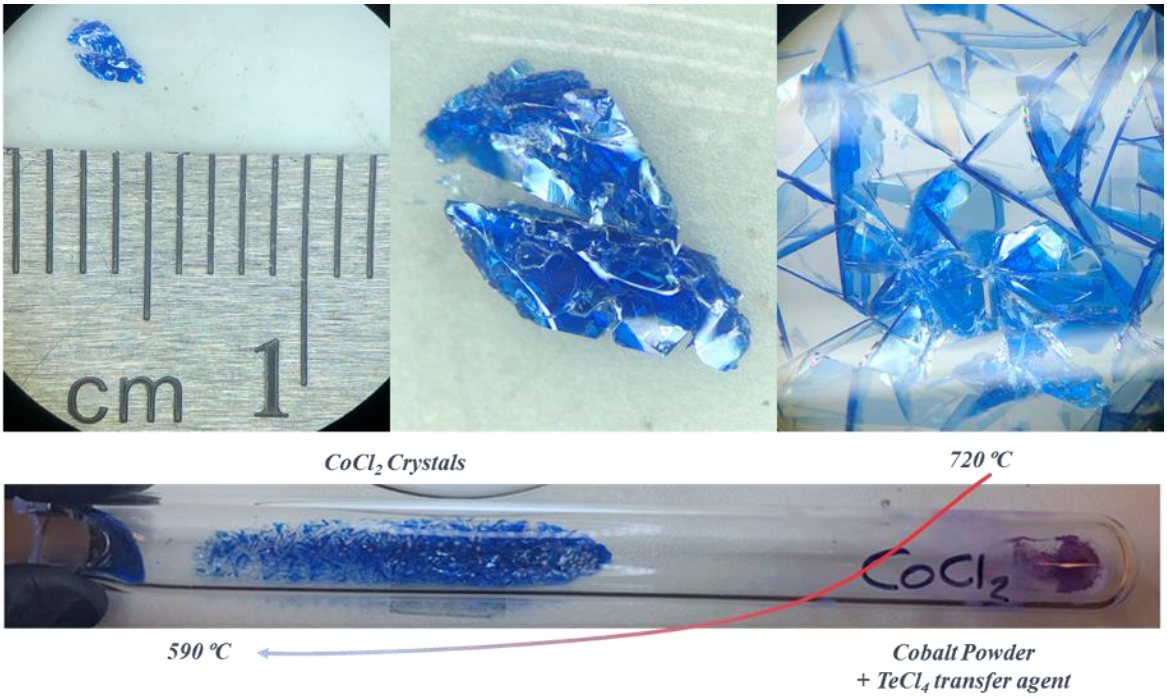

Fig. 31 | Images of the $CoCl_2$ crystals including growth conditions (bottom).

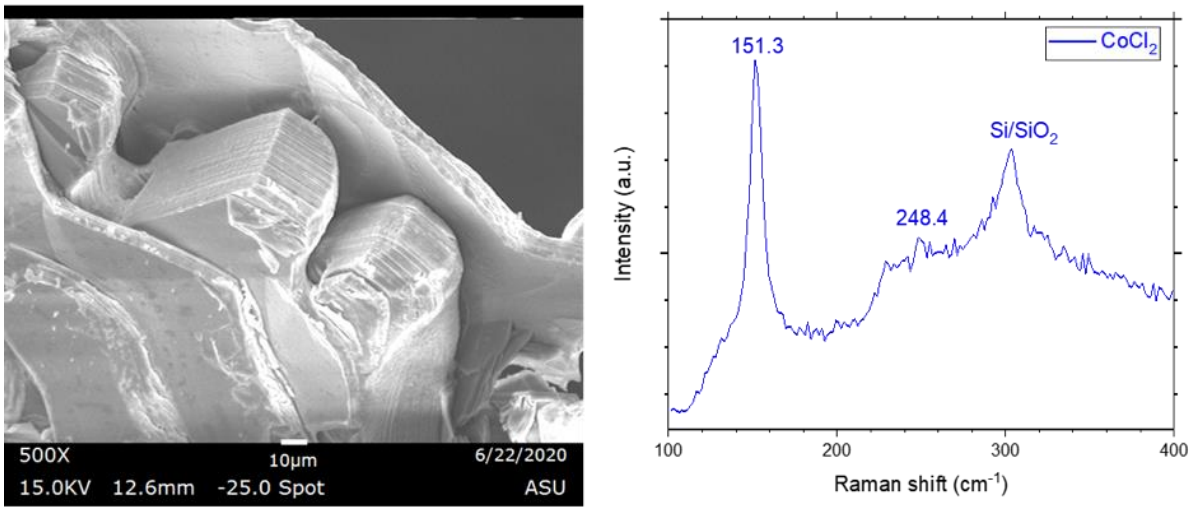

Fig. 32 | (Left) SEM image of $CoCo_2$ flake; note the stacking of layers near the edges of the imaged flakes. Raman signal showing peaks at 151 and 248 cm^{-1} (right).

4.2.5 $FeCl_3$

As one of the lower temperature TMH compound, $FeCl_3$ has been studied for a long time and it has been found to exist in many phases including the rhombohedral BiI_3 crystal structure ($R\bar{3}$ space group), trigonal Ti_3O structure (P312 space group), and the trigonal $P\bar{3}$ structure. This compound is highly hygroscopic making it difficult to handle and challenging to characterize. As such, the crystal was synthesized in the closed (sealed ampoule) system environment described before. Taking advantage of the compounds high vapor pressure, synthesis was performed using 300mg of anhydrous $FeCl_3$ powder (98% purity from Alfa Aesar). To avoid contact with air, precursors were transferred in the glovebox prior to sealing. Growth took place in a two-zone furnace as per the conditions listed in Table 1. Most precursors were transported to the cold zone with a small amount powder remaining in the source area likely from oxidized iron judging by the (brown) color. All crystals grew in one (coldest) location inside the ampoule with large hexagonal domains in the millimeter range (see Fig. 33).

The stability of these crystals is very low upon exposure to air. Fig. XX shows the immediate degradation that occurs within minutes of breaking the vacuum environment where $FeCl_3$ is stored. Crystal degradation begins on the edges (likely due to the presence of more active sites compared to the bulk) and continues until all crystals have turned into a (brown) liquid. As a result of this challenge, crystals were isolated inside the glovebox, exfoliated onto Si/SiO_2 substrates and covered with polymethyl methacrylate (PMMA). This method prolongs the stability of $FeCl_3$ allowing for Raman measurements to be taken. However, further characterization was made impossible given the available instruments.

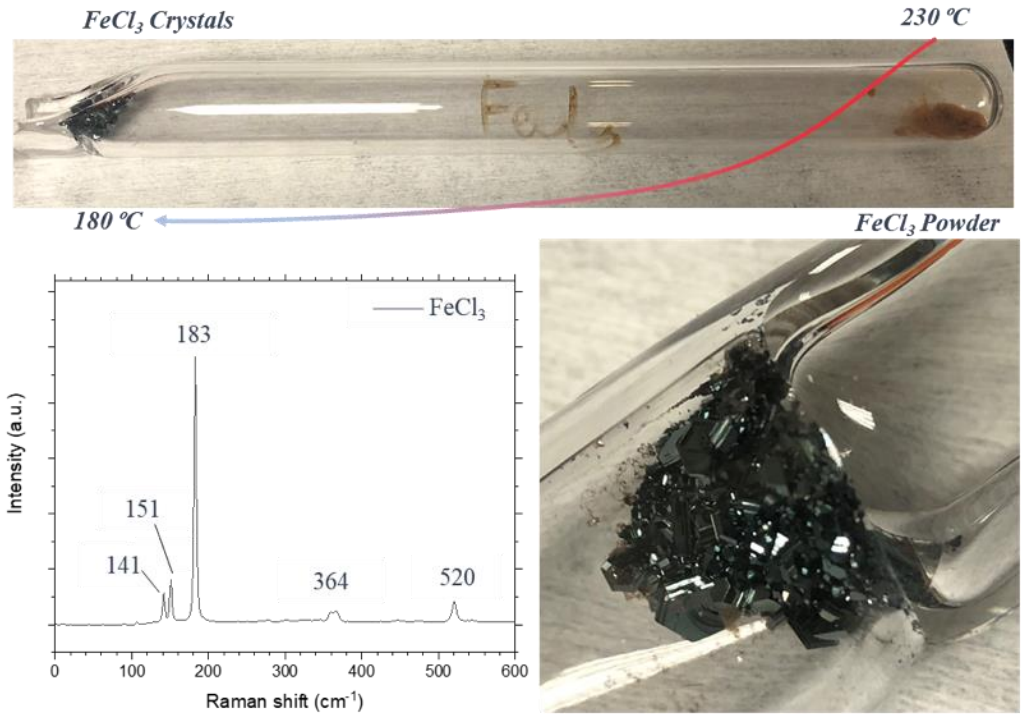

Fig. 33 | Growth ampoule of with $FeCl_3$ crystals in the cold zone and leftover precursors in the hot zone (top), closeup image of the crystals (bottom right), and Raman spectrum (bottom left) confirming the identity of the crystal.

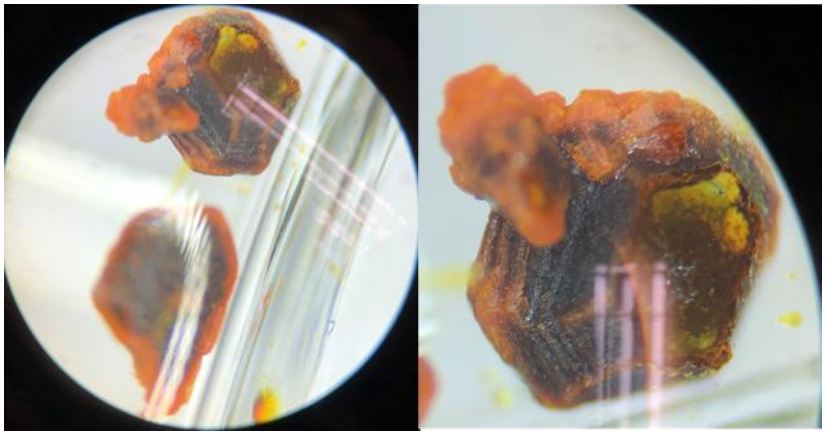

Fig. 34 | Fast degradation of $FeCl_3$ crystals starting with the edges. Note the crystals were images while being inside of a glass vial with a closed lid, upon opening the lid, crystal degradation is accelerated, and they become liquid.

4.3 Synthesis and characterization of cationic, ternary TMH alloys

Successful and controllable alloying across the cations in the MCl_x (x = 2 or 3) compounds must fulfill certain requirements that can be classified into two parts: chemical and physical considerations. The former includes the factors that ultimately affect the Gibbs free energy of the compound. Among those factors is the crystal structure which can induce strain in the crystal lattice if it doesn't match between parent compounds, difference in atomic radius which can similarly lead to strain and change in bond length, electronegativity which affects the bond length/strength between two atoms, and valence which clearly affects the number of bonds an atom will more preferentially form. Generally, alloying of two compounds (or elements) becomes thermodynamically stable when there is a match between crystal structure, electronegativity, atomic radius, and valence in which case the formation enthalpy of the alloy is lowered to a point where it allows the contribution from the increased mixing entropy to make the Gibbs energy negative.

The second class, physical considerations, includes design of the experiment to provide appropriate conditions of temperature and pressure conducive for growth, choice and stoichiometry of precursors, precursor form (e.g. powder size) which determines the surface area available to react, choice of transport agent which will determine the mechanism of transport, and vapor pressure of all compounds in the given temperature conditions. Phase diagrams are a useful resource that help determine the temperature and concentrations under which certain elements or compounds can be alloyed (or become phase separated). However, phase diagrams for the alloys presented in this work were not found, except in the case of the $Co_{1-x}Ni_xCl_2$ alloy, which suggested that the two parent

compounds ($NiCl_2$) and ($CoCl_2$) are immiscible with each other at all compositional ratios (see Supplementary Information). Despite this information, the alloy does form, as will be described in the following sections.

4.3.1 $Mo_{(1-x)}Cr_xCl_3$ alloy

Chromium sits in the fourth period in the periodic table. Its outer electronic shell consists of 4 electrons in the d-orbital and, in the $CrCl_3$ compound, it exists in the +3-oxidation state. Molybdenum sits in the same group (6) of the transition metals section in the periodic table. It has the same number of d-orbital electrons, differing from chromium by means of a larger atomic radius and, albeit counterintuitively, larger electronegativity. Despite the small differences between chromium and molybdenum, however, their tri-chloride compounds have the same monoclinic crystal structure (C2/m space group) with small differences in their lattice constants. Motivated by the magnetism in $CrCl_3$ at low temperatures, and in $MoCl_3$ at high temperatures, their alloy is synthesized at two composition ratios as will be described below.

Synthesis of all alloys is performed under vacuum sealed ampoule environment starting with elemental precursors (1-5 μm molybdenum powder from Sigma Aldrich of 99.9% trace metals purity, 60-mesh or 250 μm chromium powder from Alfa Aesar of 99.99% metals basis purity, and $TeCl_4$ powder of 99.9% metals basis purity from Alfa Aesar). The mass of precursors was determined so as to achieve stoichiometric alloy compositions assuming all the precursors react to completion (see equation 8). The total mass in the ampoule was kept at 0.5 grams. Growth was performed in a similar fashion as

described before, in a two-zone horizontal tube furnace. For details on growth conditions for the different alloy compositions, refer to Table 3 below.

$$(1-x)Mo + xCr + \frac{3}{4}TeCl_4 \rightarrow Mo_{(1-x)}Cr_xCl_3 + \frac{3}{4}Te \qquad (8)$$

The reason for choosing elemental metal precursors is due to a different growth mechanism that takes place compared to using TMH compound. In the latter case, TMH compounds sublime in the growth region to produce TMH compound vapors (e.g. $CrCl_3$ vapor) and they decompose into metal and chlorine vapor only at very high T (as can be seen in Fig. 35). In the TMH vapor form, these compounds can self-transport by means of sublimation leading to their condensation in the cold region of the ampoule (endothermic reaction). As such, it would be challenging to find a temperature profile where both compounds have a similar vapor pressure without decomposing. That is, $CrCl_3$ and $MoCl_3$ do not have the same stability in the growth conditions of their alloy, with the latter decomposing at only 410 °C. So, in a hot zone region where temperature is 700 °C, $CrCl_3$ and $MoCl_3$ would transport via two different mechanisms lending it difficult to grow their alloy in a predictable fashion.

On the other hand, transport of elemental metal powders takes place via a different mechanism. The vapor pressure of the elements (metals) is in this case much less significant (see Fig. 35) while the driving force for transport is the chemical reaction between the transport agent and the elemental powders. In this case, the transport agent ($TeCl_4$) decomposes at the hot zone temperature and it convert into gaseous species of $TeCl_{4(g)}$, $TeCl_{2(g)}$, $Te_{2(g)}$, $Te_{(g)}$, $Cl_{2(g)}$, and $Cl_{(g)}$ (Binnewies et. al., 2012). Chromium and molybdenum powders react with the vapor species of the decomposed transport agent forming gaseous complexes that transport the metals to the cold zone (in an endothermic

type reaction) where they deposit to form the most thermodynamically stable compound in that temperature environment. The partial pressure of all these species is dependent on the temperature. The most stable gaseous complexes that would form between these species and the metal powders will dominate the transport. Much more in-depth analysis would be required to determine the complexes that actually form in this scenario, which is beyond the scope of this work.

In regard to this proposed reaction mechanism, it can easily be determined that vapor pressure of metals at the given temperature is not an important contributor to transport. From the vapor pressure curves, it can be seen that the partial pressure of chromium is much higher than that of molybdenum at all temperatures (as well as the growth temperature for this alloy). In the case that vapor pressure plays a main role in the transport, chromium would transport faster than molybdenum leading to uncontrollable stoichiometry of the product. Also, chromium and molybdenum have vapor pressures of around 10^{-10} Torr and 10^{-25} Torr, respectively (from extrapolation of the curves in Fig. 35) which is extremely low pressures to yield transport of all precursors in any reasonable amount of time.

In the other case, regarding the reaction rate during transport, a few parameters play a role; The particle size / surface area of powders will determine the reaction rate and formation of the gaseous species for transport. Chromium powder with particle size of 250 μm has much smaller surface area than molybdenum powder with size 1-5 μm which would lead to higher transport rates of molybdenum. Also, the reactivity of the transport agent with the different metals will be different due to the difference in their respective bond formation energies. The latter is mainly dependent on the electronegativity of the

metal elements (Cr = 1.66, Mo = 2.16), and atomic radius (Cr = 166 pm, Mo = 190 pm). Molybdenum being more electronegative would attract electrons in the Mo-Cl bond more closely, however, this effect would be counterbalanced by the larger radius which would lengthen their bond. Overall, the lattice constants in both of these compounds are very similar. So, in general, the surface area of the powders would likely contribute more to the overall reaction rates leading to fast and complete transport of both species preserving the stoichiometry of the alloy.

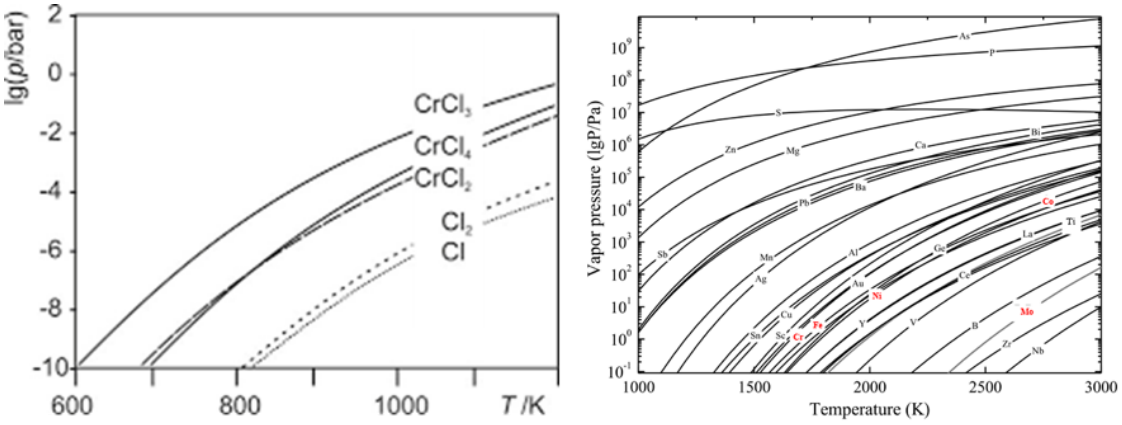

Fig. 35 | Vapor pressure of $CrCl_3$ and other decomposed species (left). Vapor pressure of metals with the relevant ones highlighted in red (right).

Table 3. Summary of crystal growth conditions of $Mo_{1-x}Cr_xCl_3$ alloy compound. Stoichiometry of compounds is determined via EDS analysis. Note that chlorine concentration is underestimated due to limitations of the instrument.

Compound (EDX analysis)	**Synthesis method**	**Hot zone T (ºC)**	**Cold zone T (ºC)**	**Precursors**	**Growth time (hrs)**
$Mo_{0.52}Cr_{0.48}Cl_{2.65}$	CVT	700	570	Mo, Cr, $TeCl_4$	72
$Mo_{0.77}Cr_{0.23}Cl_{2.64}$	CVT	625	560	Mo, Cr, $TeCl_4$	72

Images of the parent compounds and alloys show a clear trend of change in color with alloying composition (see Fig. 36) which is an indication of a bandgap change. Absorption measurements were not performed in this work, although they would be useful to determine the optical bandgap engineering with alloy concentration.

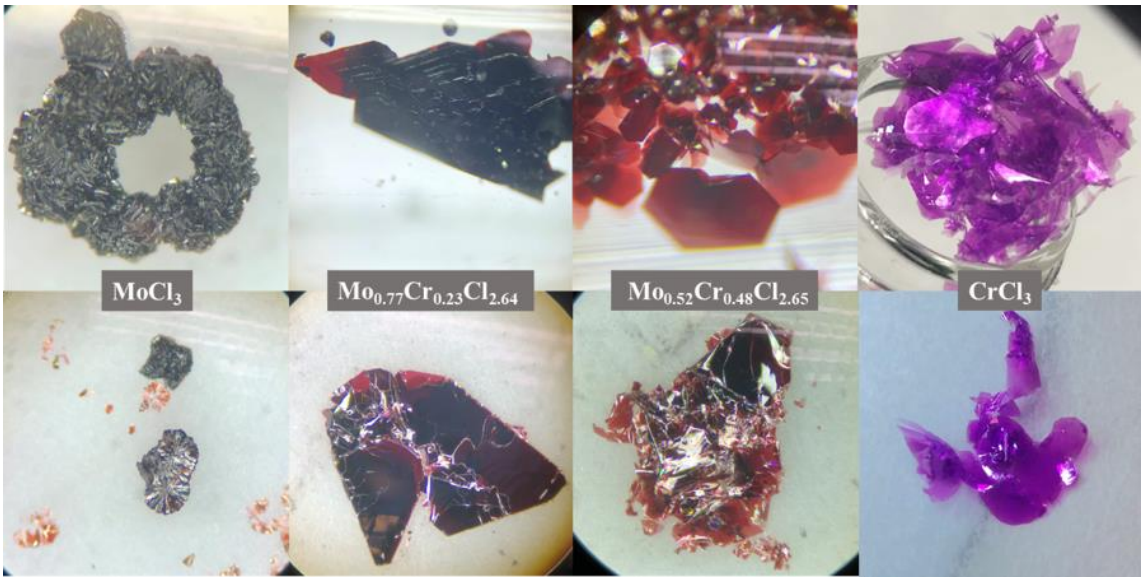

Fig. 36 | Macroscopic images of parent compounds and their alloys.

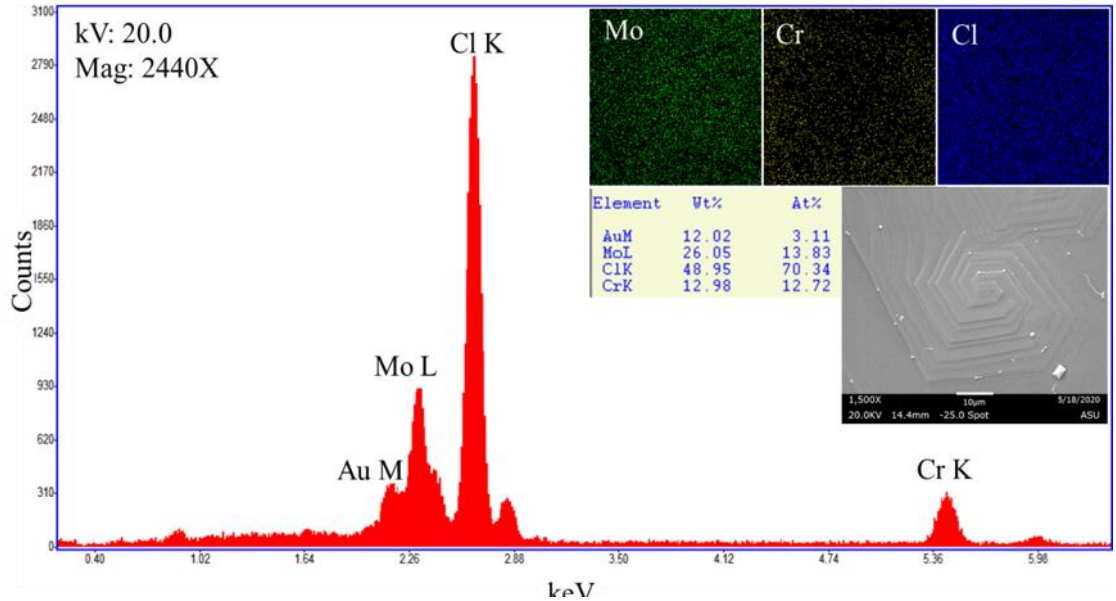

Fig. 37 | EDS mapping and spectrum illustrating the stoichiometric and uniform $Mo_{0.52}Cr_{0.48}Cl_{2.65}$ alloy. Note, the Au peak is present due to the conductive gold coating applied on top of the samples to reduce charging effects.

Energy dispersive spectroscopy reveals no sign of an alloy phase separation. The mapping in Fig. 37 clearly shows uniform coverage of molybdenum, chromium, and chlorine within the measured area (measurements are repeated in different regions of the crystal but are not included here due to the results being very similar).

Due to the similarity in crystal structure, the Raman signal of these alloys is expected to emerge from the signal of the two parent compounds and shift from one Raman spectrum to the other with varying alloy composition. $CrCl_3$ displays active Raman modes at 163, 206, 245, 299, and 343 cm^{-1}, while $MoCl_3$ is shows active modes at 156, 237, 261, 296, and 351 cm^{-1} (McGuire, Yan, et al., 2017). From Fig. 38, it is clear that alloying across from one compound to the other does not specifically induce the predicted shifts in Raman modes based on the spring force model. However, going from the Raman spectrum of $CrCl_3$ and introducing molybdenum in the lattice yields the emergence of new Raman peaks. That is, there is a shift from 343 to 349 cm^{-1} and a double peak is observed around 300 cm^{-1}. Nevertheless, it is difficult to claim that these compounds are uniformly alloyed solely based on the Raman signal. The emergence of a double peak and lack of predictable shift in most peaks suggests that some other, perhaps more complex, phenomenon is taking place. It could be that there is some microscopic phase separation within the alloy, or that the incorporation of molybdenum atoms induces a phase transition in $CrCl_3$. Further characterization can be done to answer this question. The other thing to note is the broad peaks that are observed in the $Mo_{0.75}Cr_{0.25}Cl_3$ alloy which are an indication that the laser is probing the phonon density of states of the material due to the high defect density within the crystal. This makes in more challenging to determine a trend in Raman shift as a function of alloy stoichiometry.

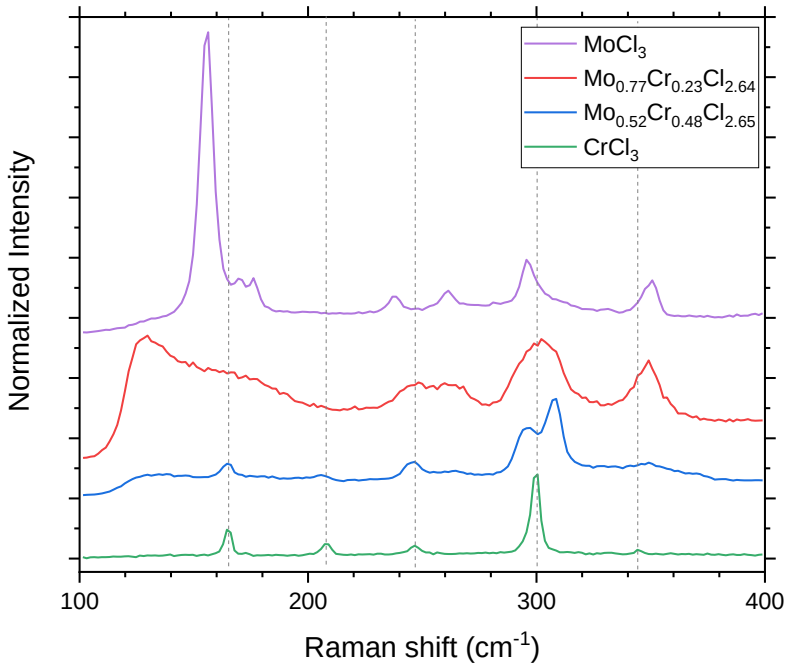

Fig. 38 | Raman spectra of parent compounds and their alloys. Gray dotted lines are used as guides to visualize peak shifts in reference to $CrCl_3$.

Table 4. Raman peak values for parent compounds and alloys. Note that some of the values are omitted due to the peaks being very broad and difficult to identify.

Compound	**Raman shift (cm^{-1})**				
$CrCl_3$	163	206	245	300	343
$Mo_{0.52}Cr_{0.48}Cl_{2.65}$	165	206	247	297, 308	349
$Mo_{0.77}Cr_{0.23}Cl_{2.64}$	n/a	n/a	n/a	302	349
$MoCl_3$	156	237	261	296	351

Structural analysis with XRD indicates that the ternary compounds are not completely phase separated, that is, there is a peak shift to lower reflection angles in all {0 0 1} planes with increasing molybdenum concentration in the alloy. This means that the incorporation of molybdenum increases the interplanar spacing, as is expected as a result of the larger atomic radius compared to the host transition metal (chromium). The measurement, however, does showcase the emergence of an additional reflection peak near the $MoCl_3$ signal which is present in both alloy compounds and does not seem to

shift with changing alloy concentration. This could mean that certain regions within the alloy contain phase separated $MoCl_3$; complete phase separation would generate peaks in the regions of both parent compounds and would reveal no peak shift (as is observed in Fig. 39). So, it can be said that an alloy of $Mo_{1-x}Cr_xCl_2$ is indeed formed, although partial phase separation may also be present.

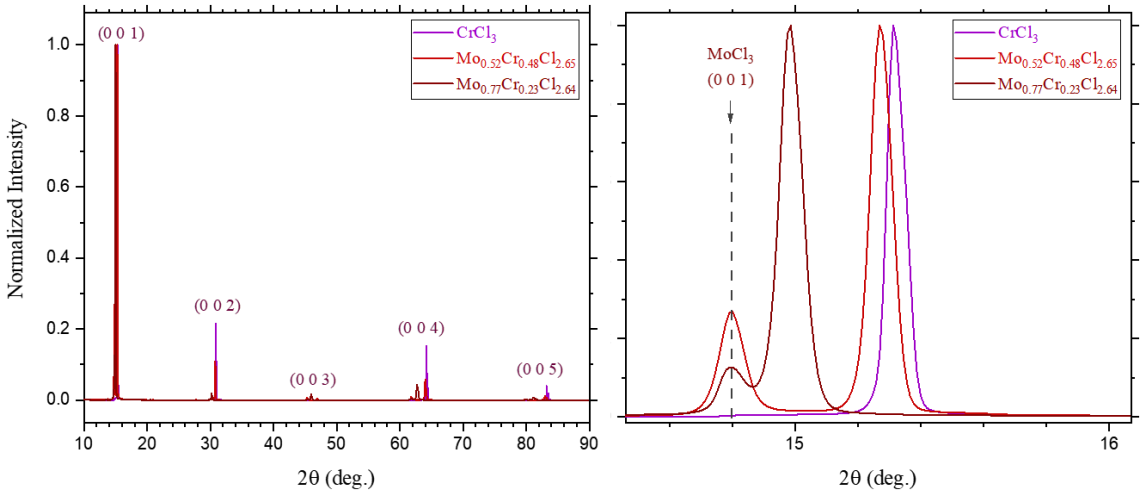

Fig. 39 | X-ray diffraction pattern of $CrCl_3$ and two cation (Mo) alloys. On the right is a closeup of the (0 0 1) reflection indicating the shift in XRD peaks with alloy composition. The dashed line indicates the position for the $MoCl_3$ (0 0 1) reflection.

Table 5. Summary of XRD peaks for the parent compound $CrCl_3$ and Mo-alloys.

Compound	**d (0 0 1) (nm)**	**d (0 0 2) (nm)**	**d (0 0 3) (nm)**	**d (0 0 4) (nm)**	**d (0 0 5) (nm)**
$CrCl_3$	0.5787	0.2896	0.1932	0.1449	0.1160
$Mo_{0.52}Cr_{0.48}Cl_{2.65}$	0.5803	0.2904	0.1937	0.1453	0.1163
$Mo_{0.77}Cr_{0.23}Cl_{2.64}$	0.5912	0.2958	0.1973	0.1480	0.1184
α-$MoCl_3$ (expected)	0.599	n/a	n/a	n/a	n/a

As a result of dimerization between the molybdenum atoms in $MoCl_3$, magnetic order is unsustainable at low temperatures as is discussed in more detail earlier in this chapter. It is, thus, expected to see a breakdown of antiferromagnetism in $CrCl_3$ at some concentration of molybdenum within its crystal lattice. This is indeed observed in the

susceptibility plots that showcase a lower Néel transition temperature and Weiss constant with increasing molybdenum. The transition is accompanied by, what appears to be, an AFM to FM transformation shown by the change in curvature at low temperaures in Fig. 40. Susceptibility in $CrCl_3$ reaches a peak with decreasing temperature which is followed by a reduction in magnitude. This is typical of AFM order where the magnetism between the opposing layers cancels out leading to reduced total magnetic moment. The subsequent susceptibility plots contain a change in the susceptibility slope (with an inflection point around the Curie temperature) but it follows a continuously increasing trend as is commonly seen in FM materials.

The alloy with 75% molybdenum appears mainly paramagnetic with a slight curvature change in the perpendicular orientation indicating paramagnetic to FM transition somewhere near the low limit of the temperature range. However, there are two indications that the alloy high in molybdenum is not completely paramagnetic: (1) the inverse susceptibility plot is not completely linear and does not intersect at zero temperature, (2) there is a FM-like magnetization versus magnetic field curve and this hysteresis has no linear region. This finding is rather interesting and further studies will reveal the true nature of the FM in this alloy system.

Another important feature from Fig. 43 is the switch in the easy axis which occurs somewhere between 50% - 75% molybdenum concentration. Note the susceptibility and magnetization in the perpendicular orientation reach higher values compared to parallel, with the latter being the easy-axis in the host $CrCl_3$ lattice as well as the alloy up to 50% molybdenum. A lot remains to be explored in this alloy system, especially the magnetic character at temperatures higher than room temperature.

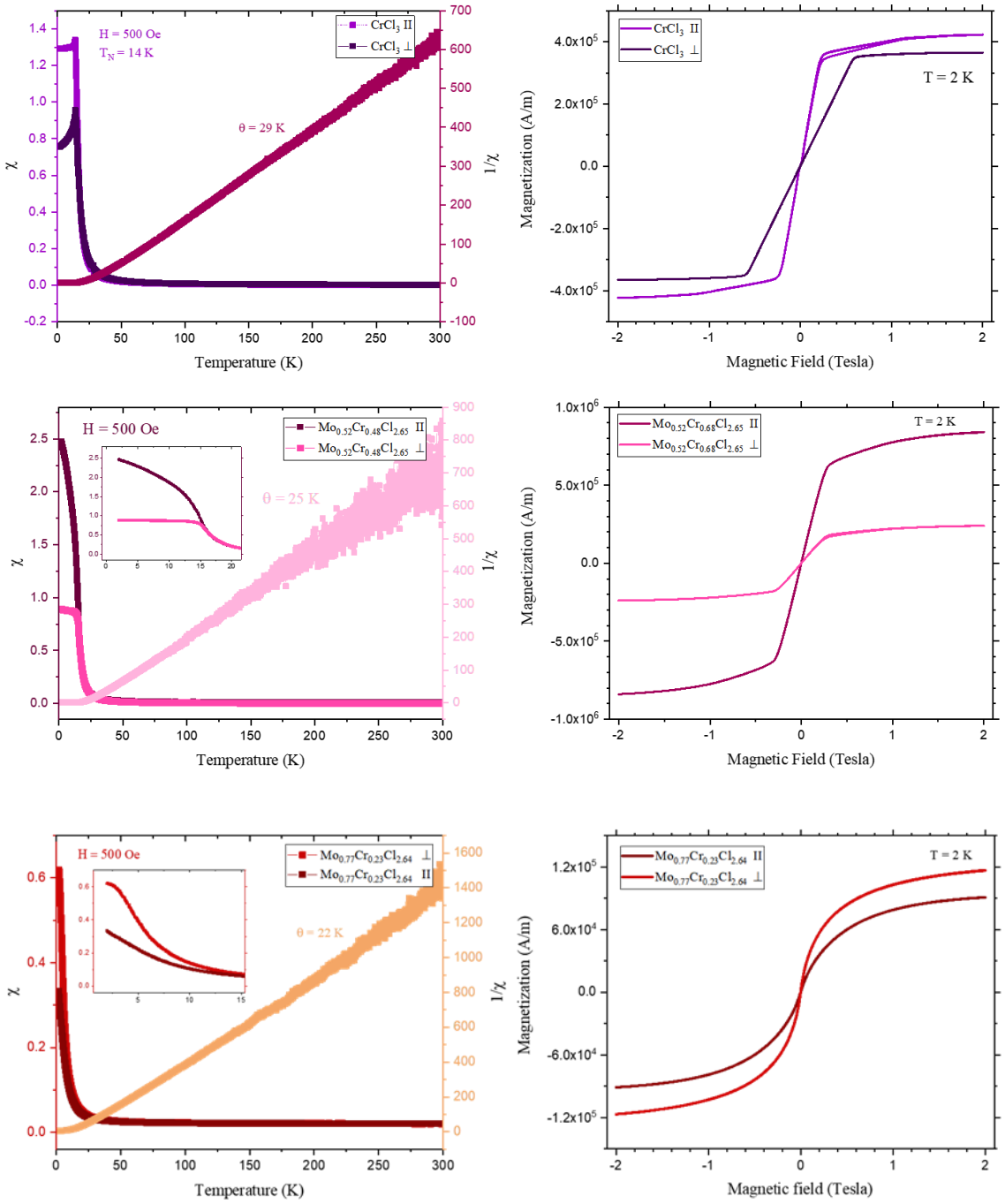

Fig. 40 | VSM data for $CrCl_3$ and two alloys with molybdenum. Plots on the left show susceptibility in both II and ⊥ orientations as well as inverse susceptibility on the right y-axis. On the right, magnetization is plotted as a function of field for both sample orientations.

4.3.2 $Co_{(1-x)}Ni_xCl_2$ alloy

Unlike the previous alloy, cobalt and nickel sit on the same period of the periodic table with the former having 7 electrons in the 3d orbital and the latter having 8. It is thus expected that the difference between these two transition metals comes in from their electronic structure rather than their atomic radius and electronegativity. As such, they will have a different number of free electrons in their +2-valence state within the MCl_2 structure yielding different mechanisms for their magnetic order (orbital magnetic moments dominating in $CoCl_2$, and spin moments dominating in $NiCl_2$) (McGuire, 2017). Overall, AFM magnetic order is established in both compounds at low temperatures with different Néel transition temperatures (Ni = 52 K, Co = 25 K). Both parent compounds stabilize in the same crystal structure (rhombohedral $CdCl_2$ structure with space group $R\bar{3}m$) meaning that their alloy should also be expected to exist in that structure with small amount of strain due to the difference in their respective atomic radius (Ni = 149 pm, Co = 152 pm).

Synthesis of alloys of cobalt and nickel di-chloride is also performed using CVT from elemental precursors (cobalt powder of 2 μm particle size, 99.8% trace metals basis purity from Sigma Aldrich, and nickel powder of <150 μm particle size, 99.99% trace metals purity from Sigma Aldrich) and transport agent ($TeCl_4$ powder of 99.9% metals basis purity from Alfa Aesar). A total mass of 0.5 grams was loaded into the ampoule with stoichiometric precursors according to equation (9). Growth was performed in a

similar fashion as described before, in a two-zone CVT furnace. For details on growth conditions for the different alloy compositions, refer to Table 6 below.

$$(1-x)Co + xNi + \frac{1}{2}TeCl_4 \rightarrow Co_{(1-x)}Ni_xCl_2 + \frac{1}{2}Te \quad (9)$$

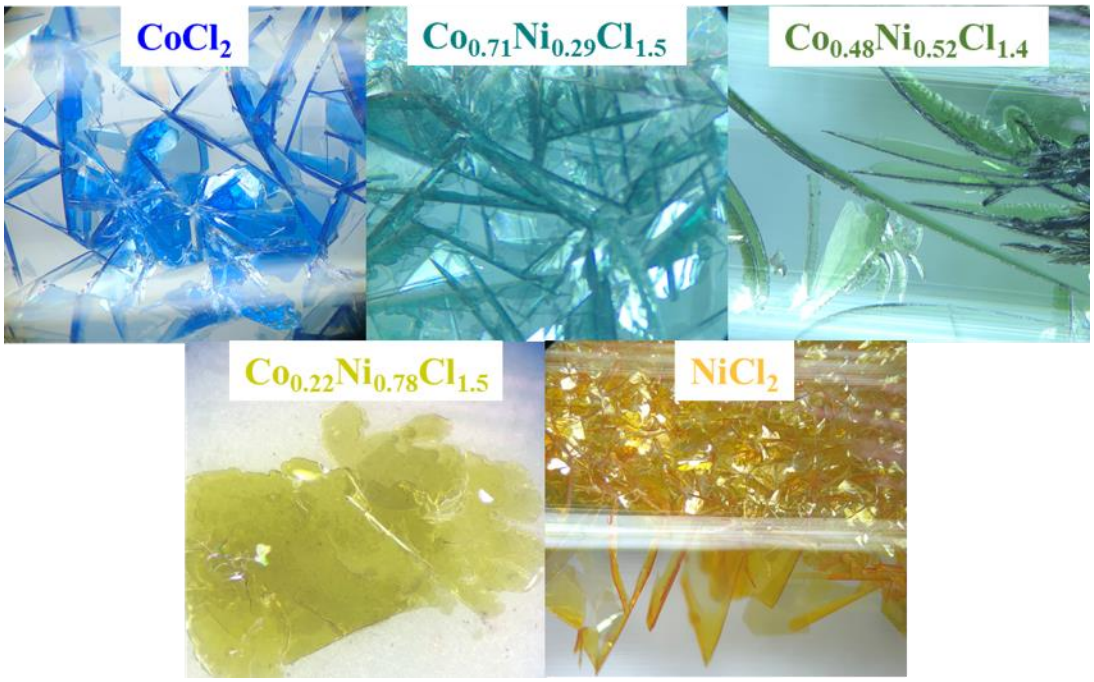

Fig. 41 | Macroscopic images of parent compounds and their alloys $Co_{(1-x)}Ni_{(x)}Cl_2$.

Growth mechanism is expected to proceed via the same pathway as with the previous alloy compounds. That is, transport of the metal powder by means of reaction with decomposed gaseous species of the transport agent ($TeCl_{4(g)}$, $TeCl_{2(g)}$, $Te_{2(g)}$, $Te_{(g)}$, $Cl_{2(g)}$, and $Cl_{(g)}$). From extrapolation of the curves in Fig. 35, it is clear that the vapor pressures of both metals (Co, and Ni vapor pressure ~ 10^{-12} Torr) are similar, albeit very small for dominating the transport reaction. Similarly, reaction of the metal powders with the transport agent species is proposed to be the leading mechanism in this synthesis. Considering that the cations are of similar atomic radius, electronegativity, and crystal

structure (in their respective chloride compounds), particle size of the powders should be the most significant factor determining transport rates. Given enough time for reaction, however, all species are transported to the cold zone (in an endothermic-type reaction) yielding stoichiometric alloy compounds as listed in Table 6.

Table 6. Summary of crystal growth conditions of $Co_{1-x}Ni_xCl_2$ alloy compound. Stoichiometry of compounds is determined via EDS analysis. Note that chlorine concentration is underestimated due to limitations of the instrument.

Compound (EDX analysis)	**Synthesis method**	**Hot zone T (ºC)**	**Cold zone T (ºC)**	**Precursor (powders)**	**Growth time (hrs)**
$Co_{0.22}Ni_{0.78}Cl_{1.5}$	CVT	740	620	Co, Ni, $TeCl_4$	72
$Co_{0.48}Ni_{0.52}Cl_{1.4}$	CVT	740	620	Co, Ni, $TeCl_4$	72
$Co_{0.71}Ni_{0.29}Cl_{1.5}$	CVT	730	600	Co, Ni, $TeCl_4$	72

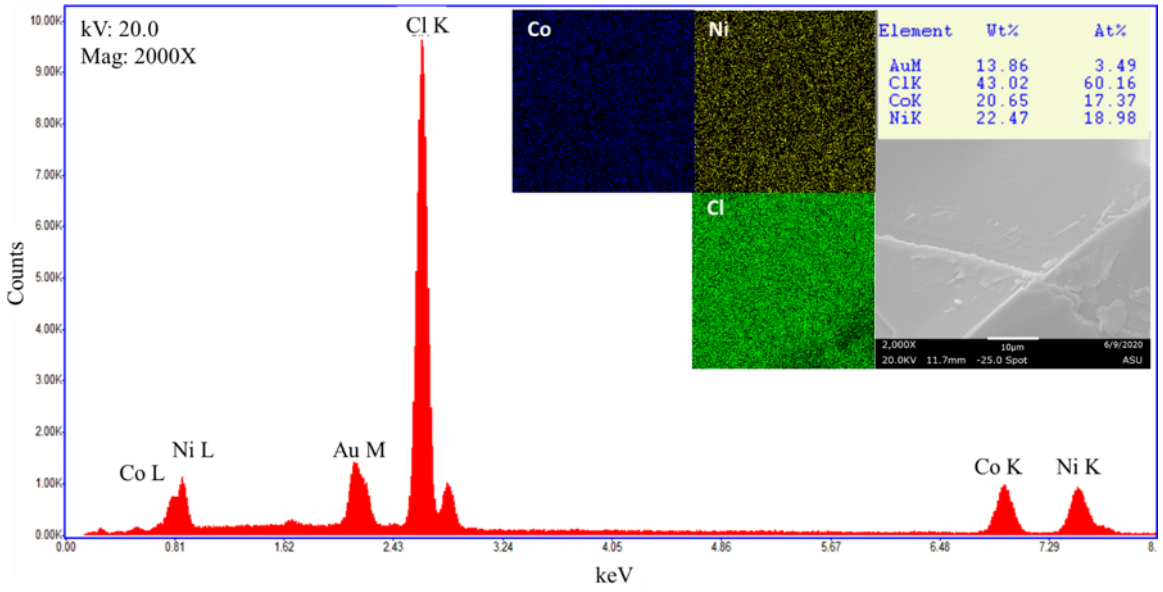

Fig. 42 | EDS mapping showcasing the uniformity of alloying $CoCl_2$ and $NiCl_2$ at a 50:50 ratio. EDS spectra of other alloy compositions will be displayed in the SI chapter.

The concentration of transition metals within this alloy system matches closely with the precursor amounts, further supporting the reasonability of the proposed growth mechanism. EDS spectra of the 50:50 alloy is shown in Fig. 46, where mapping of the elements illustrates the uniformity of the alloy.

Further analysis using Raman spectroscopy outlines a red-shift trend in the crystal lattice vibration modes as detailed in Table 7. The peak near 300 cm^{-1} is associated with a low intensity signal from the substrate (Si/SiO_2) and is, as such, not changing. The other two observable peaks near 171.2 cm^{-1} and 266.3 cm^{-1} for $NiCl_2$ are both red-shifting which can be explained by the spring force model. This model describes the lattice vibrations as motion between masses held together via a massless spring. The frequency of the vibration in such a model depends on equation 8 where υ = frequency (cm^{-1}), μ = reduced mass of the atom, and k = spring constant.

$$\vartheta = \frac{1}{2\pi}\sqrt{\frac{k}{\mu}} \qquad (10)$$

Clearly, higher mass atoms should result in lower frequency vibrations, while higher spring constants should lead to higher vibrational frequencies. In the case of the $Co_{1-x}Ni_xCl_2$ alloy, nickel has a larger mass than cobalt by only 0.24 g/mol. On the other hand, nickel has smaller atomic radius (149 pm) compared to the 152 pm cobalt atoms leading to a stronger bond energy with chlorine. That is, nickel-chlorine exhibits a bond dissociation energy of 372.3 kJ/mol, while cobalt-chlorine requires 343.9 kJ/mol. The bond energy is proportional to the spring constant in the above-mentioned model meaning that higher energy bonds between nickel and chlorine dominate the effect of the mass leading to a smaller vibrational frequency in the $CoCl_2$ system versus $NiCl_2$ which

translates into a red-shift in the Raman signal (see Fig. 43 and Table 7). Note that the Raman intensity of this alloy system including both parent compounds is relatively low making it difficult to resolve all the peaks. That is, even at very high-power levels, these compounds absorb low amount of the laser radiation yielding low signal. As a result, some of the expected peaks (such as 190, 235 cm^{-1} for $CoCl_2$) are not easily distinguished from noise (Lockwood et al., 1978).

Table 7. Raman shift peaks at different compositions of the $Co_{1-x}Ni_xCl_2$ alloy (x = 0 to 1).

Compound	**Raman shift (cm^{-1})**	
$NiCl_2$	171.2	266.3
$Co_{0.22}Ni_{0.78}Cl_{1.5}$	166.2	263.1
$Co_{0.48}Ni_{0.52}Cl_{1.4}$	159.6	258.2
$Co_{0.71}Ni_{0.29}Cl_{1.5}$	156.3	253.3
$CoCl_2$	151.3	248.4

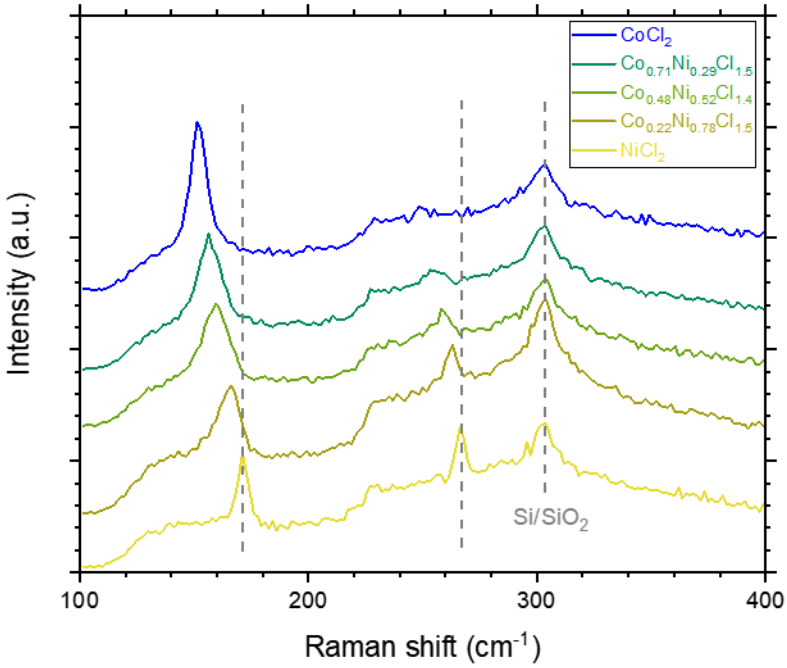

Fig. 43 | Raman signal of $Co_{1-x}Ni_xCl_2$ alloy system showcasing red-shifting with addition of cobalt in the $NiCl_2$ crystal lattice.

Table 8. Interplanar spacing for the given reflection planes. Note that the interplanar spacing for $CoCl_2$ is not experimentally determined here, rather it is adopted from literature.

Compound	d (0 0 3) (nm)	d (0 0 6) (nm)	d (0 0 9) (nm)	d (0 0 12) (nm)	d (0 0 15) (nm)
$NiCl_2$	0.5769	0.2888	0.1926	0.1444	0.1156
$Co_{0.22}Ni_{0.78}Cl_{1.5}$	0.5754	0.2884	0.1925	0.1445	0.1156
$Co_{0.48}Ni_{0.52}Cl_{1.4}$	0.5776	0.2891	0.1928	0.1447	0.1158
$Co_{0.71}Ni_{0.29}Cl_{1.5}$	0.5776	0.2892	0.1929	0.1447	0.1158
$CoCl_2$ (expected)	0.581	n/a	n/a	n/a	n/a

X-ray diffraction analysis is not performed on the $CoCl_2$ crystals due to limitations from the crystal size. A placeholder dotted line is present in the plot below showing a lower XRD peak associated with the $CoCl_2$ structure compared to the $NiCl_2$ structure coming from the same reflection plane (0 0 3). Considering the slightly larger atomic radius of cobalt compared to nickel, the interplanar spacing of the cobalt containing compounds is expected to increase with cobalt concentration leading to a smaller 2θ value. This trend is generally observed within this alloy system, however, there is a small deviation from it. $Co_{0.22}Ni_{0.78}Cl_{1.5}$ has a higher reflecting angle near the (0 0 3) reflection compared to $NiCl_2$ while at higher angles (as illustrated in Fig. 45), this compound is also shifting to lower angles as expected. This observation cannot be easily explained without further analysis of the crystal structure dependence on cation concentration. That is, it is likely that small amount of cobalt incorporation into the $NiCl_2$ lattice induces a phase change leading to the unexpected higher (0 0 3) peak, while higher concentrations of cobalt stabilize the inherent crystal structure that is found in both parent compounds (namely, the rhombohedral $CdCl_2$ structure with space group $R\bar{3}m$). More in-depth analysis will reveal the nature of this inconsistency in the XRD pattern for this alloy system. Note that the double peak in Fig. 45 is a commonly found artifact

associated with the nature of the copper excitation sources composed of two energy waves (Cu Kα1 and Cu Kα2) which are known to generate this type of splitting of the peaks in the XRD pattern. This is taken into account when calculating the interplanar spacing so that the appropriate λ value is used for the double-peaks.

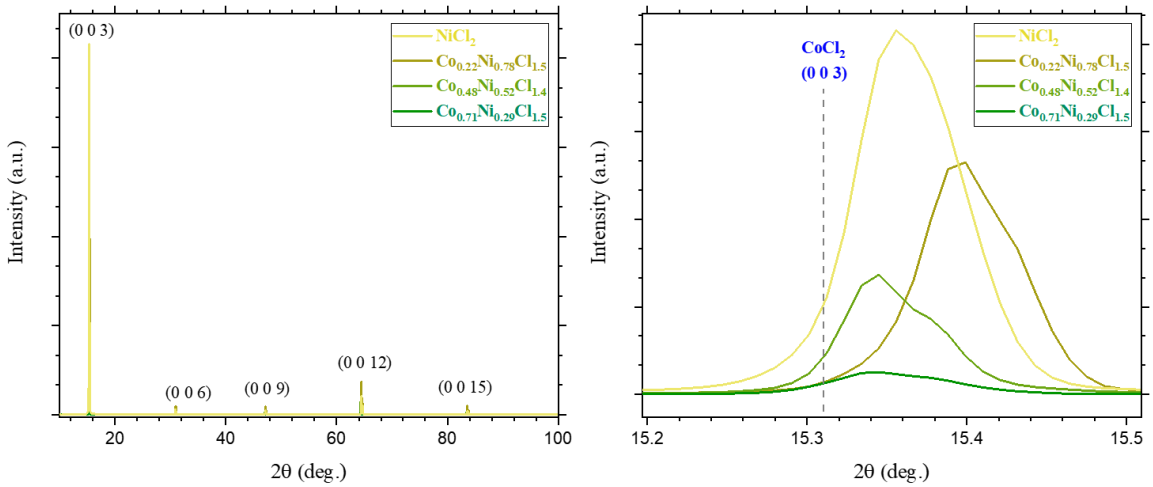

Fig. 44 | XRD analysis for $Co_{1-x}Ni_xCl_2$ alloy system showing the characteristic reflections from the {0 0 3} family of planes associated with the rhombohedral $CdCl_2$ structure with space group $R\bar{3}m$. The closeup on the right emphasizes the shift in interplanar spacing with alloy composition. Dotted line is a placeholder for the peak expected from $CoCl_2$.

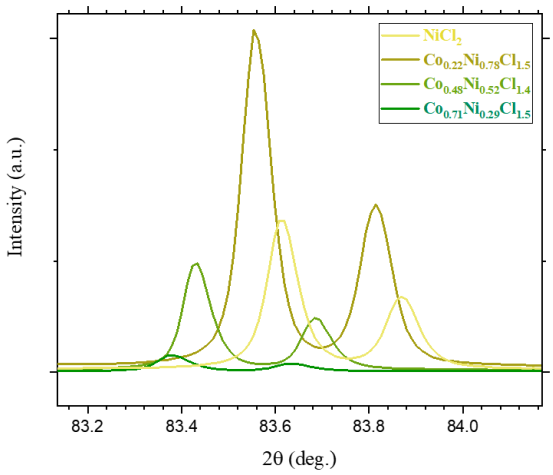

Fig. 45 | XRD analysis for $Co_{1-x}Ni_xCl_2$ alloy system showing the characteristic reflections from the {0 0 3} family of planes associated with the rhombohedral $CdCl_2$ structure with space group $R\bar{3}m$. Closeup showcasing a slight change in trend compared to the (0 0 3) reflections as is described in the text above.

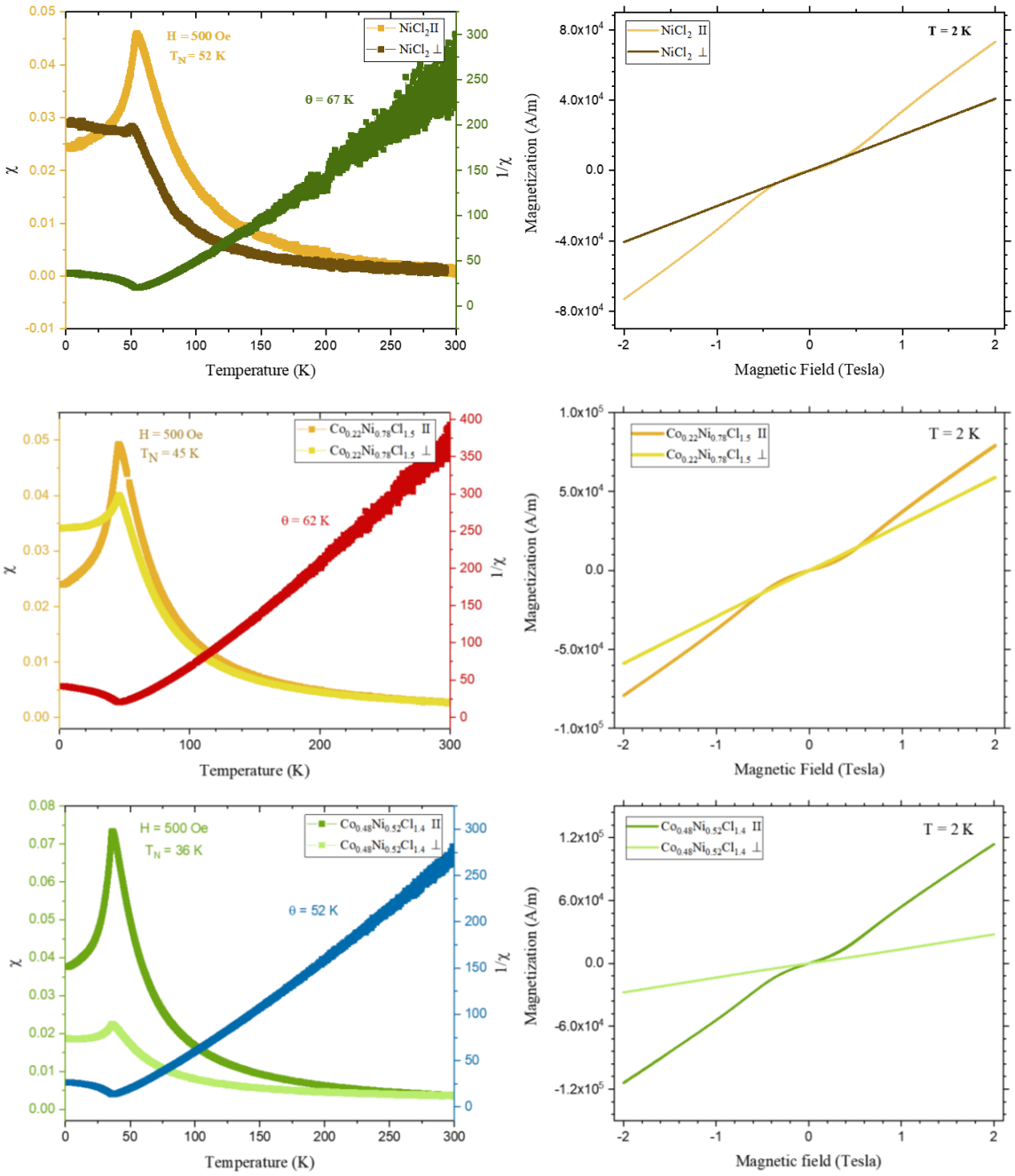

Fig. 46 | VSM data for $NiCl_2$ and two alloys with cobalt. Plots on the left show ZFC susceptibility in both II and ⊥ orientations (referencing the ab-plane) as well as inverse susceptibility on the left y-axis. On the right, magnetization is plotted as a function of field for both sample orientations.

The magnetization curves as a function of magnetic field (Fig. 46) are not displaying a hysteresis (as expected for ferro- and anti-ferromagnetic materials) but remain constant up to 2 Tesla. This does not mean that these compounds are paramagnetic (with characteristic linear magnetization versus field relationship), rather, it could mean that the field applied is not high enough to saturate the magnetic moments. Another feature in the magnetization plots is the curvature near low fields for the parallel orientation. This artifact is well reported in previous studies and is described to occur as a result of orientation of the field and the sample. In the parallel configuration, samples consisting of flakes not necessarily bound strongly to each other can be oriented slightly off in reference to the applied field leading to a not very well-defined magnetization curve which will be more pronounced at low fields. Further, in the case where moments are oriented in the ab-plane direction and the field is applied parallel to that direction, spin flopping occurs at low fields giving rise to the AFM order, as opposed to a coherent rotation of moments that is present when magnetic moment is out-of-plane. This leads to the non-linear magnetization curve at low fields in the parallel orientation which is consistently observed in all measurements and is especially evident in the $Co_{(1-x)}Ni_xCl_2$ data (McGuire, Clark, et al., 2017).

The evidence for AFM order between stacked layers in this alloy system is found in the susceptibility curves as a function of temperature. That is, there is a decrease of magnetic moment measured below the transition temperature. As discussed previously, $NiCl_2$ exhibits AFM order at $T < 52$ K, while $CoCl_2$ at $T < 25$ K. Susceptibility as a function of temperature displays the Néel transition temperature (from paramagnetic at high T to AFM at low T) in Fig. 46, while the inverse susceptibility displays the Weiss

temperature around 67 K. The transition temperature shifts to lower values with increasing cobalt in the crystal lattice of nickel di-chloride which is expected due to the lower Néel temperature of $CoCl_2$. With that, the Weiss constant is also decreasing with increasing cobalt, although still remaining positive. Note that the noise in the inverse susceptibility plot is a result of the low field (500 Oe) applied during the measurement and the lower sample signal to background noise with increasing temperature. The positive Weiss constant implies a dominating ferromagnetic order which is the case within each layer of these compounds (McGuire, Clark, et al., 2017).

Magnetism in 2D materials is interesting due to the anisotropy effect giving rise to the idea of easy-axis. The directional dependence of magnetization is evident from comparing the susceptibility plots between the parallel and perpendicular orientations of the sample (in reference to the crystals ab-plane) versus the magnetic field. In the case of the parent compound ($NiCl_2$) and both $Co_{1-x}Ni_xCl_2$ alloys, the magnetic moments preferentially orient in the parallel direction (evident from the higher susceptibility) meaning that the easy-axis in this alloy system is within the ab-plane. Owing to the similarity of the two parent compounds in terms of structure and properties, the magnetic properties can be easily tailored within that space. Detailed analysis remains to be done and is expected to reveal more fundamental information on the magnetism within these alloy compounds.

4.3.3 $Fe_{(1-x)}Cr_xCl_3$

Alloy systems exist only after certain requirements are met, as detailed in the beginning of this chapter. Thermodynamically stable alloys have lower mixing energy

compared to the phase separated compounds/elements. The factors that determine the mixing energy of an alloy are manyfold including the crystal structure of the elements or compounds to be mixed. As such, two TMH compounds that were found to be phase separated are $CrCl_3$ and $FeCl_3$. The former exists in the monoclinic structure with C2/m space group while the latter can take on a rhombohedral BiI_3 crystal structure ($R\bar{3}$ space group), trigonal Ti_3O structure (P312 space group), or trigonal ($P\bar{3}$) structure. This fact conditions the stability of their alloy making them incompatible, albeit it is not the only determining factor for their miscibility. Chromium with electronegativity of 1.66, and iron of 1.83 apply a different amount of 'pull' towards the shared electrons with chlorine atoms. Iron is also much smaller (~156 pm) compared to chromium with atomic radius ~166 pm. Their change in radius is induced due to their different number of d-orbital electrons; Chromium is filled up to $3d^4$, while iron has $3d^6$ electrons. Constrained in the tri-chloride composition, their respective TMH compounds have great difference in their electronic structures. The parent compounds are as a result stable at significantly different temperatures with $CrCl_3$ having a melting point of 1152 ^oC and $FeCl_3$ melting at just 306 ^oC. This induces yet another constraint in the synthesis of their alloy, making it difficult to determine the growth conditions that would stabilize both cations within the same TMH crystal lattice in a +3-valence bonded to chlorine.

Synthesis of this compound was performed in a similar way to the previously detailed CVT growths. The precursors used are elemental (fine iron powder > 99% purity from Sigma Aldrich, 60-mesh or 250 μm chromium powder from Alfa Aesar of 99.99% metals basis purity, and $TeCl_4$ powder of 99.9% metals basis purity from Alfa Aesar) and add up to 0.5 grams of powders with a 50:50 cation stoichiometry. Growth was

performed in the conditions outlines in Table 9 with heating rate ~3 ^{o}C/min and natural cooling inside the two-zone furnace.

Table 9. Growth parameters for the CVT synthesis of $Cr_{1-x}Fe_xCl_3$ alloy.

	Hot zone T (^{o}C)	**Cold zone T (^{o}C)**	**Precursors**	**Growth time (hrs)**
Growth 1	750	660	Fe, Cr, $TeCl_4$	72 hours
Growth 2	700	570	Fe, Cr, $TeCl_4$	72 hours

The image below shows the visually distinguishable phases of $CrCl_3$ (purple crystal) and $FeCl_3$ (black crystal). Raman analysis confirms their identity leading to the conclusion that these two compounds are unstable given the growth conditions. That is not to say, however, that they are completely immiscible across the entire phase diagram (temperature and composition range). To establish their alloying extent (if any is possible), experiments are to be performed at different temperatures and precursor ratios.

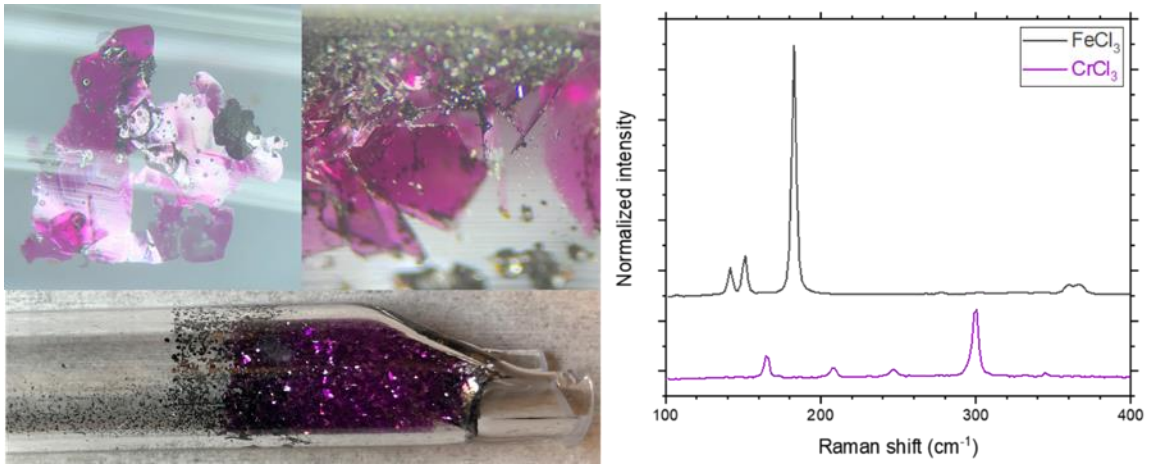

Fig. 47 | Image of the phase separated alloy of $CrCl_3$ and $FeCl_3$ with the former associated with the purple crystals while the latter with the smaller black crystals (left). Raman spectra of the two compounds clearly indicating that there is no alloying between them (right).

4.4 Summary of TMH cationic alloy growth and relevant properties

Synthesis of $Mo_{(1-x)}Cr_xCl_3$, $Co_{(1-x)}Ni_xCl_2$, and $Fe_{(1-x)}Cr_xCl_3$ TMH alloys was performed using chemical vapor transport, which allows for growth to occur in a closed, high pressure environment. Growth of these alloys takes place by transport of metal species from a hot zone to a colder zone driven by a temperature gradient. Metals are transported by means of chemically bonding to gaseous species of dissociated tellurium tetrachloride and converting into gaseous complexes. As a result of the endothermic nature of the chemical reactions taking place, these complexes are then transported to a region of a reduced temperature where they crystallize. The transport is performed for 72 hours to ensure that all reactions are completed, and stoichiometry of precursors is preserved. The final crystal formed within the ampoule is the most thermodynamically stable compound given the pressure, temperature, and chemical environment.

It was determined that alloys of $Co_{(1-x)}Ni_xCl_2$ are the easiest to form as a result of the similarity between the two parent compounds. That is, they both have the same rhombohedral ($R\bar{3}m$) crystal structure, similar atomic radius (Co = 152 pm, Ni = 149 pm), electronegativity (Co = 188, Ni = 191), with a small difference in electronic structure (Co = $3d^7$, Ni = $3d^8$). Alloys of $Mo_{(1-x)}Cr_xCl_3$ are also stable, with some data suggesting partial phase separation which will need to be confirmed with more detailed analysis. This is proposed to be the case due to the difference in atomic radius between chromium and molybdenum (Cr = 166 pm, Mo = 190 pm), and electronegativity (Cr = 1.66, Mo = 2.16). Crystallographic structure is also the same between both parent compounds (monoclinic C2/m). Lastly, $Fe_{(1-x)}Cr_xCl_3$ is found to be more thermodynamically stable in the phase-separated state, at least given the two sets of

conditions that were attempted for the synthesis of this alloy. As a result, it is concluded that the dissimilarity in the crystal structure of the two parent compounds ($CrCl_3$ = monoclinic C2/m, $FeCl_3$ = most stable in trigonal P312) leads to the destabilization of their ternary alloy likely due to lower Gibbs free energy associated with their phase-separation. This does not mean that this alloy is unstable under different temperature, pressure and compositional ratio environments. Further studies can reveal more about the potential of alloying $FeCl_3$ and $CrCl_3$.

The properties of the $Co_{(1-x)}Ni_xCl_2$ alloys are scaled quite predictably with composition. That is, Raman peak shifts are linearly scaled with foreign metal concentration, XRD peaks as well as Néel transition temperature also shift from the characteristic value of one parent compound towards the other but not in a linear fashion. Magnetic character remains the same, that is, the parent compounds and their alloys are AFM below the Néel temperature. The $Mo_{(1-x)}Cr_xCl_3$ alloys also induce Raman peak shifts but the trend is not very clear given the number of data points. That is, more alloy compositions need to be synthesized to be able to establish such a trend. The presence of a double peak around 300 cm^{-1} suggests that there is possibility for phase separation but does not phase out the possibility for the emergence of new phases induced by alloying $CrCl_3$ with molybdenum. XRD peaks shift to lower angle values with increasing molybdenum illustrating an increase in the interplanar spacing due to the larger atomic size of molybdenum compared to chromium. The presence of an additional peak at 14.8^o that does not change position with alloying composition also suggests that partial phase separation could be taking place. Magnetic properties of these alloys are rather interesting. Magnetization curves become more ferromagnetic-like with increasing

molybdenum concentration. Susceptibility shifts to lower temperatures and shows ferromagnetic-like curvature below the transition temperature. When the molybdenum concentration reaches ~75%, the easy-axis magnetization appears to shift from parallel to perpendicular. However, this data is still preliminary and much more in-depth magnetic and structural measurements are necessary to confirm the observations made and discussed here.

5. CONCLUSION AND FUTURE OUTLOOK

Alloying TMH compounds via cation substitution has great potential to tune their optical, structural, and magnetic properties. The importance of this technique roots from the simplicity of the process and the wide array of options considering the large number of transition metals constituting the majority of the periodic table. Alloying the anions in TMH compounds is equally beneficial but provides limited space for exploration.

To explore this territory, this work presents for the first time the synthesis of three ternary alloy systems, namely $Mo_{(1-x)}Cr_xCl_3$, $Co_{(1-x)}Ni_xCl_2$, and $Fe_{(1-x)}Cr_xCl_3$. The results give a lot of insight into the growth mechanism, factors determining alloy miscibility or the lack thereof, the effect of alloying over the structure and magnetic properties and shed some light over the challenges that could be faced within other, unexplored, TMH alloy systems, all of which is discussed in the previous chapter.

This work is still the beginning of some exciting exploration that needs to take place which will require further analysis and more sophisticated characterization to confirm the proposed phenomena that seem to be taking place given the current data. Future studies should focus on understanding how the molybdenum concentration affects the phase-space of the $Mo_{(1-x)}Cr_xCl_3$ alloy and determine whether a phase transition takes place at any point in the compositional range. Magnetic measurements of susceptibility as a function of temperature must be performed at varying magnetic field levels and hysteresis curves at varying temperatures. These types of measurements will paint a clearer picture on the type of magnetic order taking place at varying temperature and field, and as a function of alloy stoichiometry. It would be quite useful to study the high temperature magnetic space of the $Mo_{(1-x)}Cr_xCl_3$ alloy, given the paramagnetic and

predicted antiferromagnetic order with increasing temperature in $MoCl_3$. Even further in future studies, the magnetism should be studied as a function of crystal thickness / number of layers to determine whether magnetic order can be maintained and the modifications that could take place.

Given these findings, it is clear that alloying can be quite useful in achieving desired material properties. In the case of this material class, the goal will be to understand and tune magnetism to ultimately achieve ferromagnetic and antiferromagnetic systems that retain their magnetic order at room temperature. Although a lot of work remains to be done to reach that goal, alloying can definitely be employed along the way. It will be interesting to study other types of TMH alloys, especially those that can yield drastic changes and new emerging magneto-structural phases.

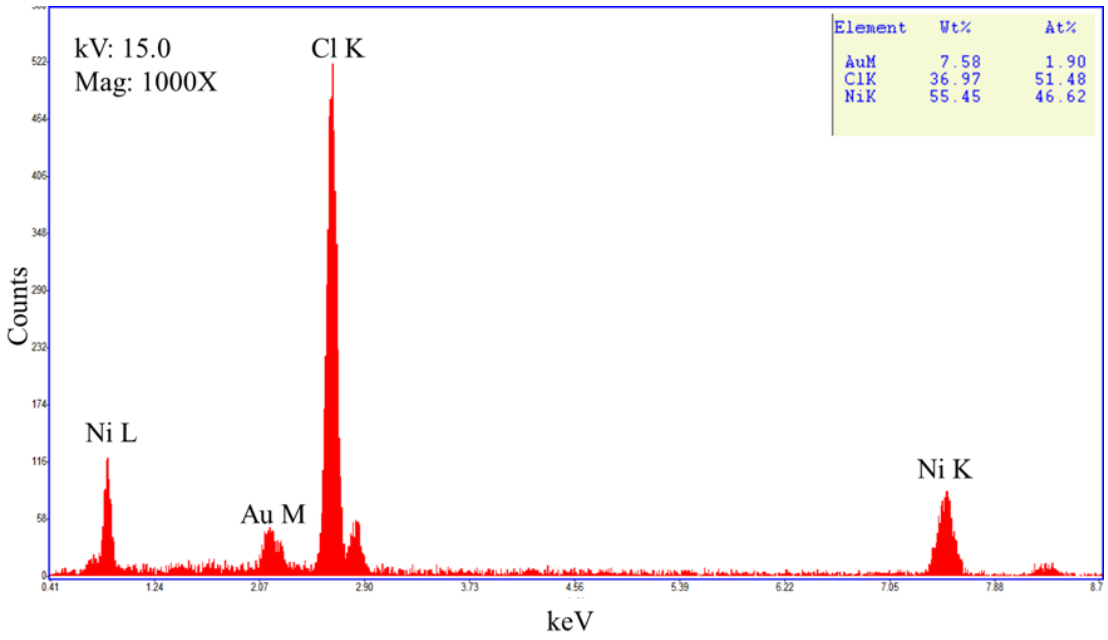

Fig. 48 | EDS spectrum of $NiCl_2$. Note the lower chlorine atomic % is due to low detection of lighter atoms versus heavier one leading to an underestimation of chlorine.

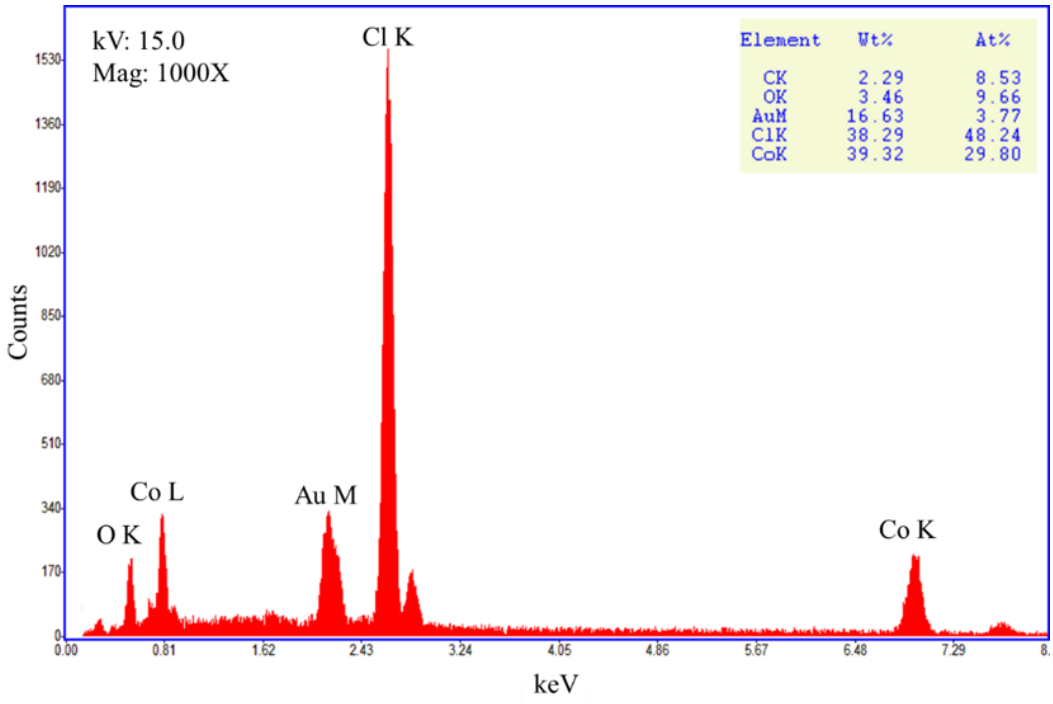

Fig. 49 | EDS spectrum of $CoCl_2$. Note the lower chlorine atomic % is due to low detection of lighter atoms versus heavier one leading to an underestimation of chlorine. Oxygen is detected due to this compound being highly hygroscopic.

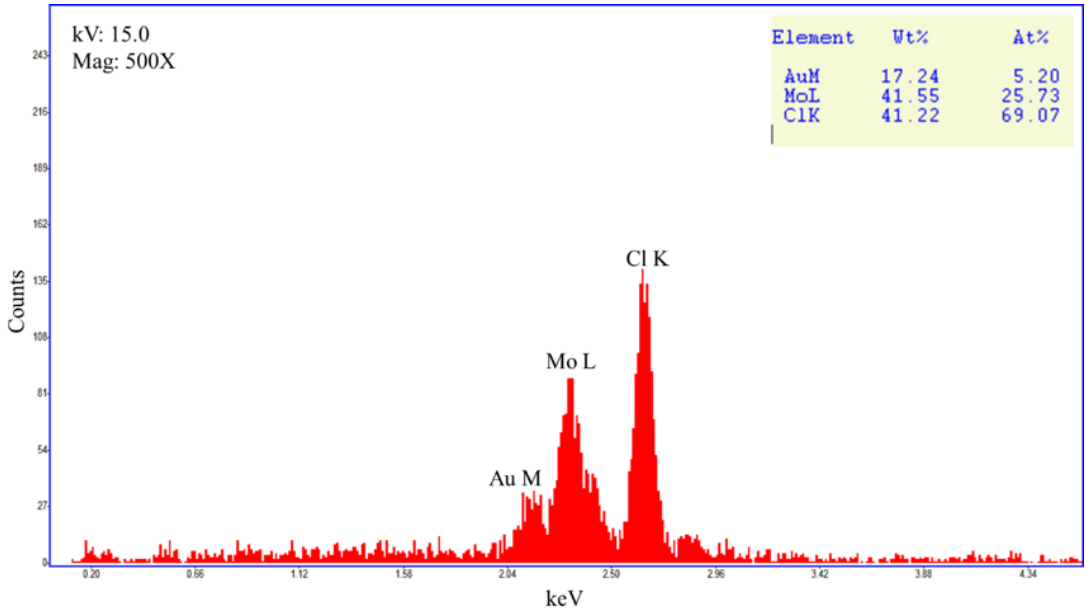

Fig. 50 | EDS spectrum of $MoCl_3$. Note the lower chlorine atomic % is due to low detection of lighter atoms versus heavier one leading to an underestimation of chlorine.

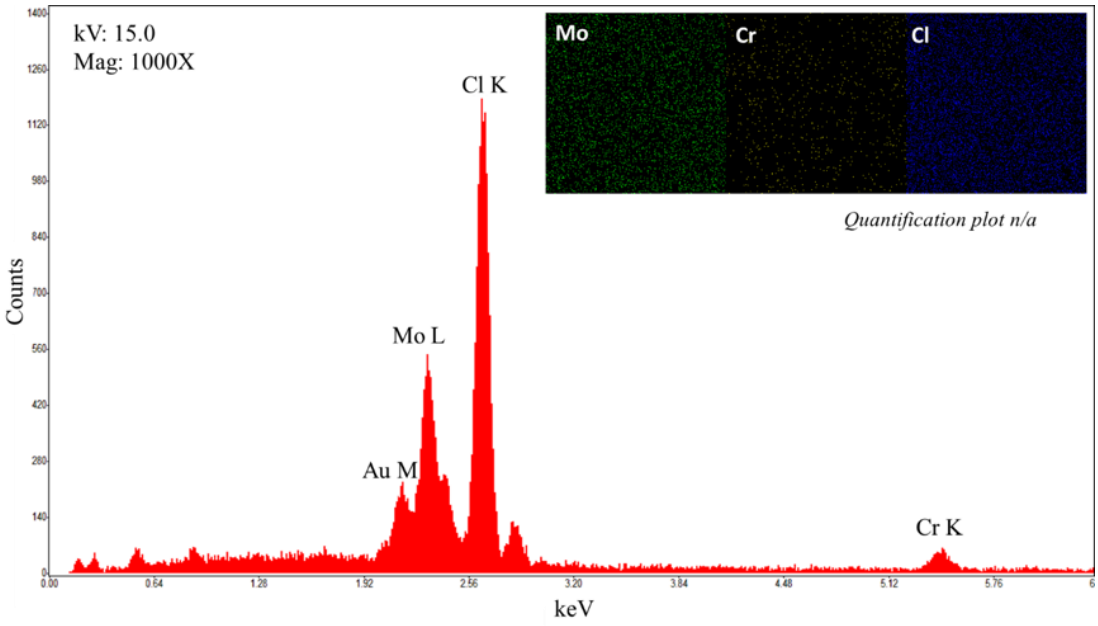

Fig. 51 | EDS spectrum of $Mo_{0.77}Cr_{0.23}Cl_{2.64}$. Note the lower chlorine atomic % is due to low detection of lighter atoms versus heavier one leading to an underestimation of chlorine. Quantification EDS plot not available.

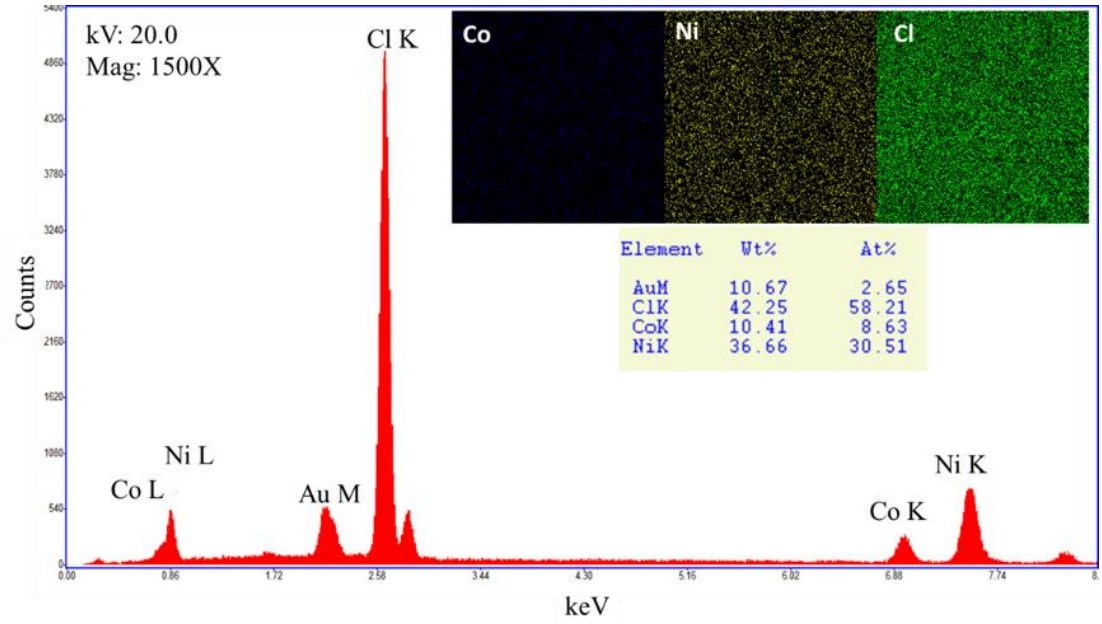

Fig. 52 | EDS spectrum of $Co_{22}Ni_{78}Cl_{1.5}$. Note the lower chlorine atomic % is due to low detection of lighter atoms versus heavier one leading to an underestimation of chlorine.

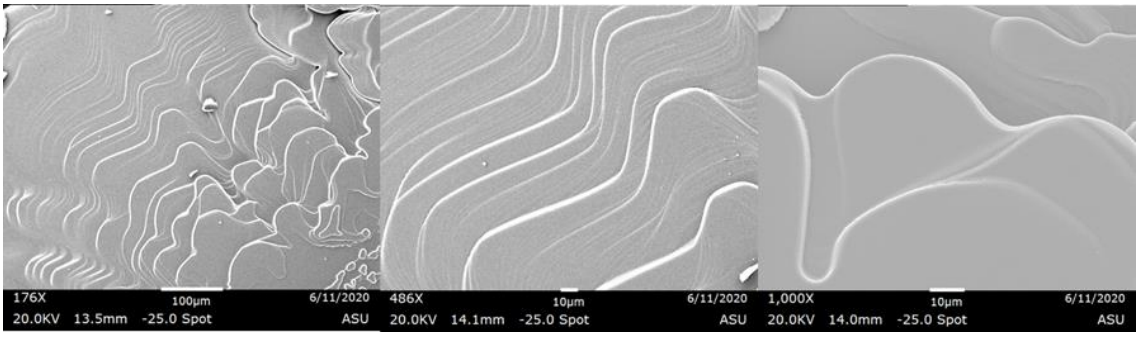

Fig. 53 | SEM images of $Co_{22}Ni_{78}Cl_{1.5}$. The growth dynamics of all cobalt and nickel chloride alloys tends to have similar wave-like edges.

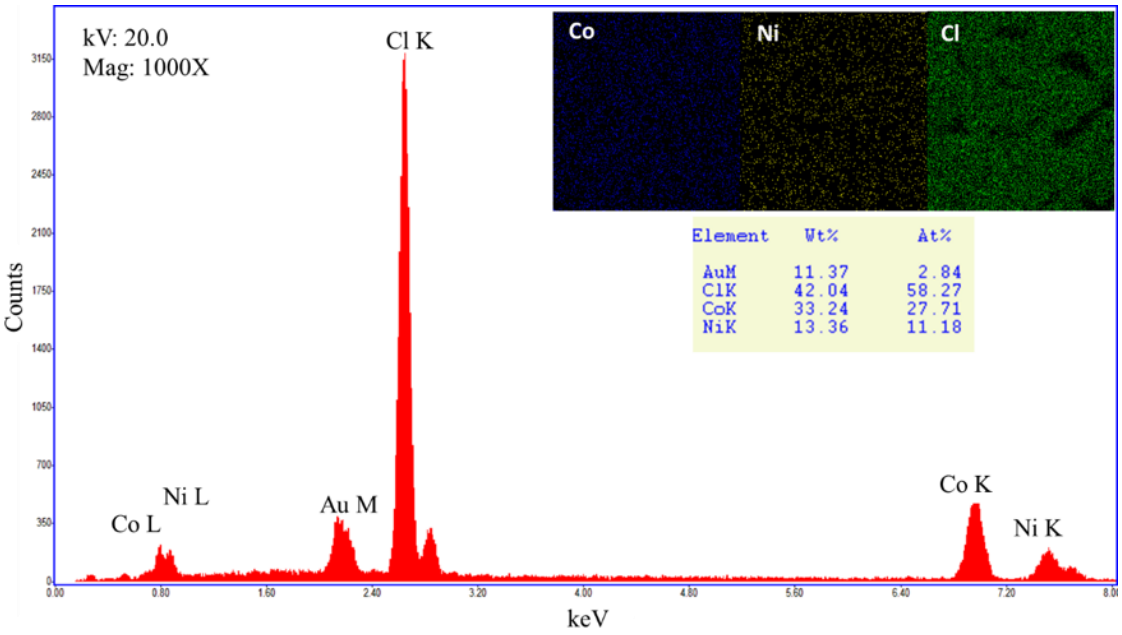

Fig. 54 | EDS spectrum of $Co_{71}Ni_{29}Cl_{1.5}$. Note the lower chlorine atomic % is due to low detection of lighter atoms versus heavier one leading to an underestimation of chlorine.

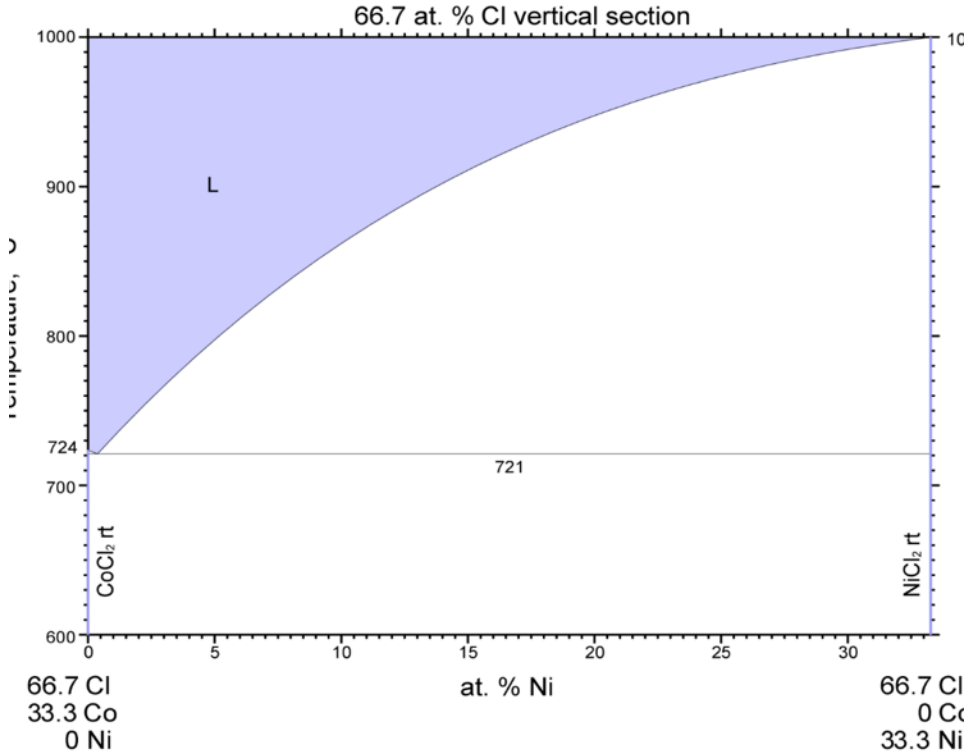

Fig. 55 | Phase diagram of $CoCl_2$ and $NiCl_2$ showing immiscibility across the entire alloying range.

7. REFERENCES

Abramchuk, M., Jaszewski, S., Metz, K. R., Osterhoudt, G. B., Wang, Y., Burch, K. S., & Tafti, F. (2018). Controlling Magnetic and Optical Properties of the van der Waals Crystal CrCl3−xBrx via Mixed Halide Chemistry. *Advanced Materials*, *30*(25), 1–7. https://doi.org/10.1002/adma.201801325

Agarwal, A., Qin, Y., Chen, B., Blei, M., Wu, K., Liu, L., … Tongay, S. (2018). Anomalous isoelectronic chalcogen rejection in 2D anisotropic vdW TiS3(1-:X)Se3x trichalcogenides. *Nanoscale*, *10*(33), 15654–15660. https://doi.org/10.1039/c8nr04274h

Ardizzone, V., De Marco, L., De Giorgi, M., Dominici, L., Ballarini, D., & Sanvitto, D. (2019). Emerging 2D materials for room-temperature polaritonics. *Nanophotonics*, *8*(9), 1547–1558. https://doi.org/10.1515/nanoph-2019-0114

Ashcroft, N. W., & Mermin, N. D. (1968). Solid state physics. *Vacuum*, Vol. 18, p. 525. https://doi.org/10.1016/0042-207x(68)90868-3

Binnewies, M., Glaum, R., Schmidt, M., & Schmidt, P. (2012). Chemical Vapor Transport Reactions. *Chemical Vapor Transport Reactions*, 1–16. https://doi.org/10.1515/9783110254655

Bonaccorso, F., Sun, Z., Hasan, T., & Ferrari, A. C. (2010). Graphene photonics and optoelectronics. *Nature Photonics*, *4*(9), 611–622. https://doi.org/10.1038/nphoton.2010.186

Bonilla, M., Kolekar, S., Ma, Y., Diaz, H. C., Kalappattil, V., Das, R., … Batzill, M. (2018). Strong roomerature ferromagnetism in VSe2 monolayers on van der Waals substrates. *Nature Nanotechnology*, *13*(4), 289–293. https://doi.org/10.1038/s41565-018-0063-9

Botana, A. S., & Norman, M. R. (2019). Electronic structure and magnetism of transition metal dihalides: Bulk to monolayer. *Physical Review Materials*, *3*(4), 1–7.

https://doi.org/10.1103/PhysRevMaterials.3.044001

Burch, K. S., Mandrus, D., & Park, J. G. (2018). Magnetism in two-dimensional van der Waals materials. *Nature*, *563*(7729), 47–52. https://doi.org/10.1038/s41586-018-0631-z

Cain, J. D., Hanson, E. D., & Dravid, V. P. (2018). Controlled synthesis of 2D MX2 (M = Mo, W; X = S, Se) heterostructures and alloys. *Journal of Applied Physics*, *123*(20). https://doi.org/10.1063/1.5025710

Camley, R. E., Celinski, Z., & Stamps, R. L. (Eds.). (2015). Magnetism of surfaces, interfaces, and nanoscale materials. Retrieved from https://ebookcentral-proquest-com.ezproxy1.lib.asu.edu

Castro Neto, A. H., Guinea, F., Peres, N. M. R., Novoselov, K. S., & Geim, A. K. (2009). The electronic properties of graphene. *Reviews of Modern Physics*, *81*(1), 109–162. https://doi.org/10.1103/RevModPhys.81.109

Chakraborty, C., Vamivakas, N., & Englund, D. (2019). Advances in quantum light emission from 2D materials. *Nanophotonics*, *8*(11), 2017–2032. https://doi.org/10.1515/nanoph-2019-0140

Chhowalla, M., Shin, H. S., Eda, G., Li, L. J., Loh, K. P., & Zhang, H. (2013). The chemistry of two-dimensional layered transition metal dichalcogenide nanosheets. *Nature Chemistry*, *5*(4), 263–275. https://doi.org/10.1038/nchem.1589

Choi, W., Choudhary, N., Han, G. H., Park, J., Akinwande, D., & Lee, Y. H. (2017). Recent development of two-dimensional transition metal dichalcogenides and their applications. *Materials Today*, *20*(3), 116–130. https://doi.org/10.1016/j.mattod.2016.10.002

Deng, D., Novoselov, K. S., Fu, Q., Zheng, N., Tian, Z., & Bao, X. (2016). Catalysis with two-dimensional materials and their heterostructures. *Nature Nanotechnology*,

11(3), 218–230. https://doi.org/10.1038/nnano.2015.340

Duan, X., Wang, C., Fan, Z., Hao, G., Kou, L., Halim, U., … Duan, X. (2016). Synthesis of WS2xSe2-2x Alloy Nanosheets with Composition-Tunable Electronic Properties. *Nano Letters*, *16*(1), 264–269. https://doi.org/10.1021/acs.nanolett.5b03662

Feigelson, R. S. (2015). Crystal Growth through the Ages: A Historical Perspective. In *Handbook of Crystal Growth: Second Edition* (Second Edi, Vol. 1). https://doi.org/10.1016/B978-0-444-56369-9.00001-0

Geim, A. K. (2009). Graphene: Status and prospects. *Science*, *324*(5934), 1530–1534. https://doi.org/10.1126/science.1158877

George, S. M., & Kandasubramanian, B. (2020). Advancements in MXene-Polymer composites for various biomedical applications. *Ceramics International*, *46*(7), 8522–8535. https://doi.org/10.1016/j.ceramint.2019.12.257

Gibertini, M., Koperski, M., Morpurgo, A. F., & Novoselov, K. S. (2019). Magnetic 2D materials and heterostructures. *Nature Nanotechnology*, *14*(5), 408–419. https://doi.org/10.1038/s41565-019-0438-6

Ginsberg, N. S., & Tisdale, W. A. (2020). Spatially Resolved Photogenerated Exciton and Charge Transport in Emerging Semiconductors. *Annual Review of Physical Chemistry*, *71*(1), 1–30. https://doi.org/10.1146/annurev-physchem-052516-050703

Gong, C., Li, L., Li, Z., Ji, H., Stern, A., Xia, Y., … Zhang, X. (2017). Discovery of Intrinsic Ferromagnetism in Two-Dimensional van der Waals Crystals. *IEICE Electronics Express*.

Gupta, A., Sakthivel, T., & Seal, S. (2015). Recent development in 2D materials beyond graphene. *Progress in Materials Science*, *73*, 44–126. https://doi.org/10.1016/j.pmatsci.2015.02.002

Hu, F., & Fei, Z. (2020). Recent Progress on Exciton Polaritons in Layered Transition-Metal Dichalcogenides. *Advanced Optical Materials*, *8*(5), 1–16. https://doi.org/10.1002/adom.201901003

Huang, B., Clark, G., Navarro-Moratalla, E., Klein, D. R., Cheng, R., Seyler, K. L., … Xu, X. (2017). Layer-dependent ferromagnetism in a van der Waals crystal down to the monolayer limit. *Nature*, *546*(7657), 270–273. https://doi.org/10.1038/nature22391

Huang, X., Zeng, Z., & Zhang, H. (2013). Metal dichalcogenide nanosheets: Preparation, properties and applications. *Chemical Society Reviews*, *42*(5), 1934–1946. https://doi.org/10.1039/c2cs35387c

Kang, S., Lee, D., Kim, J., Capasso, A., Kang, H. S., Park, J. W., … Lee, G. H. (2020). 2D semiconducting materials for electronic and optoelectronic applications: Potential and challenge. *2D Materials*, *7*(2). https://doi.org/10.1088/2053-1583/ab6267

Klein, D. R., MacNeill, D., Lado, J. L., Soriano, D., Navarro-Moratalla, E., Watanabe, K., … Jarillo-Herrero, P. (2018). Probing magnetism in 2D van der Waals crystalline insulators via electron tunneling. *Science*, *360*(6394), 1218–1222. https://doi.org/10.1126/science.aar3617

Kuo, C. T., Neumann, M., Balamurugan, K., Park, H. J., Kang, S., Shiu, H. W., … Park, J. G. (2016). Exfoliation and Raman Spectroscopic Fingerprint of Few-Layer NiPS 3 Van der Waals Crystals. *Scientific Reports*, *6*(May 2015), 1–10. https://doi.org/10.1038/srep20904

Lee, J. U., Lee, S., Ryoo, J. H., Kang, S., Kim, T. Y., Kim, P., … Cheong, H. (2016). Ising-Type Magnetic Ordering in Atomically Thin FePS3. *Nano Letters*, *16*(12), 7433–7438. https://doi.org/10.1021/acs.nanolett.6b03052

Leng, Y. (2013a). Chapter 4 - Scanning electron microscopy. In *Materials Characterization : Introduction to Microscopic and Spectroscopic Methods* (2nd ed.,

pp. 41–75). https://doi.org/10.1029/2003JD004173.Aires

Leng, Y. (2013b). Chapter 6 X-Ray Spectroscopy for Elemental Analysis. In *Materials Characterization : Introduction to Microscopic and Spectroscopic Methods* (2nd ed., pp. 191–219). https://doi.org/10.1002/9783527670772.ch6

Lewandowska, R., & Liu, J. (2016). Raman Microscopy: Analysis of Nanomaterials. *Reference Module in Materials Science and Materials Engineering*, 1–6. https://doi.org/10.1016/b978-0-12-803581-8.02593-5

Li, H., Duan, X., Wu, X., Zhuang, X., Zhou, H., Zhang, Q., … Duan, X. (2014). Growth of alloy MoS2xSe2(1-x) nanosheets with fully tunable chemical compositions and optical properties. *Journal of the American Chemical Society*, *136*(10), 3756–3759. https://doi.org/10.1021/ja500069b

Lin, M. W., Zhuang, H. L., Yan, J., Ward, T. Z., Puretzky, A. A., Rouleau, C. M., … Xiao, K. (2016). Ultrathin nanosheets of CrSiTe3: A semiconducting two-dimensional ferromagnetic material. *Journal of Materials Chemistry C*, *4*(2), 315–322. https://doi.org/10.1039/c5tc03463a

Liu, Y., Zeng, C., Zhong, J., Ding, J., Wang, Z. M., & Liu, Z. (2020). Spintronics in Two-Dimensional Materials. *Nano-Micro Letters*, *12*(1). https://doi.org/10.1007/s40820-020-00424-2

Lockwood, D. J., Bertrand, D., Carrara, P., Mischler, G., Billerey, D., & Terrier, C. (1979). Raman spectrum of NiCl2. *Journal of Physics C: Solid State Physics*, *12*(17), 3615–3620. https://doi.org/10.1088/0022-3719/12/17/031

Lockwood, D. J., Johnstone, I. W., Carrara, P., & Mischler, G. (1978). *Raman scattering from magnons in CoCl2 and FeCl2*. *25*.

Mas-Ballesté, R., Gómez-Navarro, C., Gómez-Herrero, J., & Zamora, F. (2011). 2D materials: To graphene and beyond. *Nanoscale*, *3*(1), 20–30.

https://doi.org/10.1039/c0nr00323a

McGuire, M. A. (2017). Crystal and magnetic structures in layered, transition metal dihalides and trihalides. *Crystals*, *7*(5). https://doi.org/10.3390/cryst7050121

McGuire, M. A., Clark, G., Kc, S., Chance, W. M., Jellison, G. E., Cooper, V. R., … Sales, B. C. (2017). Magnetic behavior and spin-lattice coupling in cleavable van der Waals layered CrCl3 crystals. *Physical Review Materials*, *1*(1), 1–10. https://doi.org/10.1103/PhysRevMaterials.1.014001

McGuire, M. A., Yan, J., Lampen-Kelley, P., May, A. F., Cooper, V. R., Lindsay, L., … Sales, B. C. (2017). High-temperature magnetostructural transition in van der Waals-layered α-MoCl3. *Physical Review Materials*, *1*(6), 1–10. https://doi.org/10.1103/PhysRevMaterials.1.064001

Mermin, N. D., & Wagner, H. (1966). Absence of ferromagnetism or antiferromagnetism in one- or two-dimensional isotropic Heisenberg models. *Physical Review Letters*, *17*(22), 1133–1136. https://doi.org/10.1103/PhysRevLett.17.1133

Mogi, M., Tsukazaki, A., Kaneko, Y., Yoshimi, R., Takahashi, K. S., Kawasaki, M., & Tokura, Y. (2018). Ferromagnetic insulator Cr2Ge2Te6 thin films with perpendicular remanence. *APL Materials*, *6*(9). https://doi.org/10.1063/1.5046166

Novoselov, K. S., Fal'Ko, V. I., Colombo, L., Gellert, P. R., Schwab, M. G., & Kim, K. (2012). A roadmap for graphene. *Nature*, *490*(7419), 192–200. https://doi.org/10.1038/nature11458

Novoselov, K. S., Mishchenko, A., Carvalho, A., & Castro Neto, A. H. (2016). 2D materials and van der Waals heterostructures. *Science*, *353*(6298). https://doi.org/10.1126/science.aac9439

Parvez, K. (2019). Two-dimensional nanomaterials: Crystal structure and synthesis. In *Biomedical Applications of Graphene and 2D Nanomaterials*.

https://doi.org/10.1016/B978-0-12-815889-0.00001-5

Principles, B. (2009). *Basic Principles of Non-Contact Temperature Measurement*. 1–32. https://doi.org/10.1016/B978-0-12-386984-5.10002-3

Qian, Z., Jiao, L., & Xie, L. (2020). Phase Engineering of Two-Dimensional Transition Metal Dichalcogenides. *Chinese Journal of Chemistry*. https://doi.org/10.1002/cjoc.202000064

Siena, M. C. De, Creutz, S. E., Regan, A., Malinowski, P., Jiang, Q., Kluherz, K. T., … Gamelin, D. R. (n.d.). *with Robust Ferromagnetism*.

Stanford, M. G., Rack, P. D., & Jariwala, D. (2018). Emerging nanofabrication and quantum confinement techniques for 2D materials beyond graphene. *Npj 2D Materials and Applications*, *2*(1). https://doi.org/10.1038/s41699-018-0065-3

Susarla, S., Kutana, A., Hachtel, J. A., Kochat, V., Apte, A., Vajtai, R., … Ajayan, P. M. (2017). Quaternary 2D Transition Metal Dichalcogenides (TMDs) with Tunable Bandgap. *Advanced Materials*, *29*(35), 1–8. https://doi.org/10.1002/adma.201702457

Tomar, S., Ghosh, B., Mardanya, S., Rastogi, P., Bhadoria, B. S., Chauhan, Y. S., … Bhowmick, S. (2019). Intrinsic magnetism in monolayer transition metal trihalides: A comparative study. *Journal of Magnetism and Magnetic Materials*, *489*(January), 165384. https://doi.org/10.1016/j.jmmm.2019.165384

Wang, Hao, Li, S., Ai, R., Huang, H., Shao, L., & Wang, J. (2020). Plasmonically enabled two-dimensional material-based optoelectronic devices. *Nanoscale*, *12*(15), 8095–8108. https://doi.org/10.1039/c9nr10755j

Wang, Haotian, Yuan, H., Sae Hong, S., Li, Y., & Cui, Y. (2015). Physical and chemical tuning of two-dimensional transition metal dichalcogenides. *Chemical Society Reviews*, *44*(9), 2664–2680. https://doi.org/10.1039/c4cs00287c

Wang, Xiaomu, & Xia, F. (2015). Stacked 2D materials shed light. *Nature Materials*, *14*(3), 264–265. https://doi.org/10.1038/nmat4218

Wang, Xingzhi, Du, K., Liu, Y. Y. F., Hu, P., Zhang, J., Zhang, Q., … Xiong, Q. (2016). Raman spectroscopy of atomically thin two-dimensional magnetic iron phosphorus trisulfide (FePS3) crystals. *2D Materials*, *3*(3). https://doi.org/10.1088/2053-1583/3/3/031009

Wolverson, D. (2008). Raman spectroscopy. In *Characterization of Semiconductor Heterostructures and Nanostructures*. https://doi.org/10.1016/B978-0-444-53099-8.00008-7

Wu, K., Blei, M., Chen, B., Liu, L., Cai, H., Brayfield, C., … Tongay, S. (2020). Phase Transition across Anisotropic NbS3 and Direct Gap Semiconductor TiS3 at Nominal Titanium Alloying Limit. *Advanced Materials*, *32*(17), 1–8. https://doi.org/10.1002/adma.202000018

Xu, C., Feng, J., Prokhorenko, S., Nahas, Y., Xiang, H., & Bellaiche, L. (2020). Topological spin texture in Janus monolayers of the chromium trihalides Cr(I, X)3. *Physical Review B*, *101*(6), 60404. https://doi.org/10.1103/PhysRevB.101.060404

Yuan, S., Pang, S.-Y., & Hao, J. (2020). 2D transition metal dichalcogenides, carbides, nitrides, and their applications in supercapacitors and electrocatalytic hydrogen evolution reaction. *Applied Physics Reviews*, *7*(2), 021304. https://doi.org/10.1063/5.0005141

Zeng, Q., Wang, H., Fu, W., Gong, Y., Zhou, W., Ajayan, P. M., … Liu, Z. (2015). Band engineering for novel two-dimensional atomic layers. *Small*, *11*(16), 1868–1884. https://doi.org/10.1002/smll.201402380

Zheng, Y., Sun, F. Z., Han, X., Xu, J., & Bu, X. H. (2020). Recent Progress in 2D Metal-Organic Frameworks for Optical Applications. *Advanced Optical Materials*, *2000110*, 1–17. https://doi.org/10.1002/adom.202000110